Nonvolatile and Volatile Resistive Switching —

Characterization, Modeling, Memristive Subcircuits

Tong Liu

Dissertation submitted to the faculty of the Virginia Polytechnic Institute and State University in partial fulfillment of the requirements for the degree of

Doctor of Philosophy
In
Electrical Engineering

Marius K. Orlowski, Committee Chair
Louis J. Guido
Mantu K. Hudait
Joseph G. Tront
Jean J. Heremans

April 29, 2013
Blacksburg, Virginia

Keywords: resistive switching, nonvolatile memory, volatile switching, memristor, conductive filament, simulation model

Nonvolatile and Volatile Resistive Switching — Characterization, Modeling, Memristive Subcircuits

Tong Liu

Abstract

Emerging memory technologies are being intensively investigated for extending Moore's law in the next decade. The conductive bridge random access memory (CBRAM) is one of the most promising candidates. CBRAM shows unique nanoionics-based filamentary switching mechanism. Compared to flash memory, the advantages of CBRAM include excellent scalability, low power consumption, high OFF-/ON-state resistance ratio, good endurance, and long retention. Besides the nonvolatile memory applications, resistive switching devices implement the function of memristor which is the fourth basic electrical component. This research presents the characterization and modeling of Cu/TaO_x/Pt resistive switching devices. Both Cu and oxygen vacancy nanofilaments can conduct current according to the polarity of bias voltage. The volatile resistive switching phenomenon has been observed on Cu/TaO_x/δ-Cu/Pt devices and explained by a flux balancing model. The resistive devices are also connected in series and in anti-parallel manner. These circuit elements are tested for chaotic neural circuit. The quantum conduction has been observed in the I–V characteristics of devices, evidencing the metallic contact between the nanofilament and electrodes. The model of filament radial growth has been developed to explain the transient I–V relation and multilevel switching in the

metallic contact regime. The electroforming/SET and RESET processes have been simulated according to the mechanism of conductive filament formation and rupture and validated by experimental results. The Joule and Thomson heating effects have also been investigated for the RESET processes.

Acknowledgment

I would like to express my sincerest gratitude to my doctoral advisor Professor Marius Orlowski for his guidance, support, and encouragement during my Ph.D. study. The fifty-two months research work under his advising was an exciting, wonderful, and treasurable experience. His profound knowledge, gentle personality, and rigorous attitude toward research will benefit my whole life.

I would thank Professors Louis Guido, Mantu Hudait, Joseph Tront, and Jean Heremans for serving as my committee members. I am very grateful to Don Leber, John Harris, and Professor Jerry Hunter for their advices and help in Micron Lab, CAD and Visualization Lab, and Nanoscale Characterization and Fabrication Lab of Virginia Tech. I would also appreciate the mentorship and suggestions from Professors Khai Ngo, Ming Xu, and Kathleen Meehan.

Special thanks are offered to my dearest parents, Enxue Liu and Ning Jiang, and my girlfriend Ying Li for their love and support.

I want to express my thanks to all colleagues and friends in Blacksburg: Yuhong Kang, Coumba Ndoye, Mohini Verma, Sarah El-Helw, Tanmay Potnis, Daocheng Huang, Xu Guo, Zhimin Chen, Ruxi Wang, Dong Jiang, Lei Pan, Qian Liu, Xiaohua Hu, Mingkai Mu, Shuilin Tian, Jing Xu, Yan Liang, Michele Lim, Fang Luo, Hua Lin, Xiao Cao, Puqi Ning, Yu Zhao, Hao-Hsiang Liao, Bo Wen, Dong Dong, Zheng Chen, Zhiyu Shen, Shuwen Duan, Kevin Chern, Timothy Ciarkowski, Bassam Alfeeli, Mehdi Nikkhah, Jing Sun, Liang Shan, Jiajia Li, Qiang Li, Yan Zhu, Nihkil Jain, Siddharth Vijayaraghavan, Zhiguang Zhu, Yihui Fang, Xin Xin, Shuchi Wu.

Table of Contents

Chapter 1 Introduction 1

1.1 Scaling Challenges in Flash Memory 1

1.2 Opportunities for Resistive Memory 3

1.2.1 Emerging Memory Technologies 4

1.2.2 Memristor..5

1.2.3 Synapse for Neuromorphic Computation 9

1.3 Fundamentals of Resistive Memory 9

1.3.1 Resistive Switching and Electrochemistry..10

1.3.2 Materials of Solid State Electrolytes..15

1.4 Dissertation Objective and Organization 16

Chapter 2 Characterization of Cu/TaO_x/Pt Resistive Switching Devices 20

2.1 Introduction...20

2.2 Fabrication Processes 21

2.3 Resistive Switching Based on Cu and Oxygen Vacancy Conductive Nanofilaments 25

2.4 Bubble Formation 35

2.5 RESET-SET Instability..40

2.6 Multilevel SET Process 43

2.7 Summary 45

Chapter 3 Volatile Switching of Cu/TaO_x/δ-Cu/Pt Devices.......................................46

3.1 Introduction...46

3.2 Threshold Switching of Resistive Memory 50

3.3 Characterization of Cu/TaO_x/δ-Cu/Pt Devices...51

3.4 Effect of Interfacial Layers on Device Fluctuations 62

3.5 Summary 64

Chapter 4 Circuit Elements Based on Cu/TaO_x/Pt Devices 65

4.1 Introduction...65

4.2 Complementary Resistive Switches (CRS) 66

4.3 Antiparallel Resistive Switches (APS) 67

4.4 APS in Single Cells 74

4.5 Cascaded Resistive Switches..76

4.6 Summary 85

Chapter 5 Multilevel Cell of CBRAM..86

5.1 Introduction..86

5.2 Physics of Multilevel Cell 87

5.3 Voltage Constant in Multilevel Switching...89

5.4 Radial Growth Model for Conical Filament..98

5.5 Temperature Effect..111

5.6 Summary 114

Chapter 6 Simulation of CBRAM Switching 116

6.1 Introduction..116

6.2 Rate-Limiting Process in Resistive Switching...117

6.3 Forming Process Simulation..120

6.4 Modeling of Thermal Effect in RESET Process 127

6.4.1 Joule Heating 129

6.4.2 Thomson Effect..132

6.5 Summary 136

Chapter 7 Summary and Future Works 138

7.1 Summary 138

7.2 Future Works 141

Bibliography 144

List of Figures

Fig. 1-1. Device structure and operating mechanism of flash memory (floating gate device). In the flash memory device, a floating gate is inserted in the oxide of MOSCAP. A high write/erase voltage is needed to charge/discharge the floating gate. Under the high electric field, electrons can tunnel through the gate oxide between the Si substrate and floating gate. 2

Fig. 1-2. (a) Redox memory, also known as CBRAM. It is based on the redox reaction in a thin solid electrolyte film sandwiched between two metal electrodes. (b) Spin-transfer torque memory which is based on magnetic tunneling junction CoFeB/MgO/CoFeB. 4

Fig. 1-3. The four fundamental two-terminal circuit elements: resistor, capacitor, inductor, and memristor [11]. 6

Fig. 1-4. Simplified equivalent circuit of the coupled variable-resistor model for a memristor [11]. 7

Fig. 1-5. Pinched hysteresis loop as a signature of memristors. (a) Schematic diagram. (b) Experimental I–V of a Cu/TaO_x/Pt device. 8

Fig. 1-6. Schematic illustration of switching processes of conductive bridge resistive devices. Red circles represents Cu atoms and cations. The yellow rectangle represents the solid electrolyte. The "+" and "–" signs represent the voltage polarity relative to 0 V…………...11

Fig. 1-7. Illustration of I–V characteristics of (a) bipolar switching and (b) unipolar switching.……..13

Fig. 1-8. Graphic view of the electron transfer in redox reactions at the electrode/electrolyte interface. 14

Fig. 2-1. Schematic layer structure of the cross section of Cu/TaO_x/Pt resistive memory device. 22

Fig. 2-2. Process flow of Cu/TaO_x/Pt conductive bridge resistive devices. (1) Thermal oxidation of Si substrate. (2) Lithography and Pt/Ti e-beam evaporation. (3) Pt/Ti lift-off. (4) Lithography, TaO_x e-beam deposition, and TaO_x lift-off. (5) Lithography, Cu e-beam deposition, and Cu lift-off. 22

Fig. 2-3. Schematic illustration of the electron beam deposition. 25

Fig. 2-4. Schematic illustration of voltage sweeping mode in DC characterization....26

Fig. 2-5. I–V characteristics of bipolar and unipolar switching. (a) Bipolar switching of V_O CF. (b) Unipolar switching of V_O CF. (c) Bipolar switching of Cu CF. (d) Unipolar switching of Cu CF. 27

Fig. 2-6. (a) Dependence of R_{ON} of individual resistive switches as a function of the compliance current applied to the cells during the set operation. (b) Retention of Cu CF at room temperature. The Cu CF was formed with compliance current of 1 mA. 29

Fig. 2-7. (a) Consecutive bipolar switching of Cu CF and unipolar switching of V_O CF. Section 1 and 2 are the set and reset operations of Cu CF. Section 3 and 4 are the set and reset operations of V_O CF. (b) Consecutive bipolar switching of Cu and V_O CFs. Section 1 and 2 are the set and reset operations of V_O CF. Section 3 and 4 are the set and reset operations of Cu CF. 30

Fig. 2-8. (a) Repeated unipolar switching characteristics for V_O CF in a $Cu/TaO_x/Pt$ device. (b) Retension property of the V_O CF at 25 °C. The ON/OFF resistance ratio is 10^4. The LRS and HRS stays nearly constant up to 10^6 seconds................................31

Fig. 2-9. R_{ON} temperature coefficient α of (a) Cu CF and (b) V_O CF. 32

Fig. 2-10. (a) V_{SET} and V_{RESET} distributions of $Cu/TaO_x/Pt$ devices. The SET voltage is positive for Cu CFs. (b) V_{SET} and V_{RESET} distributions of $Cu/TaO_x/Pt$ devices. The SET voltage is negative for V_O CFs. (c) R_{ON} and R_{OFF} distributions of Cu CFs in $Cu/TaO_x/Pt$ devices. The read voltage is 0.1 V for R_{OFF}. (d) R_{ON} and R_{OFF} distributions of V_O CFs. The device sizes are 10 μm, 15 μm, 20 μm, 25 μm, 30 μm, and 35 μm.… 33

Fig. 2-11. (a) V_{SET} and V_{RESET} distributions of $Cu/TaO_x/Pt$ devices with V_O CFs. Both positive and negative reset voltages can be used to rupture the conductive filaments. (b) Comparison of set voltages of Cu and V_O CFs. The V_O CF needs higher V_{SET} than the Cu CF……… 35

Fig. 2-12. (a) Image of 10 μm × 10 μm cells after multiple switching (0 to −7 V). No protrusions are observed. The inset shows the enlarged view of one device. (b) Image of 35 μm × 35 μm cells after forming voltage sweep from 0 to −7 V. The inset shows the enlarged view of protrusions...37

Fig. 2-13. Percolation model for the bubble formation and resistive switching based on oxygen vancancy filament. (a) Oxygen vacancy generation. (b) Oxygen vacancy distribution. (c) Conductive path formation. (d) Gas accumulation (TaO_x blanket). ..38

Fig. 2-14. (a) Image of 35 μm × 35 μm cells after electroforming (0 to ±7 V). The protrusions appear in one of the nine devices under test (upper left). (b) Attendant I–V characteristic of the electroforming operation for the Cu/TaO_x/Cu device with protrusions in (a). 39

Fig. 2-15. RESET-SET instability of Cu/TaO_x/Pt resistive memory devices. The I–V characteristics are divided into three sections: (1) Cu CF formation (2) Cu CF rupture (3) V_O CF formation. 41

Fig. 2-16. Schematic illustration of the incremental RESET strategies in (a) voltage pulse mode and (b) voltage sweep mode. 42

Fig. 2-17. Multilevel current jump in voltage sweeping mode. 44

Fig. 3-1. (a) Crossbar architecture for emerging nonvolatile memory devices. (b) NOR type flash memory..47

Fig. 3-2. Sneak current in nanocrossbar architecture [2]. 47

Fig. 3-3. Switching element structure proposed by Samsung [5]. 48

Fig. 3-4. (a) 1D1R and (b) 1T1R device cells in nanocrossbar architecture. 49

Fig. 3-5. Schematic diagram of I–V characteristics of (a) memory switching and (b) threshold switching devices [7]. 50

Fig. 3-6. (a) Cross-sectional view of Cu/TaO_x/δ-Cu/Pt volatile resistive switching cells. (b) Fifteen consecutive volatile switching curves of a Cu/TaO_x/δ-Cu/Pt device in log scale.……...52

Fig. 3-7. (a) Conceptual view of the Cu^+ and Cu fluxes in volatile switching devices. (b) Resistive state transition during the volatile switching operations. For curves 1, 2, and 3, the sweep is halted at a small but non-zero voltage. 54

Fig. 3-8. (a) I–t characteristics of the volatile device. The device is biased at constant voltages with the step of 0.025 V. (b) Dependence of switching time on bias voltages of the volatile Cu bridge. 56

Fig. 3-9. (a) V_{SET} of volatile switching devices at different ramp rates. (b) Dependence of R_{ON} on compliance current of the volatile Cu bridge. 58

Fig. 3-10. R_{OFF} at different device area. R_{OFF} decreases with the area, which indicates the switching in OFF-state is homogeneous across the device cell. Very high HRS/LRS ratio is also achieved in the device. 59

Fig. 3-11. R_{ON} at different device area. R_{ON} does not depend on device area, which indicates the filamentary type switching in the devices...59

Fig. 3-12. Nonvolatile switching of Cu/TaO_x/δ-Cu/Pt devices at high compliance current of 1 mA. 60

Fig. 3-13. Appllication of volatile switching Cu/TaO_x/δ-Cu/Pt as selection devices..61

Fig. 3-14. (a) R_{ON} and R_{OFF} distributions of volatile (V) and nonvolatile (NV) devices. (b) V_{SET} distribution of volatile and nonvolatile devices...62

Fig. 3-15. Comparison between Cu/TaO_x/Pt devices and Cu/TaO_x/δ-Cu/Pt nonvolatile devices. The thickness of d-Cu layer is 3.5 nm. With thin δ-Cu layer, the devices are nonvolatile memory and the δ-Cu layer provides nucleation sites for Cu ions. (a) R_{ON} and R_{OFF} distribution of Cu/TaO_x/δ-Cu/Pt devices. (b) V_{SET} and V_{RESET} of

$Cu/TaO_x/\delta$-Cu/Pt devices. (c) R_{ON} and R_{OFF} distribution of Cu/TaO_x/Pt devices. (d) V_{SET} and V_{RESET} of Cu/TaO_x/Pt devices. 63

Fig. 4-1. Device structure and I–V characteristics of complementary resistive switches [7]………...66

Fig. 4-2. (a) The chaotic circuit based on one memristor (canonical Chua's oscillator). (b) The chaotic circuit based on two memristors in antiparallel. The elements m, m_1, and m_2 represent memristors [13]. 67

Fig. 4-3. (a) The device structure of anti-parallel resistive switches (APS). (b) Layer structure of a single switch. The shown layer thicknesses are not drawn to scale. (c) The bipolar switching characteristics of a single Cu/TaO_x/Pt cell. The set voltage is 1.05 V and the reset voltage is −1.11 V. The set and reset voltages of Cu/TaO_x/Pt cell are typically ± (1 to 2) V and the reset current is 1 to 5 mA. 68

Fig. 4-4. I–V characteristics of two anti-paralleled resistive switches. The set and reset voltages are −2.0 V and 1.34 V for switch 1, and 1.72 V and −1.12 V for switch 2. On the positive switching side, cell 1 switched off before cell 2 switched on. With negative voltage bias, cell 2 switched off before cell 1 switched on. The compliance current is 2 mA for the positive switching and 5 mA for the negative switching. 70

Fig. 4-5. I–t characteristic of APS device. The bias voltage is 2.5 V. The duration of high resistance state is 1.5 s. 72

Fig. 4-6. I–V characteristics of anti-paralleled resistive switches different from those in Fig. 4-4. $R_{ON}(1) = 64\ \Omega$ when CC = 15 mA, and $R_{ON}(2) = 162\ \Omega$ when CC = 50 mA…………...73

Fig. 4-7. (a) Cu and V_O bridges in the same device cell. (b) One switching cycle of anti-parallel switching Cu and V_O CFs in a single 10 μm Cu/TaO_x/Pt cell. Multiple switching cycles have been measured in the voltage sweeping mode........................74

Fig. 4-8. Multiple switching cycles of APS in single devices. Steps 1 to 4 are the same as Fig. 4-7………..76

Fig. 4-9. Conceptual illustration of three cascaded resistive switches. TE and BE mean the top electrode and bottom electrode. Orange, blue and green materials represent Cu, TaO_x, and Pt...76

Fig. 4-10. Schematic illustration of the SET process of cascaded resistive switches..77

Fig. 4-11. Current characteristics as a function of time of two serially connected resistive switches under a collective voltage stress of 0.5 V......................................78

Fig. 4-12. Current characteristics as a function of time of two serially connected resistive switches under a collective voltage stress of 1.5 V. The inset shows switching behavior of the 2nd individual cell..79

Fig. 4-13. Current characteristics as a function of time of three serially connected resistive switches under a collective voltage stress of 1.4 V......................................80

Fig. 4-14. (a) Time for each SET process and (b) ON-state resistances for each current level of three serially connected resistive switches under a collective voltage stress of 1.4 V………...82

Fig. 4-15. Schematic cross section of integrated cascaded resistive switches in the crossbar array..84

Fig. 5-1. Schematic illustration of physical mechanisms of SET process in a CBRAM cell. Red circles represents Cu atoms and cations. Blue circles represent electrons. The yellow rectangle represents the solid electrolyte. The "+" and "–" signs represent the voltage polarity relative to 0 V. 87

Fig. 5-2. Quantum conduction observed in I–V characteristic of $Cu/TaO_x/Pt$ devices. The sweep rate ν is 0.002 V/s. $G_0 = 2e^2/h$, where e is the elementary charge and h is the Planck constant. 88

Fig. 5-3. I–V characteristics of a 10 μm ×10 μm $Cu/TaO_x/Pt$ resistive switching device. The voltage sweep rates ν are 0.04 V/s, 0.1 V/s and 2 V/s. The dimension of the measured device cell is 10 μm by 10 μm and the compliance current is 1 mA......90

Fig. 5-4. LRS R_{ON} for different sweep rates. The current compliance is 1 mA...........91

Fig. 5-5. Conceptual I–V and V–t characteristics. (a) Voltage drop on the device cell with time. (b) Cell voltages with different voltage sweep rates. V_C is the bias voltage on the device cell and R_{ON} is the final LRS resistance. ν is the voltage sweep rate and $V_{SET} = \nu t_{SET}$. Different SET times are labeled as $t_{SET(i)}$. 91

Fig. 5-6. Dependence of ON-state resistance on compliance current for $Cu/TaO_x/Pt$ devices. The dash line is the fitting curve for $R_{ON} = 0.17/I_{CC}^{0.998}$. 92

Fig. 5-7. Dependence of SET voltage on voltage sweep rate for the $Cu/TaO_x/Pt$ devices. The horizontal dash line is the saturated SET voltage which is 0.17 V. The inclined dash line is the fitting curve for the SET voltage at high sweep rates. 93

Fig. 5-8. Dependence of SET time on voltage sweep rate. t_{SET} is proportional to ln(ν)/ν and thus increases as ν decreases. 95

Fig. 5-9. I–V characteristics of $Cu/TaO_x/Pt$ devices at low sweep rates. The compliance current is 1 mA. The device current does not reach the compliance current at the SET voltage……..96

Fig. 5-10. LRS R_{min} for different sweep rates. The current compliance is not applied.96

Fig. 5-11. Conceptual I–V characteristic of resistive devices. If there is no current compliance, the device ends in a constant resistance. The R_{ON}–I_{CC} relation is invalid if the compliance current is set in the region above the dashed line. 97

Fig. 5-12. (a) I–V characteristic of a 10 μm ×10 μm $Cu/TaO_x/Pt$ resistive switching device. The voltage sweep rate is 0.02 V/s. (b) Experimental and simulated I–V characteristics of the resistance state transition. The quasi-static voltage sweep is applied on the $Cu/TaO_x/Pt$ device. The time interval between two experimental data points is 50 ms and the voltage step is 1 mV. 99

Fig. 5-13. (a) Geometry of the truncated conical filament. The electric field depends on the position h away from the filament tip. L is the length of the filament, h is the height of the top part, r and R are the radii of filament top and bottom respectively. V(L) is the voltage drop on the filament. V(L) and V(L–h) are voltages drop on the top and bottom parts (V(L)=V(h)+V(L–h)). (b) Conceptual view of the metallic contact, radial growth of filament, and the local electric field in the $Cu/TaO_x/Pt$ CBRAM device. V(h) and R(h) are voltage drop and resistance of the top part filament, respectively. V_{ap} is the voltage between Cu and Pt electrode and I is the current. The arrow lines represent the electric field. The denser the arrow lines, the higher the local electric field...101

Fig. 5-14. Voltage distribution along the axial direction of filament. The slopes of red and blue lines represent the approximate electric field at the top and bottom of the filament………. 103

Fig. 5-15. (a) Simulated growth rates of the top and bottom of filament. The initial growth rate of filament tip is extremely high whereas the growth rate of filament base is close to zero. At the end of radial growth, the two growth rates stabilize and converge. (b) Simulated radii of the top and bottom of filament. The final radii of filament tip and base are close rendering a more cylindrical geometry. 108

Fig. 5-16. (a) Dependency of device resistance and current on radial growth time. The time of 0 s is recorded when the HRS to LRS transition starts (current higher than 15 μA in Fig. 1). (b) Experimental and simulated resistance-current relation in the transition region between HRS and LRS..108

Fig. 5-17. Experimental and simulated multilevel switching property of $Cu/TaO_x/Pt$ devices. The ON-state resistance R_{ON} is inversely proportional to the compliance current I_{CC}…..109

Fig. 5-18. Simulation of CF voltage decrease with time due to the continuous radial growth in the current compliance regime. The voltage decreases until the voltage constant K is reached. 110

Fig. 5-19. Continuous radial growth time for different compliance current level. 111

Fig. 5-20. Simulated I–V characteristics with different thermal models...................113

Fig. 6-1. Cation concentration in CBRAM devices in two extreme cases: (a) Uniform distribution when reduction reaction is the rate-limiting process. (b) C_I = 0 when transport is the rate-limiting process. 118

Fig. 6-2. Potential barriers seen by an ion in solid electrolyte under high electric field. The electric field distorts the random ion jump between potential wells. The unbalanced ion hopping results in ion current. 120

Fig. 6-3. Simulation of 16 nm TaO_x devices at 298 K. The voltage ramp rate is 1 V/s. (a) Cu ion distribution in TaO_x at different times. The simulation shows most growth of the nanobridge happens within a narrow voltage range. (b) Voltage distribution in TaO_x for the Cu ion distributions given in (a). The electric field enhancement at the bridge front is within 20%. 124

Fig. 6-4. (a) Simulated and measured J–V characteristics of Cu/TaO_x/Pt CBRAM at different temperatures. (b) Simulated dependence of SET voltage on operating temperature for Cu/TaO_x/Pt cell. The inset shows the experimental SET voltages as a function of temperature [13]. 124

Fig. 6-5. Simulated (a) J–V characteristics and (b) electroforming voltages of Cu/TaO_x/Pt CBRAM for different oxide thickness. 126

Fig. 6-6. (a) Simulated J–V characteristics of Cu/TaO_x/Pt CBRAM at different trapping densities. (b) Simulated J–V characteristics of Cu/TaO_x/Pt CBRAM at different widths of fixed charge layer. 126

Fig. 6-7. Electrochemical dissolution in bipolar and unipolar switching. (a) SET process (b) RESET process in bipolar switching (c) RESET in unipolar switching. 127

Fig. 6-8. Cumulative probability of RESET voltages of bipolar and unipolar switching for Cu filament. The V_{RESET} in bipolar switching is mirrored to its positive magnitude. It shows the cumulative probability is almost symmetrically distributed across the V_{RESET} range [15]. 128

Fig. 6-9. Three-dimensional model for resistive switching simulation. 130

Fig. 6-10. Simulated Cu concentration at different time during CF dissolution. The color represents the ion concentration and the scale is the same as that in Fig. 6-9..131

Fig. 6-11. Simulated device current at different time in RESET process. 132

Fig. 6-12. Simulated temperature profiles of unipolar and bipolar switching in $Cu/TaO_x/Pt$ CBRAM devices. (a) Thomson coefficient μ = T/200 (μV/K). (b) Thomson coefficient μ = T (μV/K). The length of simulation domain is 32 nm. 136

List of Tables

Table 1-1 Summary of the flash memory and emerging memory technologies according to the ITRS roadmap [1]. Red, orange, and green colors mean poor, moderate, and good. 5

Table 2-1 Summary of Electron Beam Deposition for Cu/TaO_x/Pt Devices. 24

Table 3-1 Summary of Electron Beam Deposition for Cu/TaO_x/δ-Cu/Pt Devices. 53

Table 5-1 Values of parameters in the radial filament growth model. 107

Table 5-2 Parameters in simulation models considering thermal effect...................114

Table 6-1 Parameters for the simulation model of forming process in Cu/TaO_x/Pt CBRAM cells..123

Table 6-2 Simulated growth rate of Cu nanobridge in Cu/TaO_x/Pt CBRAM cells...125

Table 6-3 Values of parameters in the Fourier equation. 135

Chapter 1 Introduction

This chapter starts with an introduction to the challenges and opportunities for the scaling of memory devices. The conductive bridge resistive switching devices are highlighted for their memory and non-memory applications. After examining the surveyed results from literature, the fundamentals of resistive switching are reviewed. The materials and switching mechanisms are addressed for solid electrolytes based resistive devices. Finally, the organization of the dissertation is presented.

1.1 Scaling Challenges in Flash Memory

In the past 25 years, the semiconductor device scaling has been very successful according to Moore's law, leading to the shrinkage of integrated circuit feature size (channel length/half-pitch) from 1 μm to 20 nm. The one-dimensional scaling factor is about 0.7 for the feature size in every two years which yield a factor of 0.5 for the device footprint [1]. The smaller feature size allows more transistors on a single chip, more functions of the circuits, and lower cost for each function. The scaling of memory devices is even more aggressive than logic devices due to the simple architecture of random access memory and fierce competition in the market.

Nowadays, zetta bytes of information are stored in hard disk drives, DRAM, flash memory (NAND/NOR), and solid state drives. More and more storage spaces are demanded for smart phones, tablet computers, web search, cloud computing, etc. Among various storage devices, non-volatile memory (NVM) has recently attracted a lot of attention from both industry and academia [2]. NVM can store information after

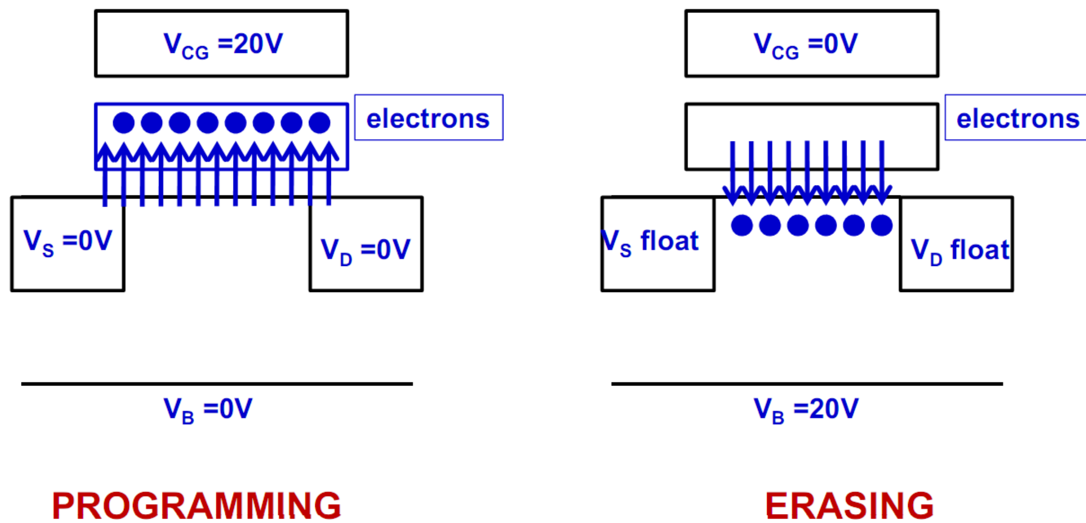

Fig. 1-1. Device structure and operating mechanism of flash memory (floating gate device). In the flash memory device, a floating gate is inserted in the oxide of MOSCAP. A high write/erase voltage is needed to charge/discharge the floating gate. Under the high electric field, electrons can tunnel through the gate oxide between the Si substrate and floating gate.

removal of power supply, which is very important for energy-efficient electronics and computing. It can also reduce the weight and increase the speed of portable personal devices. As a result, NVM devices are being developed more rapidly than any other data storage technologies.

The state-of-the-art NVM is flash memory, including NAND and NOR [3]. Flash memory was invented by Toshiba in 1980s. The basic device structure and operating mechanism are shown in Fig. 1-1. The flash memory device is a MOSFET with an additional metal gate which is known as floating gate. When a high voltage (~20 V) is applied to the control gate (non-floating), the electrons can rearrange their migrating direction and arrive at the floating gate by Fowler-Nordheim tunneling. The electrons stay on the floating gate after the gate voltage is removed, since the floating gate is surrounded by insulator (SiO_2) and there is no way to leak out. Because of the charges

stored on the floating gate, the threshold voltage of the device is significantly changed and the two states of the device (with and without charges on the floating gate) can be identified as "0" and "1" for data storage.

Although flash memory is extremely successful nowadays, it is still not the ideal solution for NVM applications. This is because (1) Flash memory is slow. The write time is in μs range, which does not satisfy the increasing high-speed requirement. (2) Flash memory requires a high write voltage. The electron tunneling needs a high operation voltage which is not energy-efficient for low power applications. (3) Flash memory is essentially a MOS-based device. This means the scaling encounters tremendous technical barriers beyond 20 nm. (4) Endurance is limited. Flash memory is good for personal devices, but industrial equipment requires more reliable storage hardware. Therefore it is desirable to develop a high speed, low power, high endurance, sub-20 nm nonvolatile memory [4]. So far, no NVM device can fulfill all those requirements for a "universal" memory scaled below the size of 20 nm.

1.2 Opportunities for Resistive Memory

In order to extend Moore's law in the next few decades, different classes of new NVM technologies have been proposed and demonstrated. Different from the conventional metal-oxide-semiconductor architecture, these technologies take advantage of novel functional materials and 3D device structures. The phenomena in nanostructures and quantum physics are extensively utilized for the emerging memory devices. Besides NVM applications, the computing logics are also being developed based on the unique memory device characteristics.

1.2.1 Emerging Memory Technologies

In recent years, many emerging nonvolatile memory technologies are invented challenging the dominant position of flash memory. Ferroelectric memory (FeRAM), oxide resistive memory (RRAM), conductive bridge resistive memory (CBRAM), phase change memory (PCM), NEMS memory, and spin-transfer torque magnetic memory (STTRAM) are all intensively being investigated and developed. Phase change memory utilizes the local heating effect to induce the material phase transition between the amorphous and crystalline states [5]. Thus the device resistance changes according to the material phase transition. The ferroelectric memory takes advantage of the ferroelectric phenomenon [6]. The NEMS memory is implemented by the movement of nano-sized mechanical switches [7]. Among the emerging technologies, the resistive memory and spin-transfer torque memory (shown in Fig. 1-2) are two most promising candidates as the successor of flash memory [8], [9]. CBRAM employs nanoionic redox reaction to change the resistance state, whereas STTRAM uses electron spins in the current to revolutionize the traditional magnetic memory.

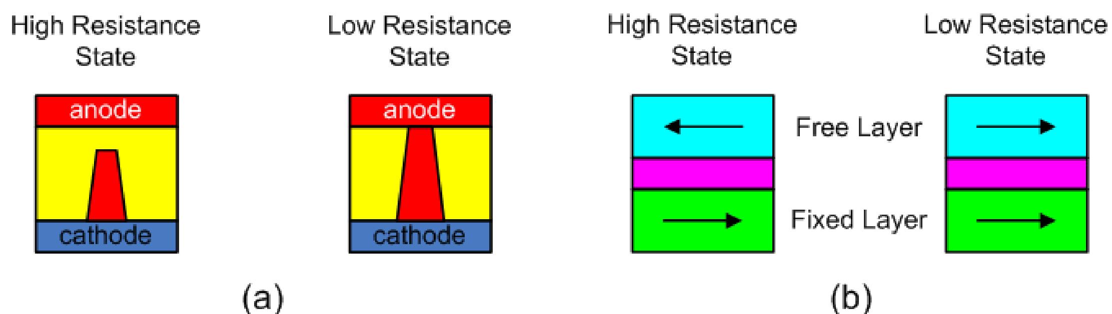

Fig. 1-2. (a) Redox memory, also known as CBRAM. It is based on the redox reaction in a thin solid electrolyte film sandwiched between two metal electrodes. (b) Spin-transfer torque memory which is based on magnetic tunneling junction CoFeB/MgO/CoFeB.

CBRAM and STTRAM are both based on multi-layer thin film stack structure and can be integrated in the back end of line of CMOS process. The compact cell size of both devices can be decreased to $4F^2$ in the crossbar array. Here F is the feature length defined by the lithography process. The state-of-the-art and emerging technologies are summarized in Table 1-1 according to ITRS roadmap [1].

Table 1-1 Summary of the flash memory and emerging memory technologies according to the ITRS roadmap [1]. Red, orange, and green colors mean poor, moderate, and good.

Parameter	Flash Memory	PCM	STTRAM	Resistive Memory	FeRAM	NEMS Memory
Scalability	orange	green	orange	green	orange	red
MLC	green	green	red	green	red	red
Endurance	green	orange	green	green	green	red
3D integration	orange	green	orange	orange	red	red
Fabrication cost	green	green	orange	orange	orange	red
Write Energy	orange	red	orange	orange	green	orange
Write Voltage	red	green	green	green	green	green

1.2.2 Memristor

In 1971, based on symmetry arguments Leon Chua proposed a fourth fundamental electrical element besides resistor, capacitor, and inductor [10]. The new element is

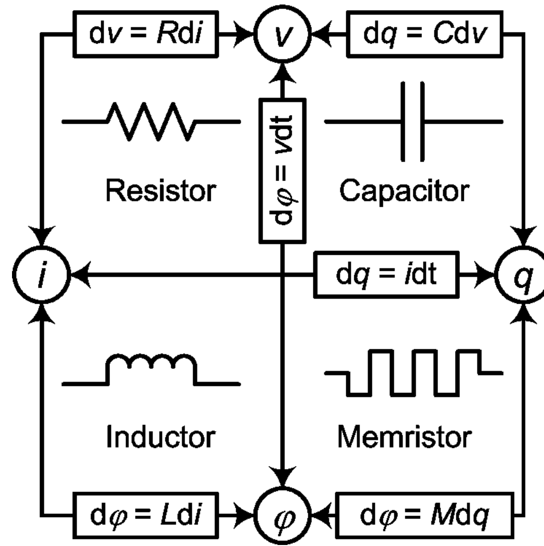

Fig. 1-3. The four fundamental two-terminal circuit elements: resistor, capacitor, inductor, and memristor [11].

named memristor (short for memory resistor) which links magnetic flux φ and charge q via a single-valued function M(q). M(q) is called memristance. In 2008, Strukov et al. pointed out that the Pt/TiO_2/Pt device is a memristor [11]. Later Chua confirmed that all resistive switching devices are memristors no matter what mechanism they are built upon [12]. Fig. 1-3 shows the relations connecting pairs of the electric current i, voltage v, charge q, and magnetic flux φ [11].

The basic mathematical equations of the i–v characteristic for a current-controlled memristor are

$$v = R(w)i \tag{1-1}$$

$$\frac{dw}{dt} = i \tag{1-2}$$

where w is the state variable of the device and R is the generalized resistance. It can be claimed that the state of the memristor is not only determined by the device itself, but also the external bias conditions. The history of the bias conditions and previous

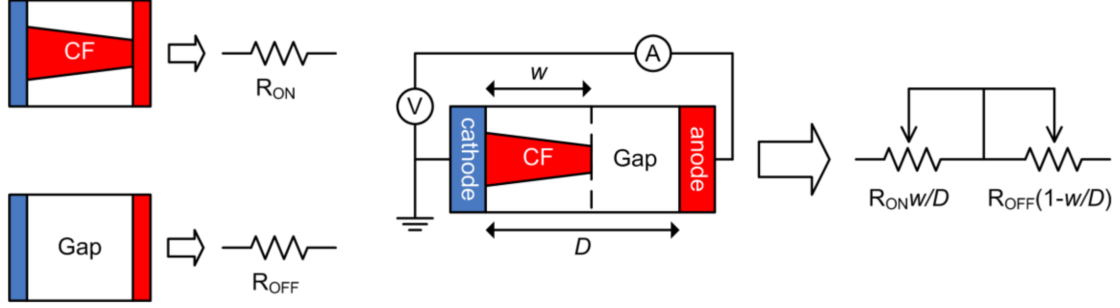

Fig. 1-4. Simplified equivalent circuit of the coupled variable-resistor model for a memristor [11].

device state will determine the following state. Therefore the input and output are coupled in a way different from all the other circuit elements. In general, a memristive system is described by equations

$$v = R(w, i)i \tag{1-3}$$

$$\frac{dw}{dt} = f(w, i) \tag{1-4}$$

where w is a set of state variables and R and f are explicit functions of time.

A resistive switching memory device can be viewed as a serial connection of a high resistance part and a low resistance part as shown in Fig. 1-4 [11]. The boundary of the two resistive parts moves as the external voltage bias varies. The physical mechanism of the moving boundary is the ion migration in high electric field in the electron insulating and ion conductive solid electrolyte. The mathematical models of the resistive switching phenomenon are

$$v(t) = \left(R_{ON} \frac{w(t)}{D} + R_{OFF} \left(1 - \frac{w(t)}{D} \right) \right) i(t) \tag{1-5}$$

$$\frac{dw(t)}{dt} = \mu_V \frac{R_{ON}}{D} i(t) \tag{1-6}$$

$$w(t) = \mu_V \frac{R_{ON}}{D} q(t) \tag{1-7}$$

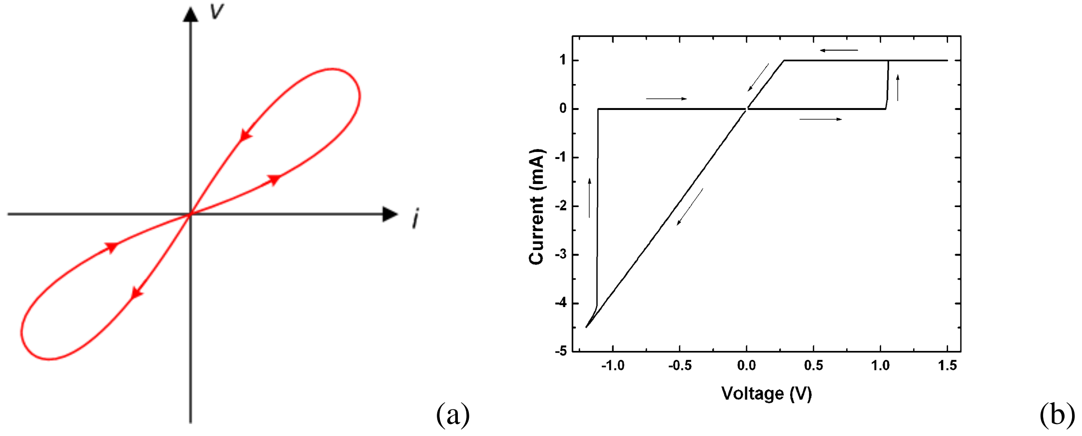

Fig. 1-5. Pinched hysteresis loop as a signature of memristors. (a) Schematic diagram. (b) Experimental I–V of a $Cu/TaO_x/Pt$ device.

$$M(q) = R_{OFF}\left(1 - \frac{\mu_V R_{ON}}{D^2} q(t)\right) \tag{1-8}$$

where R_{ON} and R_{OFF} are the low and high resistances of the memristor, D is the thickness of solid electrolyte, w is the thickness of doped or low resistive region of solid electrolyte, μ_V is the average ion mobility, q is the electronic charge, and M the memristance. A typical signature of memristors is the pinched hysteresis loop (figure "8" alike) as shown in Fig. 1-5. The resistive switching memories, including ReRAM and CBRAM, all show such kind of I–V characteristics. Therefore they are considered as memristors.

An immediate application of memristor is the nonvolatile memory because it can retain the memory states and data in power-off mode. The memristors can even replace transistor in the future CPU and reduce the chip footprint. The binary logic can be implemented with the material implication (IMP) operation [13]. It also attracts great interest in the chaotic circuit [14], neuromorphic computation [15], and neural networks.

1.2.3 Synapse for Neuromorphic Computation

A fascinating application of resistive memory device is the neuromorphic computation. The vision is to develop electronic machine technology that scales to biological level. IBM has reported the simulation of a cat brain based on software technology. A more efficient way of mimicking a brain is to implement it with special hardware. The sudden change of resistance state of resistive memory can be used to emulate the synapse in neural systems [16]. Therefore resistive switches can be used for connecting CMOS neuron circuits, like the synapses and neurons in a brain. This unique behavior enables the implementation of computing hardware that is physically similar to a mammalian brain. The prototyping devices and circuits have been demonstrated on both CBRAM and RRAM [16], [17]. The controllable gradual resistance change is correlated to the learning ability of neural systems [18]. Electrical pulse has also been generated by connecting two resistive devices antiserially [19]. In general, the research and development of neuromorphic computation is still in the starting phase and a lot of problems have not been solved. However, if the development succeeds someday, this innovative computing machine will revolutionize the computer industry and the artifical intelligence research.

1.3 Fundamentals of Resistive Memory

The early research of resistive switching phenomenon in metal/insulator/metal (MIM) structures started in the 1960's and proceeded in the following two decades [20]. The renaissance of resistive switching is from the late 1990's to nowadays,

accompanying the ever increasing demand for data storage capacity and the invention of resistive memory [21], [22]. The device structure of resistive memory is thin film stacks consist of a metal anode, an insulator, and a metal cathode which form an electrochemical cell. For CBRAM, the two metal electrodes are made of different materials. The anode material is Cu or Ag which are active metals dissolvable in the insulator [23]. The cathode material is usually Pt or W, which are the stopping barriers of Cu and Ag cations. The solid electrolytes of Cu or Ag are selected as the insulator layer. In fact, the electrolyte layer is insulating for electrons but conductive for ions. For RRAM, the two metal electrodes could be symmetric, such as $Pt/TiO_2/Pt$ [24]. An inert material Pt is used and therefore no metal ion enters the insulator. In this type of resistive memory, oxygen vacancies are responsible for the conduction. The insulator materials are usually oxide electrolytes. Because the operation of resistive memory relies on ions, this type of device is also called nanoionic device [25]. The development and application of CBRAM is the goal of this dissertation.

1.3.1 Resistive Switching and Electrochemistry

The resistance of a CBRAM device can be measured between the two electrodes. When the resistance of the two-terminal device is high, the memory state is “0” which is called high resistance state (HRS), or OFF-state. The corresponding device resistance is R_{OFF}. The HRS remains if there is an insulating material between the anode and cathode. On the contrary, when the device resistance is low, the memory state is “1”, which is called low resistance state (LRS), or ON-state. The corresponding device resistance is R_{ON}. R_{ON} can be controlled by an external selection

device through the compliance current I_{CC}. This R_{ON}–I_{CC} relation is the foundation of multilevel cell of resistive memory. The LRS remains until an erase operation is applied to the device. The device state transitions from HRS to LRS in the so-called SET or write process, whereas it transitions from LRS to HRS in the so-called RESET or erase process. In both SET and RESET processes, there are threshold voltages to toggle the resistance state, which are called SET voltage (V_{SET}) and RESET voltage (V_{RESET}).

Resistive memory devices show a low resistance state independent of device cell sizes. Therefore a filamentary switching mechanism is proposed for the electroforming and SET processes in the resistive materials. The conductive filament (CF) is a local phenomenon in the solid electrolyte that has been confirmed with the conductive atomic force microscope [26]. Fig. 1-6 shows a switching cycle of a CBRAM device. In CBRAM, the metal ions can dissolve into the solid electrolyte from the active anode, and accumulate at the inert cathode. The accumulated ions nucleate and grow to form a nanosacle metallic conductive filament (CF) connecting

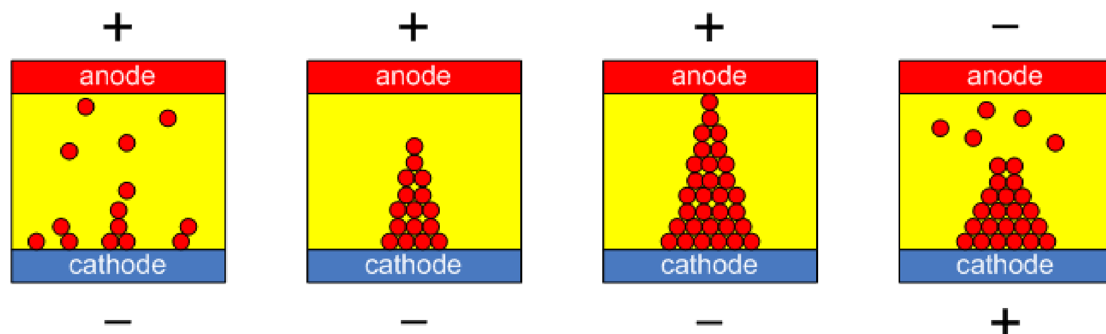

Fig. 1-6. Schematic illustration of switching processes of conductive bridge resistive devices. Red circles represents Cu atoms and cations. The yellow rectangle represents the solid electrolyte. The "+" and "–" signs represent the voltage polarity relative to 0 V.

both electrodes. When the nanofilament forms, the resistance between two electrodes is low, and this state is named low resistance state (LRS). The metallic nanofilament will not disconnect until there is enough energy to remove metal atoms from it. In fact, CBRAM has shown excellent retention at elevated temperature up to 85 °C, implying a stable metallic filament forms in SET process [27].

For a newly built fresh device cell, an electroforming process is needed to prepare the device. A forming voltage V_{form} is used to switch the device from its high resistance state to its low resistance state. The forming voltage is usually higher than the regular SET voltage of the device, possibly because the partial filament exists in the following SET process. Special treatments during the device fabrication have also been demonstrated in order for eliminating the forming process [28], [29].

There are two switching methods for resistive memory: static switching (I−V) and dynamic switching (I–t). In static switching, the bias voltage is ramped continuously from 0 to a high value and the current rises abruptly at the threshold. The SET voltage (V_{SET}) is the characteristic parameter for the static switching. In dynamic switching, voltage pulses are applied on the device and the current rises under the constant voltage bias during the pulsing interval. The SET time (t_{SET}) is the characteristic parameter for the dynamic switching. t_{SET} includes circuit delay time, cation nucleation time, and filament growth time [30]. The exponential dependence of t_{SET} on V_{SET} is usually observed because of the redox process.

The resistive switching is categorized to bipolar and unipolar schemes, as shown in Fig. 1-7. In case of bipolar switching, write and erase operations occur under

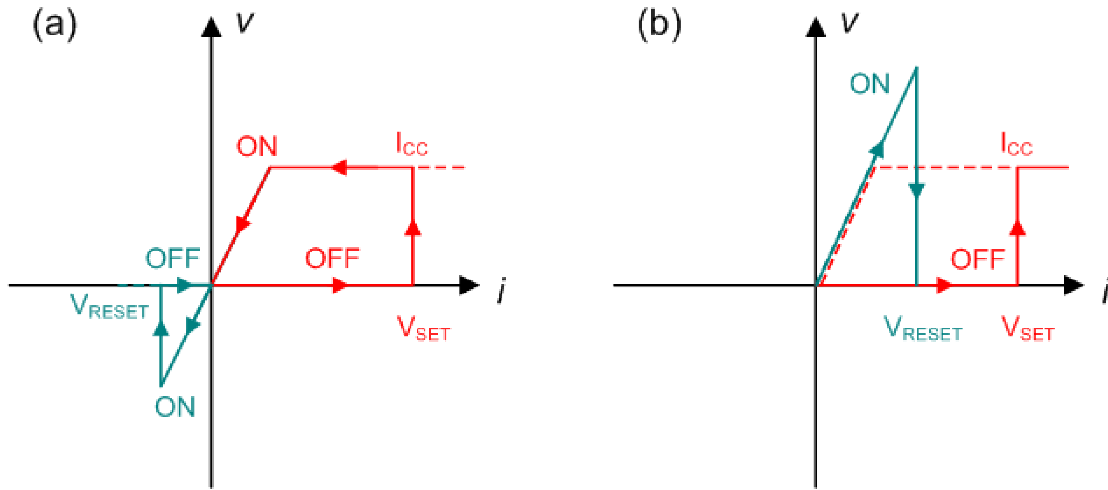

Fig. 1-7. Illustration of I–V characteristics of (a) bipolar switching and (b) unipolar switching.

opposite voltage polarities. If V_{SET} is positive, V_{RESET} is negative and vice versa. Typical examples are Cu- and Ag-migration based memory cells. Very low switching current has been achieved on Cu and Ag devices with this switching scheme [31], [32]. In case of unipolar switching, write and erase operations occur under the same voltage polarity. Typical examples are Pt/NiO/Pt and Pt/TiO_2/Pt [33], [34]. Mostly, the absolute value of RESET current (I_{RESET}) is higher than that of SET current (I_{SET}, namely I_{CC}), but V_{RESET} is lower than V_{SET}. Due to the high current, the RESET process is probably thermally assisted. Bipolar and unipolar switching can occur in the same system, for example Pt/Ta_2O_5/Pt [35]. In fact, the thermal and ionic effects take place at the same time during SET and RESET processes. I_{RESET} is much higher than I_{SET} for Cu/TaO_x/Pt devices implying the dominant thermal effect in RESET process. A high current flow through the nanofilament will generate significant Joule heating. The local temperature is so high that the Cu atoms quickly diffuse from the filament to the surrounding oxide and thus the nanofilament ruptures.

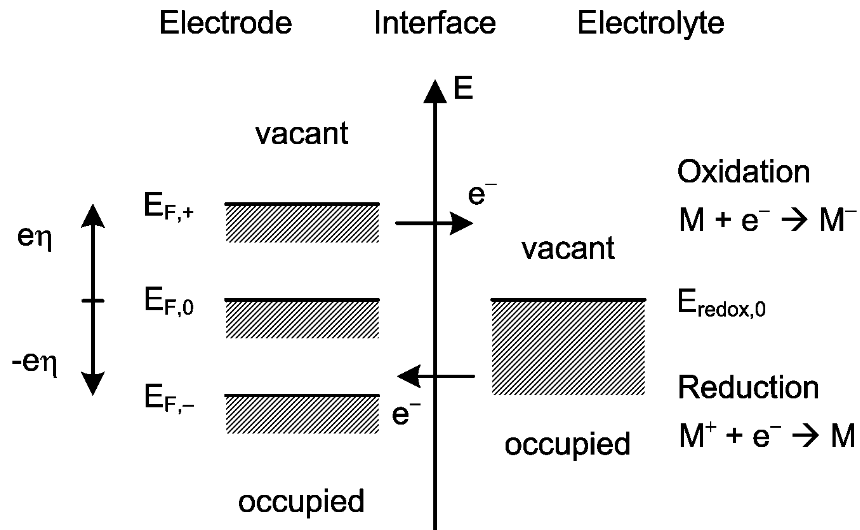

Fig. 1-8. Graphic view of the electron transfer in redox reactions at the electrode/electrolyte interface.

The switching mechanism of resistive memory is essentially based on electrochemical reactions in solid-state nanostructures. Electrochemistry studies the chemical reactions at the interface of electrode and electrolyte. The electrode is an electron conductor whereas the electrolyte is an ion conductor. The electrochemical process is well known as oxidation-reduction (redox) reactions. The theory developed from liquid phase electrochemistry can be applied to analyze the solid phase cases, such as resistive memory.

The electrons transfer between the electrode and electrolyte in redox reactions. The root cause of redox is the difference of electrode and electrolyte Fermi levels. The situation of electron transfer is schematically shown in Fig. 1-8. The Fermi level separates the occupied and vacant states for electrons. When a potential difference appears between the electrode and electrolyte, the electronic states shift between both sides of the interface. Therefore electrons transfer from occupied states in one phase to vacant states at the same energy level in the other phase. In fact, the electron

transfer only occurs in a narrow energy range around the Fermi level of metal electrode because of the sharp transition between occupied and vacant states [36].

The reaction kinetics is described by the Butler-Volmer equation. According to the Butler-Volmer equation, the oxidation and reduction current (two half reactions) exist at each electrode/electrolyte interface at the same time. The two currents balance each other and the overall current is zero if there is no external voltage (so-called overpotential). In the meanwhile, an equal number of metal ions cross in both directions across the electrode/electrolyte interface. With an external voltage bias, one of the currents will overwhelm the other, and therefore either oxidation or reduction reaction is observed at the interface.

1.3.2 Materials of Solid State Electrolytes

Many materials have shown resistive switching properties. Extensive research has been done to search the best material system for CBRAM [23]. Typical electrolyte materials are oxide (SiO_2, WO_3, and Ta_2O_5) and chalcogenide (Cu_2S, Ag_2S, and GeSe). In general, they are mainly divided into two categories: oxide electrolyte and Ag/Cu electrolyte. Oxide, chalcogenide, and halide are the most important material systems for resistive switching.

Anion redox reaction and migration often induce resistive switching in transition metal oxides. The typical materials are NiO, TiO_2, $SrTiO_3$, Nb_2O_5, $Pr_{0.7}Ca_{0.3}MnO_3$, $La_{0.7}Ca_{0.3}MnO_3$, HfO_2, CeO_2, and Al_2O_3 [33], [34], [37]–[43]. The oxygen anions can migrate in these so-called oxide electrolytes. The oxygen vacancies left form the conductive filament showing the resistive switching. These oxides can be mixed to

increase the ionic conductivity, such as $Pr_{1-x}Ca_xMnO_3$, $La_{1-x}Ca_xMnO_3$, $Zr_{1-x}Ca_xO_{2-x}$, and $Ce_{1-x}Gd_xO_{2-x/2}$. Because of the valence mismatch, oxygen vacancies have to be generated for electrical neutrality, and therefore the ion conductivity is higher.

Metal cation redox reaction and migration occurs in solid electrolytes of that particular metal. The solid electrolytes, or ion conductor of Ag and Cu are extensively studied. A broad range of inorganic compound materials show resistive switching property. Halide is one of them, such as $RbAg_4I_5$ and AgI [30], [44]. Chalcogenide is another class of solid electrolyte. GeSe, Ag_2S, Cu_2S, GeS_2 are investigated for resistive switching [32], [45]–[47]. The cation-based resistive switching is also often observed in good electron insulators, such as SiO_2, Ta_2O_5, HfO_2, Cu_2O, and WO_3 [48]–[52]. To improve the concentration of cations in the oxide, doping of Cu or Ag and annealing can be applied in the film deposition process [53]–[55]. In some experiments, nanoparticles are embedded in the electrolytes to confine the local filament growth [56]. Compared to oxygen vacancy based resistive memory, the switching mechanism for CBRAM is more straightforward and tangible. Besides inorganic materials, polymers can also be electrolytes for Cu or Ag and thus used for resistive switching [57]. This kind of ion conductor opens a door for resistive memory to the future flexible electronics.

1.4 Dissertation Objective and Organization

The objective of this work is to understand the physics of $Cu/TaO_x/Pt$ conductive bridge resistive device based on electrical characterizations and computational models,

and evaluate its applications to nonvolatile memory and memristor-based chaotic circuits.

This dissertation is organized in 7 chapters. Chapter 2 presents the fabrication and characterization of Cu/TaO_x/Pt resistive memory devices. The devices are designed in the crossbar layout and processed by electron beam evaporation and lift-off technology. The quasi-static I–V sweeping is used to characterize the electrical performance of the devices. Cu and oxygen vacancy (V_O) filaments are investigated under bias voltages with opposite polarities. Bipolar and unipolar switching modes are both demonstrated for Cu and V_O filaments.

Chapter 3 presents the volatile switching phenomenon of Cu/TaO_x/δ-Cu/Pt devices. By inserting a 6.5 nm Cu layer between the Pt electrode and TaO_x electrolyte, the devices show volatile switching at the compliance current of less than 100 μA. Switching time measurement shows the volatile switching is still due to the redox reaction and the formation of Cu nanobridge. A flux balance model is proposed to explain the phenomenon. This model is verified by the observation that the current diminishes when the bias voltage is suspended at a value close to zero volt. An application of volatile switching is the selection devices in the nanocrossbar architecture.

Chapter 4 presents the circuit elements based on Cu/TaO_x/Pt devices. Antiparallel and cascaded resistive switches were proposed and demonstrated. Antiparallel resistive switches show symmetric q-φ characteristic which can be used for memristive circuits.. The cascaded resistive switches change the resistance according

to the variation of external bias voltage. Three cascaded resistive switches show 4 resistance levels expanding over 6 orders of magnitude. This circuit element might be applied to simulate the highly nonlinear learning ability in neuromorphic computation and neural network.

Chapter 5 presents the physics of multilevel cell of CBRAM device. The voltage constant is identified as the minimum SET voltage, which is closely related to the materials, device structures, and process technologies. A computational model based on hopping mechanism is used to fit and explain the switching transition of metallic contact. The multilevel switching is attributed to the radial growth after a single atom metallic contact is formed during SET process. The validity of R_{ON}-I_{CC} relation is investigated and clarified according to the SET processes with various voltage sweeping rates. This relation is generally valid for the low current compliance regime.

Chapter 6 presents the phenomenological simulation model for the switching of cation-migration type resistive memory devices. The electroforming/SET process is simulated by solving ion transport equation, Farady equation, and Poisson equation simultaneously. A yield of 100% is assumed for the ion neutralization on the cathode. In the electroforming process, the ion transport is the rate-limiting process; in the SET process, the redox reaction is the rate-limiting process. The RESET process is simulated by solving diffusion equation and electroheating equation simultaneously. This is because the local heating induced by the high RESET current is an important contributing factor for the filament rupture. The Thomson heating effect has also been investigated as a heating source for RESET in the computational model.

Finally, Chapter 7 summarizes the conclusions of this work and recommends possible future areas of investigation.

Chapter 2 Characterization of $Cu/TaO_x/Pt$ Resistive Switching Devices

The $Cu/TaO_x/Pt$ switch is one of conductive bridge random access memory (CBRAM) devices. It also belongs to the generic concept of resistive memory. CBRAM is based on redox reactions of metal cations. Therefore it is also known as electrochemical metallization memory (ECM), atomic switch, or programmable metallization cell (PMC) [1]−[6]. Under high electric field, Cu ions dissolve and migrate in the TaO_x layer. These cations are stopped by the inert Pt electrode and accumulate to form a Cu nanofilament, or nanobridge. When the filament connects Cu and Pt electrodes, the memory state of the device switches from high resistance to low resistance. Another type of resistive memory is based on redox reactions of oxygen anions, which is known as RRAM, or valence change memory (VCM) [7]−[10].

2.1 Introduction

After years of development, the Cu interconnection is finally compatible with the Back-End-Of-Line (BEOL) of Si CMOS process. Therefore Cu is an ideal low cost material for the anode of resistive memory embedded in Si integrated circuit. Various oxides and chalcogenides are intensively being explored for the solid electrolyte of Cu ions. One of the important criteria is the electrolyte material must be also compatible to Si CMOS technology. Since resistive memory is embedded in BEOL, the oxide is the better material solution for the insulating purpose. Exotics generally do not diffuse out from oxide materials and there is less opportunity to contaminate the CMOS

process. Ta_2O_5 is selected in this research since it can improve the reproducibility of Cu-based CBRAM devices [11], [12]. It is also the oxide material used for the capacitor of DRAM and suitable for process integration. In this research, the Ta_2O_5 film is considered to be oxygen deficient (TaO_x) due to its e-beam deposition process. A parallel plate capacitor forms when the high-k dielectric TaO_x is sandwiched between micron-sized metal electrodes. Therefore the equivalent circuit of the $Cu/TaO_x/Pt$ stack is one resistor in parallel with one parasitic capacitor. The parasitic capacitance may generate transient charging current if the voltage slew rate is very high. However, in the DC characterization scheme, the bias voltage is slowly ramped up from 0 V to V_{SET}. The voltage sweep rate (dV/dt) is less than 2 V/s. The complete characterization process is quasi-static so that the transient current is minimized for our large area devices. The transient current flowing through the parasitic capacitance during the SET operation is estimated to be

$$\begin{aligned} i &= C\frac{dV}{dt} = \frac{\varepsilon_r \varepsilon_0 A}{d}\frac{dV}{dt} \\ &\leq \frac{25\times 8.854\times 10^{-12}\,F/m \times \left(10\times 10^{-6}\,m\right)^2}{30\times 10^{-9}\,m}\times 2V/s \\ &= 1.5\times 10^{-12}\,A \end{aligned} \tag{2-1}$$

where ε_r is the dielectric constant of Ta_2O_5, ε_0 the vacuum permittivity, A the cell area (100 μm^2), and d the thickness of TaO_x layer. It is negligible compared to the current flowing through the resistance in the equivalent circuit.

2.2 Fabrication Processes

The cross-section view of $Cu/TaO_x/Pt$ device structure is shown in Fig. 2-1. A thin Ti layer is deposited before Pt on the thermally oxidized SiO_2 in order to improve the

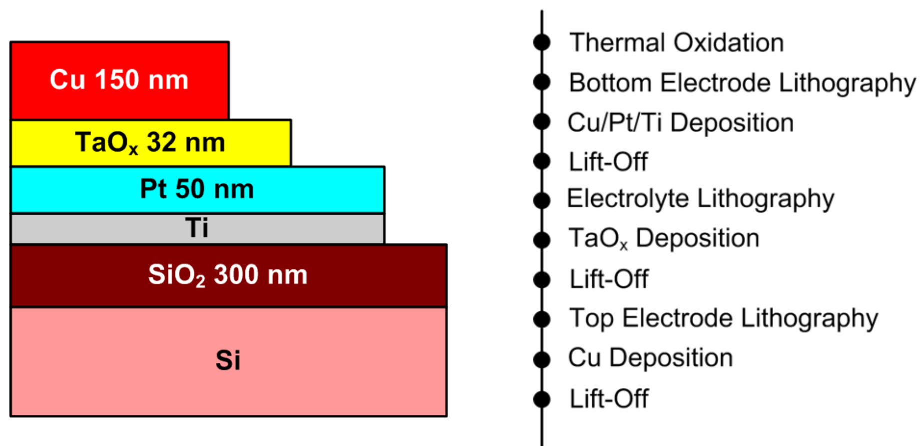

Fig. 2-1. Schematic layer structure of the cross section of Cu/TaO_x/Pt resistive memory device.

adhesion of Pt. The Cu anode is the finish layer exposed to the air and moisture. The fabrication process flow is shown in Fig. 2-2. The device cells are organized in a crossbar architecture which can achieve the minimum footprint. The Cu anodes and Pt cathodes are perpendicular to each other and each cross point is a device cell.

The Si substrate is thermally oxidized to provide an insulating SiO_2 layer as the foundation of resistive devices. The standard dry O_2/wet O_2/dry O_2 oxidation process is used. The electron beam (e-beam) evaporation is selected as the deposition method for Cu, TaO_x, Pt, and Ti layers. The melting points of those four materials are not high so that e-beam deposition is an effective way for manufacturing prototypes in a university lab. To avoid sophisticated dry etching steps, the lift-off technology is used for removing excessive materials and patterning the active region. Considering the requirement of lift-off, negative lithography is employed for defining the device active region. The MA-6 Karl Suss optical lithography in our lab can achieve the best resolution of 1 μm. Therefore the dimensions of resistive device cells are in μm range which is still suitable for demonstrating the generic device characteristics.

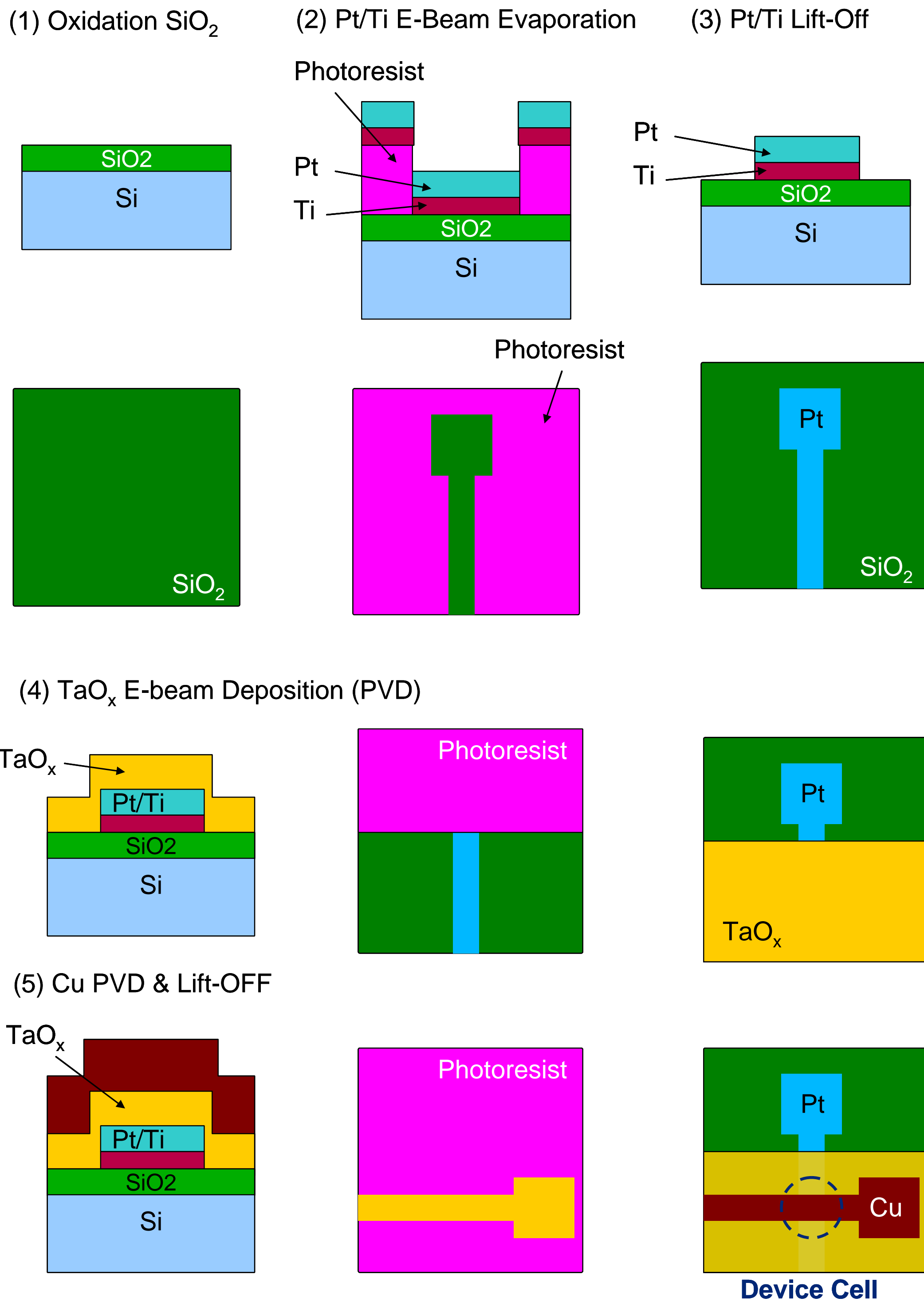

Fig. 2-2. Process flow of Cu/TaO_x/Pt conductive bridge resistive devices. (1) Thermal oxidation of Si substrate. (2) Lithography and Pt/Ti e-beam evaporation. (3) Pt/Ti lift-off. (4) Lithography, TaO_x e-beam deposition, and TaO_x lift-off. (5) Lithography, Cu e-beam deposition, and Cu lift-off.

The electron beam evaporation (PVD250) is illustrated in Fig. 2-3. The deposited material is melted in the crucible at the bottom of the chamber. The electron beam is generated from a tungsten filament (Telemark) and deflected to the graphite crucible. The vacuum pump maintains the low pressure in the PVD chamber. The substrate chuck rotates constantly at 5 rounds/min during deposition to improve the thickness uniformity of the deposited thin film. The evaporation is started when the chamber pressure reaches ~10^{-6} torr. The substrate temperature is monitored to be around 25 °C without heating the substrate chuck. The deposition rates and parameters of Pt, Cu, and TaO_x are listed in Table 2-1. The deposition rates are measured by quartz crystal microbalance in PVD, the Filmetrics F20 optical system, and the Dektak profiler. The purities of Cu, Ta_2O_5, and Pt evaporation pellets from Kurt J. Lesker Company are 99.99%, 99.95%, and 99.99%.

Table 2-1 Summary of Electron Beam Deposition for Cu/TaO_x/Pt Devices.

Material	Pt	TaO_x	Cu
Layer Thickness (nm)	50	32	150
E-Beam Deposition Rate (Å/s)	1	1	5
Melting Temperature (°C)	1768	1872	1085
E-Beam Current (mA)	180	150	120
E-Beam Base Pressure (Torr)	2×10^{-6}	2×10^{-6}	2×10^{-6}
Density (g/cm^3)	21.45	8.2	8.93
Z-ratio	0.245	0.3	0.437
Tooling Factor	140	140	140

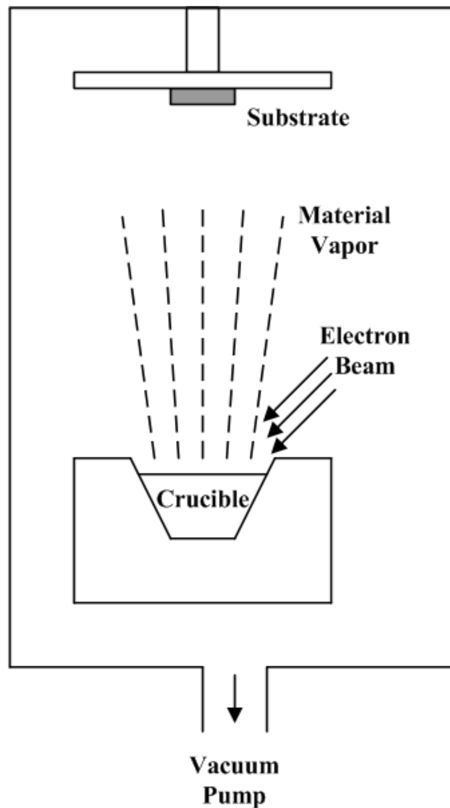

Fig. 2-3. Schematic illustration of the electron beam deposition.

2.3 Resistive Switching Based on Cu and Oxygen Vacancy Conductive Nanofilaments

The switching properties of Cu and V_O CF are characterized by quasi-static DC measurement with opposite polarities. The electroforming process is necessary for fresh devices. The forming voltage is generally 1~2 V higher than V_{SET}. The bias voltage sweeping mode is illustrated in Fig. 2-4. The Pt cathode of the device is grounded in the experiment and the positive or negative bias voltage is applied to the Cu anode. I–V characteristics of bipolar and unipolar switching in the Cu/TaO_x/Pt device are shown in Fig. 2-5. When the bias voltage sweeps from 0 V to negative values, the device transitions from HRS to LRS at about −2 V. A very high current

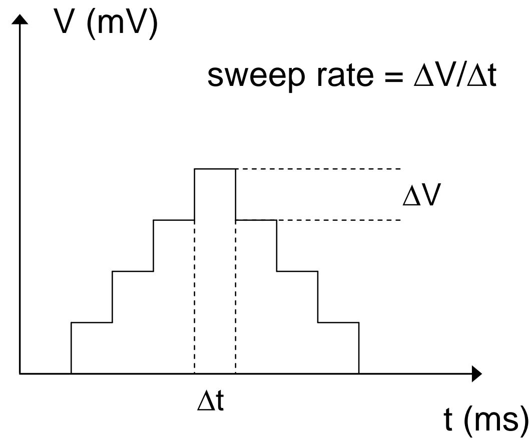

Fig. 2-4. Schematic illustration of voltage sweeping mode in DC characterization.

flowing through the insulating layer will result in permanent dielectric breakdown. Therefore the high SET/RESET current will decrease the endurance of memory devices. The compliance current is applied to the device in order to avoid destructive breakdown. Under negative bias voltages, the migration of Cu^{+} ions in electrolyte is suppressed. The Cu nanobridge cannot form a conductive path between electrodes. The electro-reduction reaction occurs in the TaO_x layer. The O^{2-} ions migrate from the Cu electrode to the Pt electrode in the electric field pointing from Pt to Cu. The vacancies V_O left behind by migrating O^{2-} ions form a conductive filament and the resistive state changes. An evidence for V_O formation is the observation of gas (O_2) bubble formation under the negative bias. Gas bubble formation is never observed under positive bias with compliance current below 1 mA.

In Fig. 2-5(a), the RESET current for V_O CF in the bipolar switching mode is 2 to 3 mA, and the RESET voltage is 1.2 V. The R_{ON} and R_{OFF} are 187 Ω and 663 MΩ, respectively. In the case of unipolar switching the RESET voltage is negative at −1.2 V as shown in Fig. 2-5(b), i.e. the same magnitude as the reset voltage for the bipolar

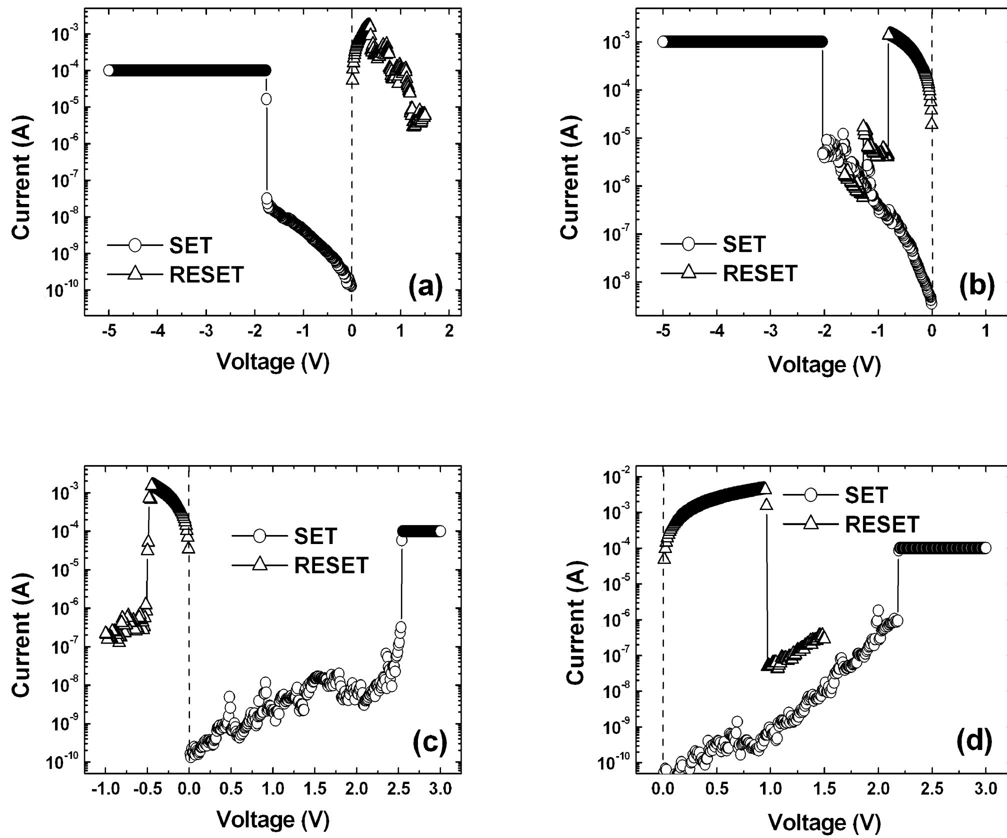

Fig. 2-5. I–V characteristics of bipolar and unipolar switching. (a) Bipolar switching of V_O CF. (b) Unipolar switching of V_O CF. (c) Bipolar switching of Cu CF. (d) Unipolar switching of Cu CF.

switching. The equality of the voltage magnitude entails equality of the current levels validating the assumption that the rupture of the CF is triggered by Joule heating. Figs. 2-5(c) and (d) show the bipolar and unipolar switching of Cu CF, respectively. Under positive bias voltages, Cu conductive filament is formed by Cu^+ ion migration in the high electric field and electrodeposition on the Pt electrode. In both cases, the Cu CF forms above 2 V and the compliance current is 0.1 mA. The R_{ON} and R_{OFF} are 288 Ω and 566 MΩ, respectively. The RESET current and voltage of Cu CF is 2 mA and –0.5 V for bipolar switching, and 6 mA and 1 V for unipolar switching. Joules heating is significant at such high current levels and can rupture both the Cu and V_O filaments.

Since Joules heating is polarity independent, both V_O and Cu CFs can be ruptured at positive and negative RESET voltages. The ON-state resistance R_{ON} does not depend on the device area, indicating the SET process is based on a local conductive path. The OFF-state resistance R_{OFF} decreases with the device area, indicating within statistical variations the leakage current is homogeneous across the cell. It was also observed that the V_O CF has less noisy HRS than the Cu CF.

Another mechanism responsible for rupturing the Cu CF is the anodic oxidation $Cu \rightarrow Cu^{z+} + ze^{-}$ during RESET process. When the applied voltage reaches a threshold (between −1 to −2 V at a sweep rate of −0.2 V/s), the Cu atoms in the CF dissolve into TaO_x electrochemically. This RESET mechanism is suitable for explaining the bipolar switching of CBRAM because the Cu atoms in the anode do not dissolve with a negative bias voltage. However, the unipolar switching of Cu-based CBRAM has been demonstrated in Fig. 2-5(d). In the unipolar RESET process, the anodic reactions take place on both Cu anode and CF [13]. The constructive cation flux from the anode can be possibly higher than the destructive flux from the CF connective neck. This means the magnitude of RESET voltage may depend on the voltage polarity. On the contrary, the cumulative probability has shown that the positive and negative V_{SET} have symmetric distributions [14]. The RESET process is actually voltage polarity independent. In addition, RESET currents of mA range are usually measured at above 1 V for $Cu/TaO_x/Pt$ devices. The temperature elevation cannot be neglected for such high RESET power consumption. Therefore two mechanisms are considered to explain the CF rupture: the electrochemical

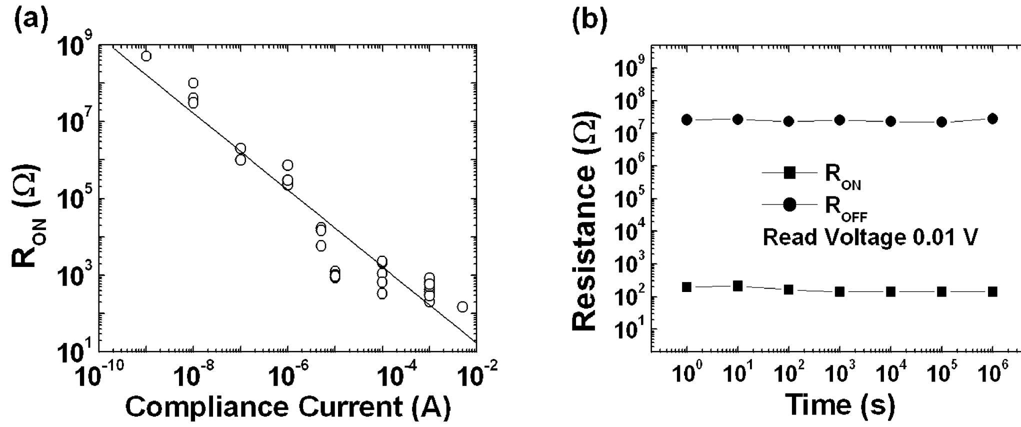

Fig. 2-6. (a) Dependence of R_{ON} of individual resistive switches as a function of the compliance current applied to the cells during the set operation. (b) Retention of Cu CF at room temperature. The Cu CF was formed with compliance current of 1 mA.

dissolution and Joule heating. Due to the ohmic behavior of a metallic CF, these two effects cannot be separately investigated in the RESET process.

Once the metallic nanofilament connects the two electrodes, it will grow laterally to increase the diameter and reduce the resistance. The subsequent growth process is controlled by the bias compliance current (CC). The dependence of R_{ON} on the compliance current is shown in Fig. 2-6(a). Since R_{ON} depends on I_{CC}, multi-bit storage in a single device can be implemented by controlling the cell LRS by different programming current. The multilevel switching based on R_{ON} change has been demonstrated on various types of resistive memory devices [15], [16]. The property is even promising for the synapse in neuromorphic computation. The retention of Cu CF at room temperature is shown in Fig. 2-6(b). The resistance fluctuation is very small.

The switching based on Cu and V_O CFs can be kept apart by the polarity and magnitude of bias voltages. In our Cu/TaO_x/Pt devices, the magnitude of RESET voltage of Cu CF is significantly lower than the SET voltage of V_O CF. Fig. 2-7

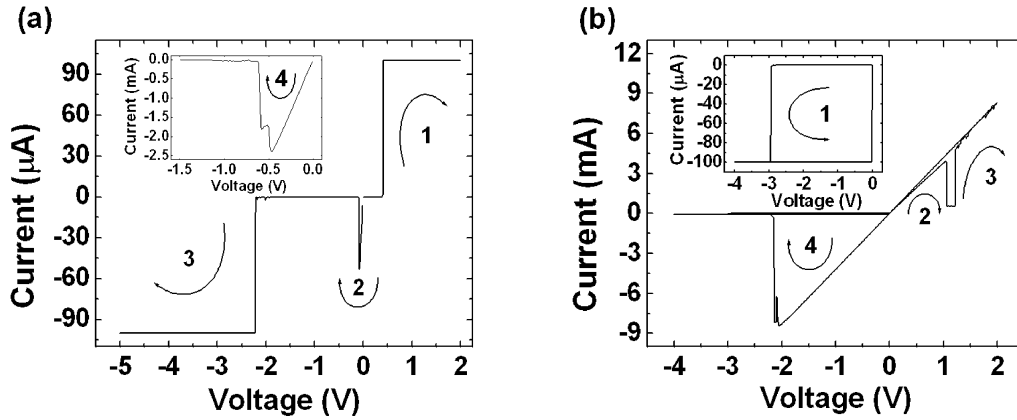

Fig. 2-7. (a) Consecutive bipolar switching of Cu CF and unipolar switching of V_O CF. Section 1 and 2 are the set and reset operations of Cu CF. Section 3 and 4 are the set and reset operations of V_O CF. (b) Consecutive bipolar switching of Cu and V_O CFs. Section 1 and 2 are the set and reset operations of V_O CF. Section 3 and 4 are the set and reset operations of Cu CF.

shows the I–V characteristics of consecutive switching of Cu CF and V_O CF in the same Cu/TaO_x/Pt device. In Fig. 2-7(a), the Cu CF is formed (section 1) and ruptured (section 2) by ramping voltage along the positive and negative axes, respectively. The R_{ON} and R_{OFF} for Cu CF are 1305 Ω and 300 MΩ, respectively. After setting the compliance current to 100 μA, the voltage sweep continues from −1 V to −3 V and the V_O CF forms at −2.2 V (section 3). A current of 2.5 mA ruptures the V_O CF at −0.6 V (section 4). The R_{ON} and R_{OFF} for V_O CF are 170 Ω and 4 MΩ, respectively. In Fig 2-7(b), the voltage ramps first along the negative axis and then the positive axis. The V_O CF is formed at −3 V (section 1, see inset) and ruptured at 1.1 V (section 2). At 1.3 V the device transitions from HRS to LRS for the second time (section 3), indicating the formation of Cu CF. Thus for positive voltages the conduction is provided by both filaments but in separate voltage intervals: from 0 V to 1.1 V the conductive nanofilament is the V_O bridge whereas from 1.3 V to above 2 V the

conductive nanofilament is the Cu bridge. The gap in the ohmic behavior between 1.1V and 1.4 V results it a “truncated” Ohm’s relation. Because both bridges have different R_{ON} resistances the slope of the curve in respective intervals is slightly different, as can be seen in Fig. 2-7(b). The created Cu CF can be very thick (i.e. low R_{ON}) since there is no compliance current limitation. Between 1.1 V and 1.3 V neither of the conductive bridges exists and the device is in an OFF state. A reset current of 8 mA is required at −2.2 V to rupture the Cu filament (section 4).

The repeated unipolar switching characteristics of the V_O nanofilament are shown in Fig. 2-8(a) for V_O CF in a single Cu/TaO_x/Pt device. The bias voltage ramps along the negative axis for set and reset operations. The range of the set voltage is −3 V to −7 V, as shown in the inset of Fig. 2-8(a), whereas the reset voltages are less than −3 V (i.e. at the same polarity). The transition between HRS and LRS is more or less abrupt. Significantly higher forming voltages, V_{FORM}, between −7 V and −8 V, are

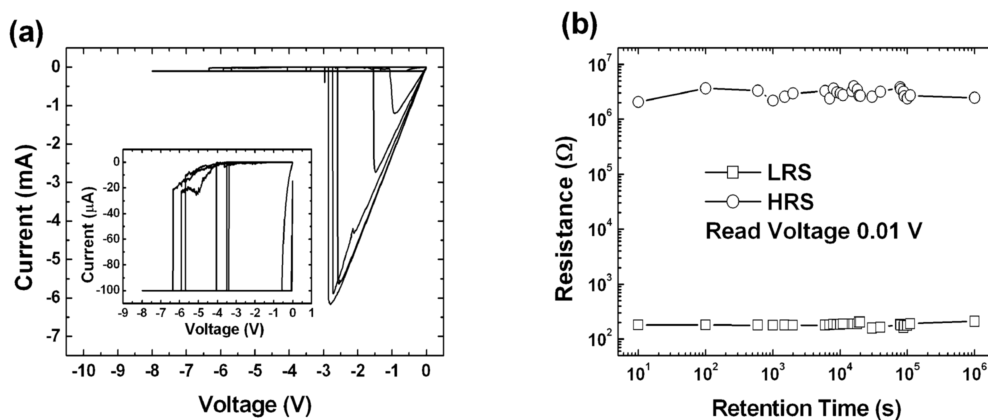

Fig. 2-8. (a) Repeated unipolar switching characteristics for V_O CF in a Cu/TaO_x/Pt device. (b) Retension property of the V_O CF at 25 °C. The ON/OFF resistance ratio is 10^4. The LRS and HRS stays nearly constant up to 10^6 seconds.

necessary for the V_O CF formation in fresh devices. The retention property of the two states has been characterized at room temperature. The read voltage of 0.01 V is used to measure R_{ON} and R_{OFF}. Fig. 2-8(b) shows very uniform LRS and HRS distribution of a single Cu/TaO_x/Pt device for V_O CF with the retention time up to 10^6 s. The LRS is about 190 Ω and HRS is about 2.5 MΩ respectively, i.e. an OFF/ON ratio above 10^4. R_{OFF} is measured right after the rupture of the respective CF.

The resistances are measured from 0 °C to 20 °C for low R_{ON} values of two kinds of filaments, as shown in Fig. 2-9. The temperature coefficient α is 0.0033 K^{-1} for Cu CF, where as 0.0013 K^{-1} for V_O CF. The measurement results are quite close to the reported data from NiO-based ReRAM devices and Cu CF based CBRAM [17], [18]. As the coefficient measured for the Cu nanofilament is very close to the bulk value of Cu, it serves as an identifier of Cu as the basic building block of the nanofilament. The positive temperature coefficient of V_O CF implies that the filament is metallic instead of semiconducting for the low R_{ON} value. The difference between the two

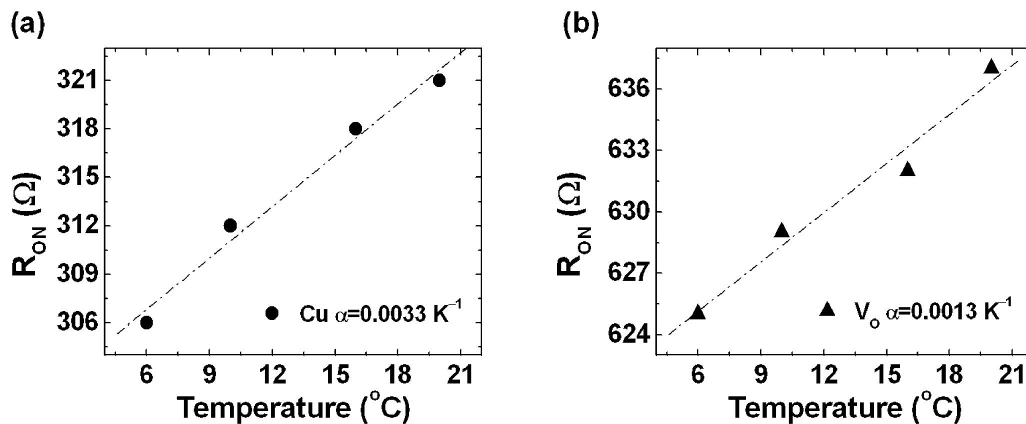

Fig. 2-9. R_{ON} temperature coefficient α of (a) Cu CF and (b) V_O CF.

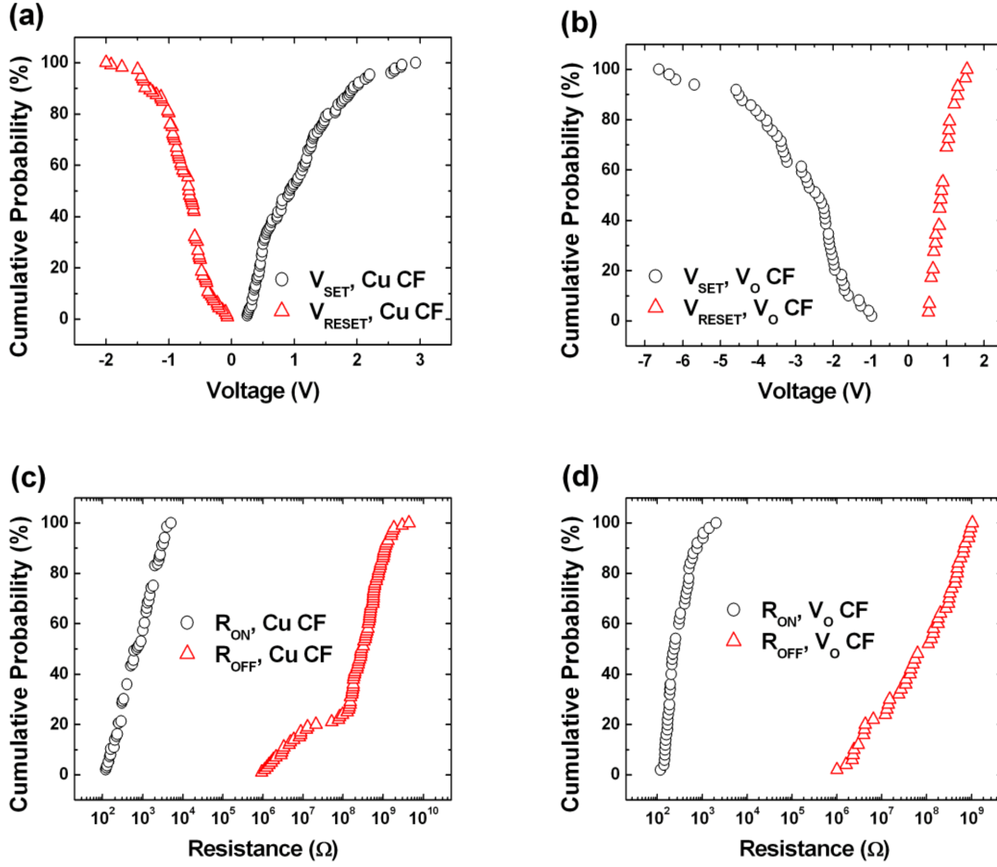

Fig. 2-10. (a) V_{SET} and V_{RESET} distributions of Cu/TaO_x/Pt devices. The SET voltage is positive for Cu CFs. (b) V_{SET} and V_{RESET} distributions of Cu/TaO_x/Pt devices. The SET voltage is negative for V_O CFs. (c) R_{ON} and R_{OFF} distributions of Cu CFs in Cu/TaO_x/Pt devices. The read voltage is 0.1 V for R_{OFF}. (d) R_{ON} and R_{OFF} distributions of V_O CFs. The device sizes are 10 μm, 15 μm, 20 μm, 25 μm, 30 μm, and 35 μm.

coefficients underscores that two different conduction mechanisms are at work.

The bipolar switching cycles have been repeated on Cu/TaO_x/Pt devices. Figs 2-10(a) and 2-10 (b) show the statistical V_{SET} and V_{RESET} distributions of a single Cu/TaO_x/Pt device with Cu and V_O CFs. In Fig. 2-10(b), the range of V_{SET} is from −1 V to −7 V, which is much wider than V_{RESET}. This wide range could be attributed to the non-uniform oxygen vacancy structures in the TaO_x layer of different devices. The positive and negative V_{RESET} ranges are mainly ±(0.6 V, 1.5 V). Figs. 2-10(c) and

2-10(d) show the statistical R_{ON} and R_{OFF} distributions of Cu/TaO_x/Pt devices with Cu and V_O CFs. The R_{OFF}/R_{ON} ratios are above 10^4.

The ranges of RESET voltages for Cu CFs and V_O CFs are comparable (0 V to ±1.5 V). However, the ranges for the SET voltages can be very different. For Cu CF, V_{SET} ranges from 0 V to 3 V. The major proportion is between 1 V and 2 V. For V_O CF, most V_{SET} are above –2 V and some are as high as –6 V. This may indicate that O^{2-} has a higher potential barrier than Cu^+ for the redox reaction on the electrodes. The work function difference of anode and cathode contributes to the asymmetric distribution of SET voltages [19]. Pt has a higher work function (5.35 eV) than Cu (4.35 eV), resulting in a built-in voltage of about 1 V across the dielectric. When the negative voltage is applied to Cu electrode, this voltage difference has to be overcome before an effective voltage drops on the oxide layer. Thus the built-in voltage shifts the effective voltages asymmetrically for Cu and V_O CFs formation. The main difference in the SET voltages is, however, due to the difference of mobilities of Cu^+ and O^{2-}, requiring higher fields for O^{2-} than for Cu^+ migration. Therefore, the SET voltage for Cu CF is significant lower than that of V_O CF.

Fig. 2-11(a) shows the statistical V_{SET} and V_{RESET} distributions for the V_O CF conduction. The V_{RESET} distributions show narrow and symmetrical shape, indicating the RESET mechanism is voltage polarity independent requiring the same magnitude of reset current. This shows that the rupturing of the V_O filament is mainly thermally driven by the local Joule heating. Fig. 2-11(b) shows the SET voltages of Cu and V_O CFs. The ranges of reset voltages are quite close (0 to ±2 V) for the Cu CFs and V_O

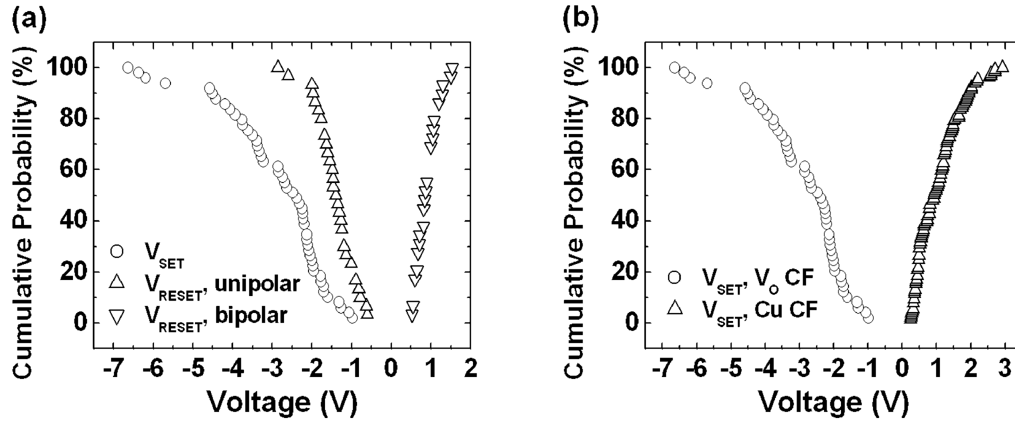

Fig. 2-11. (a) V_{SET} and V_{RESET} distributions of Cu/TaO_x/Pt devices with V_O CFs. Both positive and negative reset voltages can be used to rupture the conductive filaments. (b) Comparison of set voltages of Cu and V_O CFs. The V_O CF needs higher V_{SET} than the Cu CF.

CFs of Cu/TaO_x/Pt devices. In general, R_{OFF} of resistive switches displays a wide range up to three orders of magnitude. The large variation of V_{SET} and R_{OFF} poses a serious challenge for this kind of memory device. The wide distribution of V_{SET} and R_{OFF} may be narrowed down by engineering the electrode/electrolyte interface with appropriate intermediate layers, improved layer uniformity, and purity of the deposited materials.

2.4 Bubble Formation

During the forming and switching operations at positive voltages, no visible mechanical degradation is observed on the 10 μm cells, as shown in Fig. 2-12(a). Interestingly, when the negative voltage sweep is applied to 35 μm cells, dome-like protrusions are observed in the device area, as shown in Fig. 2-12(b). Under this bias polarity, Cu^+ ions are repelled by the electric field in TaO_x and O^{2-} ions are moved to

the Pt electrode [20]. The following electro-oxidation has been postulated at the Pt electrode,

$$2O^{2-} \rightarrow O_2 + 4e^- \quad (2\text{-}2)$$

Since the TaO_x layer was deposited in a blanket fashion, it is hypothesized that O_2 gas is being generated under the TaO_x film and eventually lifts portions of the top layers. The protrusions are observed in 35 μm to 15 μm cells but not in 10 μm and smaller cells. This may be explained by the fact that in smaller cell sizes the O_2 gas may escape through some leak at the boundary of the device area or that the gas pressure is not high enough to produce protrusions.

The experiment indicates that the formation of oxygen vacancy, which is the low resistivity building material of CF, must be necessarily accompanied by O_2(gas) generation according to the reaction [21]

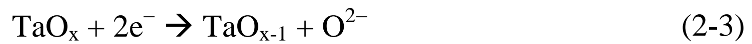

$$TaO_x + 2e^- \rightarrow TaO_{x-1} + O^{2-} \quad (2\text{-}3)$$

or

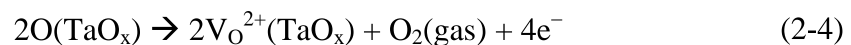

$$2O(TaO_x) \rightarrow 2V_O^{2+}(TaO_x) + O_2(gas) + 4e^- \quad (2\text{-}4)$$

The (TaO_x) in Eq. (2-4) indicates that the species is part of the TaO_x material matrix. Because the above reaction requires participation of an electron, the reaction must take place at the Pt/TaO_x interface. The gas bubble is thus formed between the bottom Pt electrode and the solid electrolyte. An opposite polarity bias as high as 4 V has been applied to cells displaying the protrusions without causing any disappearance of the protrusions. Thus the forming process of the protrusions appears to be electrically irreversible. This is in contrast with findings in Ref. [20] where opposite voltage

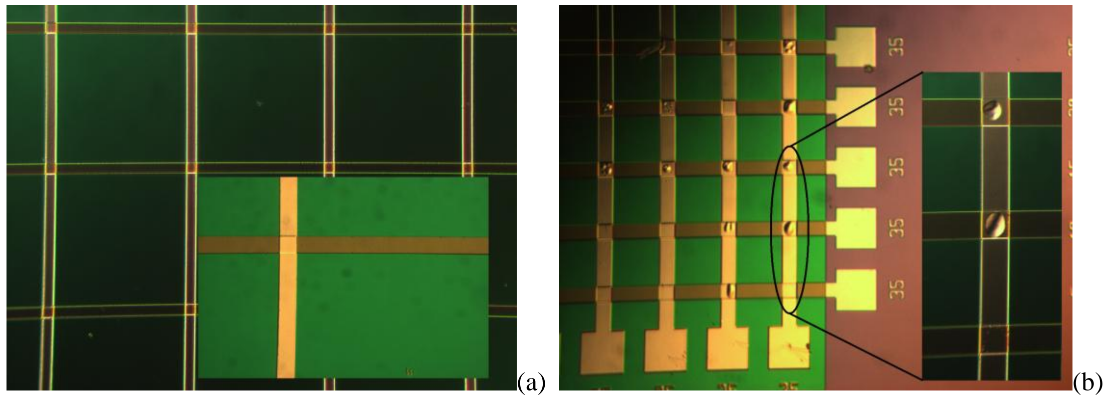

Fig. 2-12. (a) Image of 10 μm × 10 μm cells after multiple switching (0 to −7 V). No protrusions are observed. The inset shows the enlarged view of one device. (b) Image of 35 μm × 35 μm cells after forming voltage sweep from 0 to −7 V. The inset shows the enlarged view of protrusions.

polarity caused the protrusions to shrink and disappear. In Ref. [20] it was also postulated that the protrusions are due to oxygen gas bubble formation at the Pt-electrolyte interface. However, the electrolyte in devices of Ref. [20] is TiO_2 whereas in our case it is oxygen deficient TaO_x. In Ref. [20] it was also reported that some of the bubbles keep growing with applied voltage stress and that larger bubbles engulf their neighbors. Such behavior has not been observed in our samples as we see only one protrusion per cell.

The bubble formation and resistive switching can be unified in a stochastic percolation model. The percolation process is conceptually illustrated in Fig. 2-13. The oxygen vacancies are generated by the electric field randomly in the TaO_x layer. Oxygen anions are attracted to Pt electrode and oxidized to form O_2 which causes the bulge in the device cell. The left vacancies accumulate and form a conductive path.

In the experiment, the gas bubble of large size is likely to damage the Pt-TaO_x interface irreversibly and even the oxide thin film itself, rendering the reincorporation

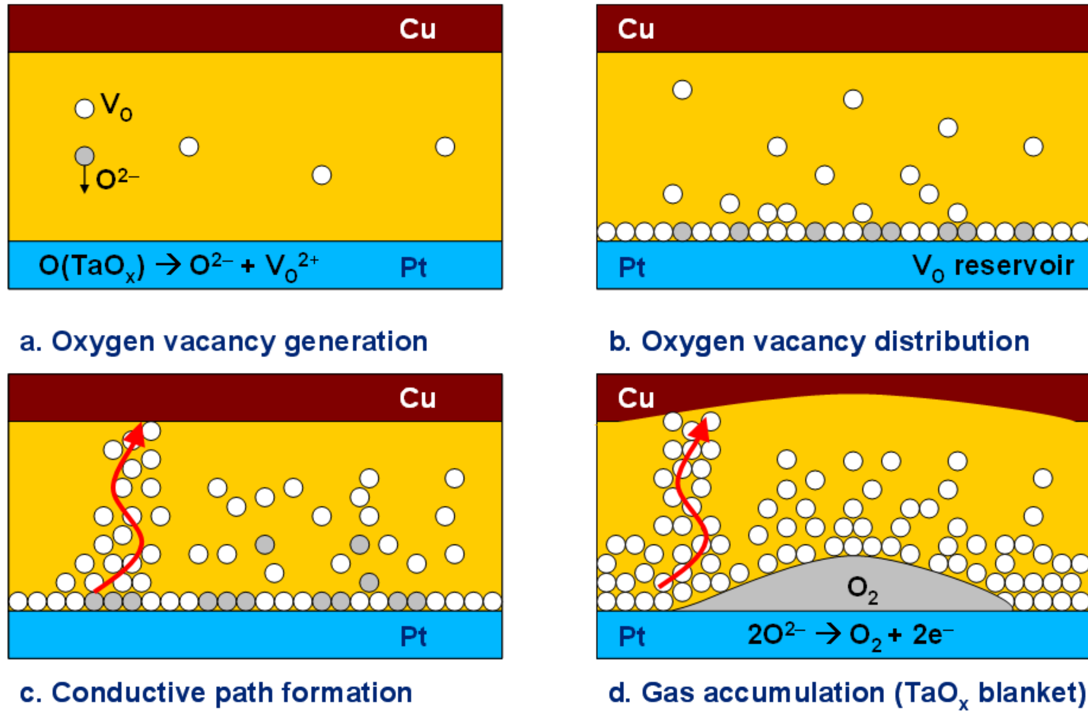

Fig. 2-13. Percolation model for the bubble formation and resistive switching based on oxygen vacancy filament. (a) Oxygen vacancy generation. (b) Oxygen vacancy distribution. (c) Conductive path formation. (d) Gas accumulation (TaO_x blanket).

of O_2 gas into the oxide very difficult. In case of our samples protrusions of some cells disappeared without any voltage stress after a few hours. The most likely explanation of this disappearance is that over time the pressure in the gas bubble must have created a leakage path for the gas to escape, for example, when the bubble reached the perimeter of the cell.

At positive bias, the O^{2-} and Cu^+ ions are believed to migrate at the same time. However, Cu filaments have lower potential barriers and can form before a substantial volume of oxygen gas manages to accumulate at the Pt electrode, if it is formed at all. Subsequently, when the Cu filament has formed, it acts like a short circuit for ion drift current. Very low voltage between two electrodes stops the O^{2-} migration. Therefore,

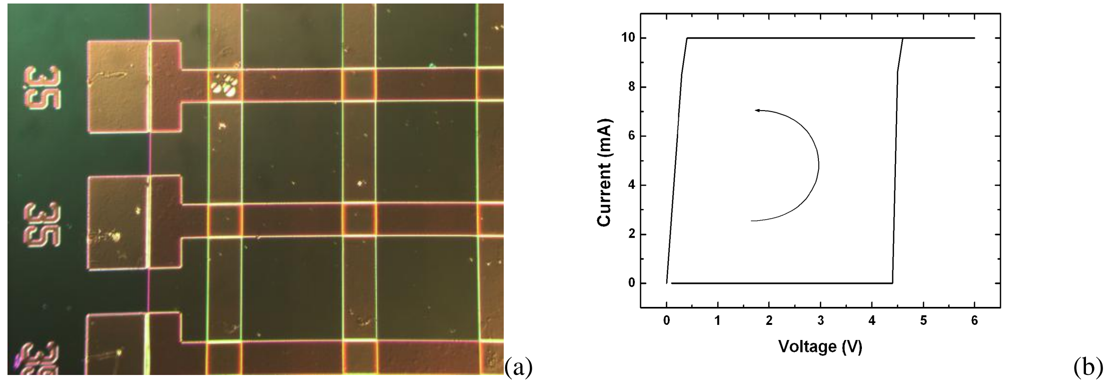

Fig. 2-14. (a) Image of 35 μm × 35 μm cells after electroforming (0 to ±7 V). The protrusions appear in one of the nine devices under test (upper left). (b) Attendant I–V characteristic of the electroforming operation for the $Cu/TaO_x/Cu$ device with protrusions in (a).

the gas bubbles do not appear when forming or setting the Cu nanofilaments with positive bias voltages. In the absence of external electric field, charge neutrality must be maintained in the oxide. Therefore negatively charged oxygen vacancies must be created to preserve the electroneutrality the dissolved Cu^+ cations.

To further explore the contributions of O^{2-} and Cu^+ migration during switching, we have fabricated $Cu/TaO_x/Cu$ devices in crossbar arrays and tested the electroforming process. Nine fresh device cells are switched on with bias voltage of both polarities (0 V to ±7 V). In these $Cu/TaO_x/Cu$ devices, both Cu^+ and O^{2-} ions can migrate in opposite directions under either voltage polarity. Visible protrusions only appear in one of the nine $Cu/TaO_x/Cu$ devices under test as shown in Fig. 2-14(a). These protrusions are formed with the attendant I–V characteristic shown in Fig. 2-14(b), in which the forming voltage is about 4.4 V. However, this resistive switching in $Cu/TaO_x/Cu$ devices does not show high endurance and reliability. Since positive voltage is applied to the top electrode (TE) and the bottom electrode (BE) is

grounded, O^{2-} ions should be attracted to the TE-oxide interface and O_2 bubbles form there.

No bubble formation has been observed at the negative bias. At the negative bias the bubble would have been formed at the bottom electrode. From pure mechanical point of view it suggests itself that it is easier to form protrusions visible at the top of the cell when the O_2 generation takes place at the top electrode rather than at the bottom electrode. Thus it can be assumed, since the Cu/TaO_x/Cu is a symmetric device, that O_2 is produced at the bottom electrode as well, however, without being able to lift the superjacent electrolyte and top electrode layer to produce the optical manifestation of a protrusion. In contrast to the 35 μm Cu/TaO_x/Pt devices, multiple small protrusions (see Fig. 2-4(a)) are formed instead of a single large one and therefore presumably less O_2 gas is generated in the redox reaction in the Cu/TaO_x/Cu samples. The protrusions remain after the removal of bias voltage.

Since there are no visible bubbles in most of Cu/TaO_x/Cu devices, we conclude the Cu nanofilament is more likely to form before the oxygen vacancy nanofilament and will therefore suppress O^{2-} migration thereafter. Even if O_2 can be generated in the Cu/TaO_x/Cu devices, its volume is smaller than in the case of Cu/TaO_x/Pt devices under negative bias voltage.

2.5 RESET-SET Instability

Fig. 2-15 shows a switching cycle of Cu/TaO_x/Pt device with reset voltage sweep from 0 V to −4 V. Section (1) shows the formation of Cu CF and the device resistance transitions from HRS to LRS. With -0.6 V reset voltage the Cu CF ruptures and HRS

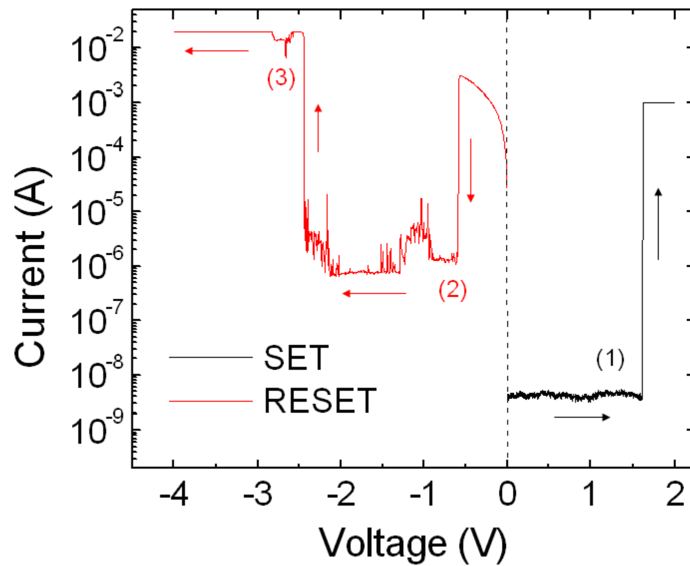

Fig. 2-15. RESET-SET instability of Cu/TaO_x/Pt resistive memory devices. The I–V characteristics are divided into three sections: (1) Cu CF formation (2) Cu CF rupture (3) V_O CF formation.

restores in section (2). The reset voltage sweep extends to −4 V and at −2.5 V the device resistance state changes for the second time. The desired HRS switches to the undesired LRS. This phenomenon is named RESET-SET instability of bipolar resistive switching memory.

When a negative voltage bias is applied to the resistive device, Cu ion migration is suppressed. According to aforementioned switching mechanism, the second resistance state transition is caused by the V_O CF when the SET voltage of V_O CF is very close to the RESET voltage of Cu CF. Due to the fluctuation of SET and RESET voltages, the operating window between sections (2) and (3) is difficult to accurately predict. However, for memory applications, this instability must be overcome to protect the data stored in each cell.

One of the solutions to the reset-set instability can be the incremental reset voltage which is similar to the programming strategy for NAND flash memory [22]. In this method, the RESET voltage increases by small steps. Multiple reset voltage pulses or sweeps (V_0, V_1, V_2, V_3,…) will be used to reset the memory device, as shown in Fig. 2-16. The initial reset voltage will be lower than the target reset voltage and the lower limit of the SET voltage fluctuation of V_O CF. Enough voltage margin can assure that the instability will not be triggered by any mistake. V_0, V_1, V_2, V_3,… will be used to reset the device one after another until the resistance state changes. The difference between adjacent RESET voltages (V_0 and V_1, V_1 and V_2, V_2 and V_3,…) is the

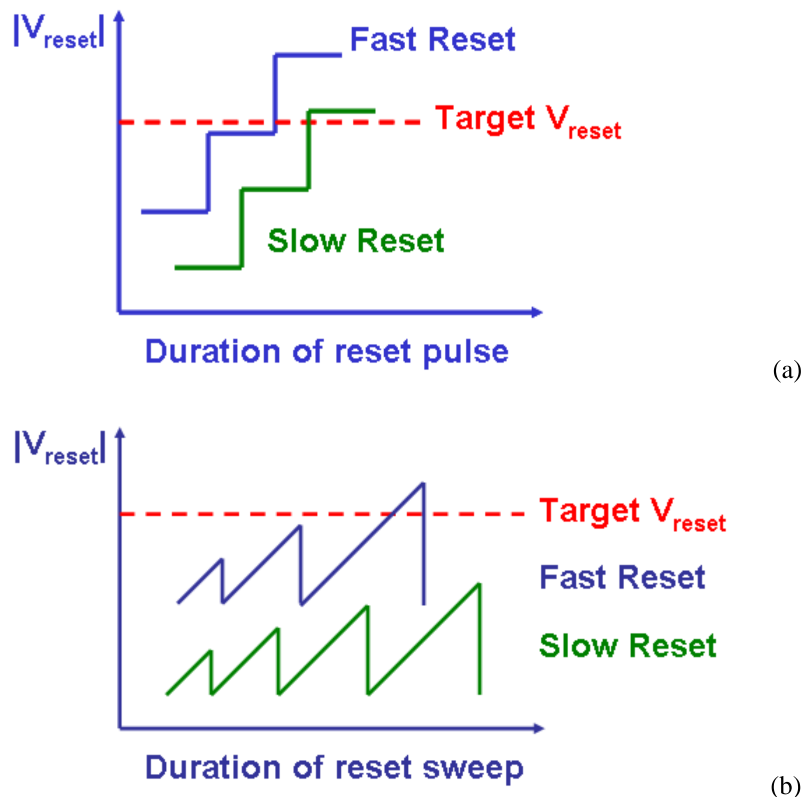

Fig. 2-16. Schematic illustration of the incremental RESET strategies in (a) voltage pulse mode and (b) voltage sweep mode.

voltage step ΔV. The RESET process can be fast or slow depending on the voltage step ΔV. If ΔV is large, the RESET voltage will quickly approach the target voltage. However, as shown in Fig. 2-16(a) the final reset voltage will be much larger than the target V_{RESET} in the fast reset operation. Small ΔV can effectively control the difference between the target voltage and the RESET voltage. However, it will require more trial time to ramp up the reset voltage. The selection of proper ΔV depends on the stochastic property of V_{SET} of V_O CF and V_{RESET} of Cu CF. The wider the gap between distributions of $V_{SET}(V_O)$ and $V_{RESET}(Cu)$, the larger the ΔV, and thus the faster the programming. In the quasi-static DC measurement, the voltage sweeps in Fig. 2-16(b) are used as the reset strategy.

2.6 Multilevel SET Process

In the voltage sweeping mode with current compliance, the number of metallic conductive filament is assumed to be only one. This is because the voltage drop across the electrolyte layer is small after the first filament connects the two electrodes. The cation migration, nucleation, and redox reaction are all suppressed by this small voltage bias. Simulations have been carried out to explain this phenomenon [23]. Based on this hypothesis, more than one filament should be able to form by continuously applying high enough voltage on the device cell. The case of two filament conduction has been demonstrated for Cu based resistive switches [24]. The characteristic I–V behavior is the two level current jumps in the voltage sweeping mode. Multiple filaments formation has also been reported for other high-k dielectric materials such as ZrO_2 and HfO_2 [25], [26].

Three levels of current jump have been observed by using high current and voltage ranges in the I–V characteristic measurement as shown in Fig. 2-17. The current compliance is removed and the voltage sweep range is 0 to 10 V. The sweep rate is 0.2 V/s and the area of device under test is 10 μm by 10 μm. The SET voltages for each level are V_{SET1} = 3.64 V, V_{SET2} = 6.78 V, and V_{SET3} = 8 V. The total resistances for each level are read from the slopes of I–V curves. They are $R_1 = 401$ Ω for level 1, $R_2 = 256$ Ω for level 2, and $R_3 = 191$ Ω for level 3. Assuming the three parallel filaments are formed sequentially in Fig. 2-17, the resistance of each filament is extracted as $R_{CF1} = 401$ Ω, $R_{CF2} = 708$ Ω, and $R_{CF3} = 752$ Ω, where $R_1 = R_{CF1}$, $R_2 = R_{CF1} // R_{CF2}$, and $R_3 = R_{CF1} // R_{CF2} // R_{CF3}$. The device cannot be reset after the SET process because a very high current flows through the device and causes permanent damage to the structure.

Although the multilevel resistance change is experimentally demonstrated, the

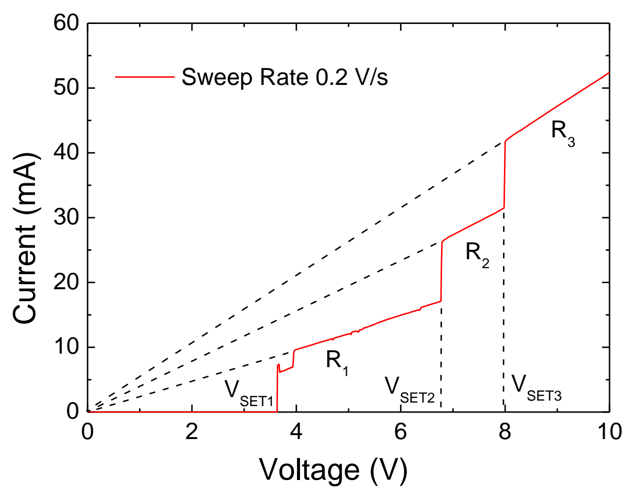

Fig. 2-17. Multilevel current jump in voltage sweeping mode.

proper explanation of the switching time and SET voltage for each current jump is still missing. Without current compliance, all the nucleation sites have more or less the equal probability to form a filament. However, the second and third current jumps require much higher V_{SET} and t_{SET}, which is open to future study.

2.7 Summary

The Cu/TaO_x/Pt devices have been fabricated by electron beam evaporation and lift-off technologies. The devices are characterized in quasi-static DC bias mode. Two switching mechanisms are observed and separated by temperature coefficient of resistance, SET voltages, and bubble formation. The ON-state resistance does not depend on the device area, indicating the filamentary type conducting path built in the dielectric. One switching mechanism is the formation and rupture of Cu nanofilament whereas the other oxygen vacancy nanofilament. Both unipolar and bipolar switching modes are observed for each type of nanofilament. Bulges have been observed on large area device cells during the formation of V_O nanofilament. This phenomenon is attributed to the reaction at the Pt-TaO_x interface generating O_2 gas. The damage of bulges is irreversible. The gas may leak out from the perimeter of small cells. No visible bulges appear during the formation of Cu nanofilament indicating higher reliability of Cu CF based resistive switching.

Chapter 3 Volatile Switching of Cu/TaO_x/δ-Cu/Pt Devices

This chapter describes volatile/threshold switching devices fabricated with the same process as resistive memory devices. A thin Cu layer is inserted between the inert Pt electrode and the TaO_x electrolyte as a sinking layer. The Cu atoms from nanobridge diffuses into the δ-Cu sinking layer and therefore the resistance state switches from low to high. The characterization with constant voltage bias show that the switching mechanism is due to the electrochemical reaction. The volatile switching devices can be applied to the nanocrossbar memory architecture to isolate the sneak path and diode logic circuits.

3.1 Introduction

The crossbar architecture as shown in Fig. 3-1 is the major interconnection structure for emerging nonvolatile memory devices. One memory cell locates at each cross point of interconnects. The cells can be accessed by selecting the "word line" and "bit line" in the same manner as NOR flash memory. This type of interconnection can increase the device endurance, decrease the read time, and increase the reliability of memory. Therefore NOR is used for code storage and critical data. The target area of the two-terminal memory cells is $4F^2$ (F is the minimal length defined by lithography) [1].

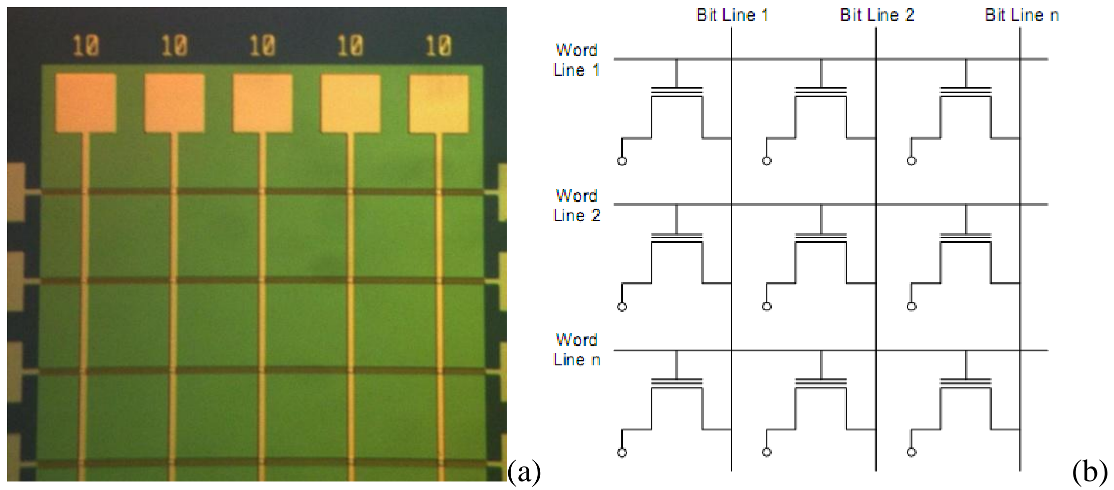

Fig. 3-1. (a) Crossbar architecture for emerging nonvolatile memory devices. (b) NOR type flash memory.

Unlike NOR flash memory, the "word line" and "bit line" of two-terminal CBRAM are not isolated. Once the resistive switch is in LRS (data written into the cell), the two interconnection lines are connected. If more than one memory cells are in LRS as shown in Fig. 3-2, there is a sneak path which will bypass the reading or programming of some memory cells [2]. The red cell in Fig. 3-2 is the target device

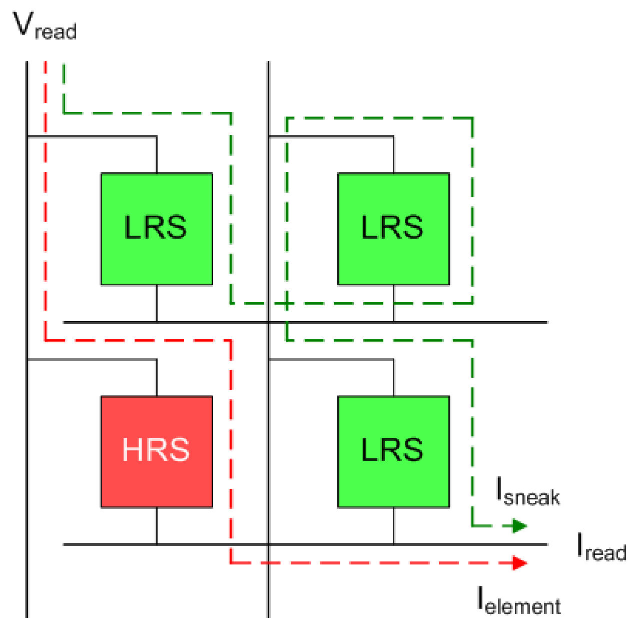

Fig. 3-2. Sneak current in nanocrossbar architecture [2].

and a sense voltage is applied to both terminals of the red cell to read its memory state. However, the surrounding green cells are all in LRS, a sneak current I_{sneak} can pass through several green cells and finally merge with the target sense current $I_{element}$ to form read current I_{read}. I_{read} is not at the standard current level and thus will disturb the data reading. Simple cross-point architecture without selection devices cannot be applied directly for memory manufacturing.

One intuitive solution to the sneak path issue is to serially connect two devices as shown in Fig. 3-3. One of them is the memory device which stores the data, whereas the other is the selection device which isolates the sneak current. The selection device must be able to regulate the current flow in one direction. A diode or a transistor can be connected in series with the CBRAM device [3], [4]. If a diode is used as the selection device, there will be two diodes back to back in the sneak path and sneak current will be suppressed. If a transistor is used as the selection device, not only the sneak path is isolated, the current flowing through memory device can also be controlled individually. Therefore the multi-bit storage in different cells is possible.

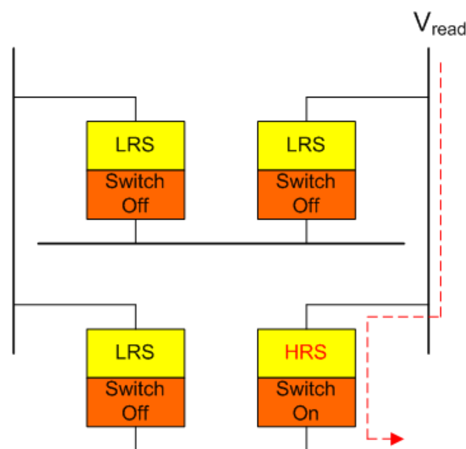

Fig. 3-3. Switching element structure proposed by Samsung [5].

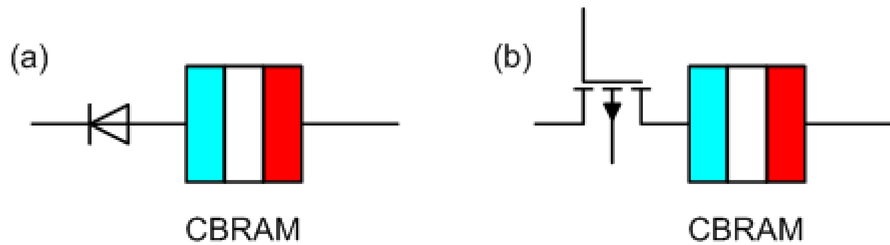

Fig. 3-4. (a) 1D1R and (b) 1T1R device cells in nanocrossbar architecture.

Advanced selection devices are also being exploited to solve the sneak path problem. Samsung has demonstrated the serial connection of memory and threshold switching resistive devices in the crossbar memory architecture [5]. The device cell consists of one Pt/NiO/Pt memory element for storing the data, and one Pt/VO_2/Pt switch element for isolating the memory element from others, as shown in Fig.3-4. Pt/NiO/Pt device is one of the resistive memory switches (RRAM), which exhibit nonvolatile switching behavior. A phenomenon of threshold/volatile switching has been observed for Pt/VO_2/Pt resistive switches. In the threshold/volatile switching, the current exists together with the bias voltage. Once the write signal is removed, the resistance state of the memory element is changed, whereas the resistance switch element is high.

In this chapter, we present the threshold/volatile switching phenomenon observed in the Cu/TaO_x/δ-Cu/Pt devices. A thin Cu layer is inserted between TaO_x and Pt as a sink layer to rupture the Cu bridge at small current level. The volatile switching can be utilized for the selection device in nanocrossbar memories as well as diode logic circuits.

3.2 Threshold Switching of Resistive Memory

Samsung invented the Pt/VO_2/Pt device as the switch element in the nanocrossbar architecture. The oxygen deficient VO_2 results in threshold switching. When the voltage sweeps from 0 V to V_{th}, the resistance of device changes abruptly at V_{th} from high to low. After turning on the device, the voltage sweeps back from V_{th} to 0 V and the current is holded. Before the voltage reaches 0 V, the device resistance returns from low to high. In this case, the resistive switching only appears between two threshold voltages as shown in Fig. 3-5. The threshold switching does not reserve the low resistance state after the bias voltage returns to zero, i.e. the device is in high resistance state without bias.

The threshold switching phenomenon has also been observed on Pt/NiO/Pt, Cu/ZnO:Mn/Pt, and polyimide-based resistive switches [6]−[10]. Besides selection devices, transistors are under development based on the nonvolatile/volatile resistive

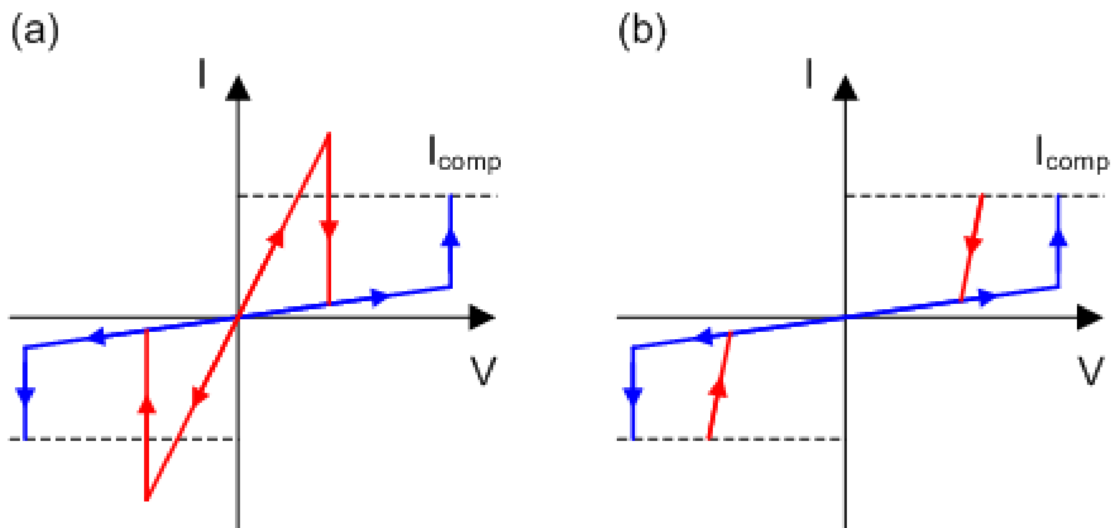

Fig. 3-5. Schematic diagram of I–V characteristics of (a) memory switching and (b) threshold switching devices [7].

switching [11]. A thermal model has been developed to explain the I–V characteristics of oxide-based devices [6], [7]. The Pt/NiO/Pt devices show memory switching at low temperature, whereas they show threshold switching at room temperature. Therefore the threshold switching is caused by the temperature driven filament rupture. At room temperature, significant Joule heating increases the local temperature of the oxygen vacancy conductive filament rendering it unstable and dissolved.

3.3 Characterization of Cu/TaO$_x$/δ-Cu/Pt Devices

With the insertion of a Cu δ-layer between the solid electrolyte and the inert Pt electrode, a volatile switching of conductive bridge resistive devices has been observed, for the first time, in Cu/TaO$_x$/δ-Cu/Pt devices. The conductive Cu filament (CF) is formed the same way as in the conventional nonvolatile devices. However, when applied voltage becomes zero, CF ruptures spontaneously. The new effect of CF volatility is explained by the dynamic balance between Cu^+ field-supported hopping and the Cu self-diffusion. Hence, the low resistance state, characterized by existence of the conductive filament, is only dynamically stable as long as high enough voltage is applied to the device.

The schematic of device cross-section is shown in Fig. 3-6(a). The difference to the conventional resistive switch is the insertion of a thin Cu layer (δ-layer) interposed between the solid electrolyte and the inert Pt electrode. We have fabricated Cu/TaO$_x$/δ-Cu/Pt switches at room temperature with 32 nm thick oxygen-deficient TaO$_x$ formed by e-beam evaporation. The bottom Pt electrode has been deposited by

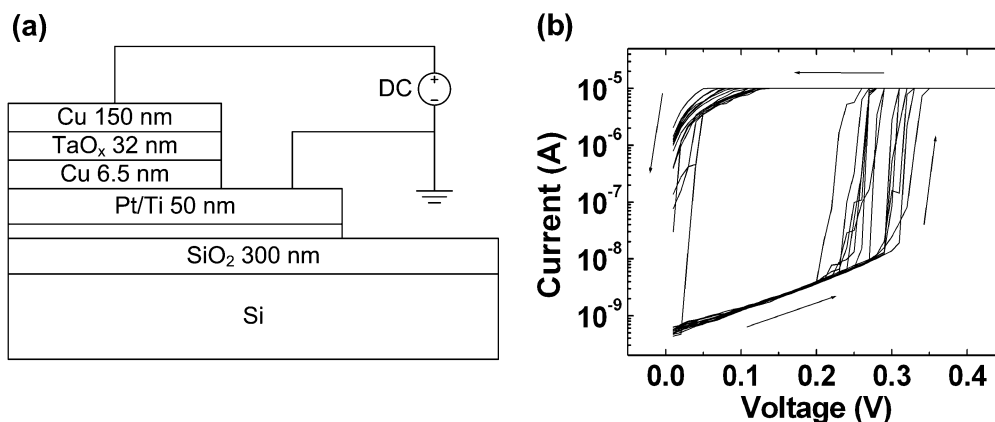

Fig. 3-6. (a) Cross-sectional view of Cu/TaO_x/δ-Cu/Pt volatile resistive switching cells. (b) Fifteen consecutive volatile switching curves of a Cu/TaO_x/δ-Cu/Pt device in log scale.

evaporation and patterned by lift-off on a thermally oxidized Si wafer. The top Cu electrode lines were processed in the same way but patterned perpendicularly to the bottom Pt lines. The width of the metal lines varies between 1 μm and 35 μm. With the exception of the Cu δ-layer, the manufacturing process is the same as Cu/TaO_x/Pt devices. The thickness of the Cu δ-layer between TaO_x and Pt bulk electrode is 6.5 nm.

The schematic of device cross-section and process flow are shown in Fig. 3-6(a). The difference to the conventional resistive switch is the insertion of a Cu δ-layer interposed between the solid electrolyte and the inert Pt electrode. The process flow is the same as the Cu/TaO_x/Pt nonvolatile switching devices except the insertion of the δ-layer. The parameters of electron beam deposition are listed in Table 3-1. Fig. 3-6(b) shows 15 consecutive volatile switching cycles of a Cu/TaO_x/δ-Cu/Pt cell. As soon as the voltage is swept to zero, the nanofilament dissolves spontaneously, rendering a reset operation for the transition from low resistive state (LRS) to high resistive state (HRS) redundant. The measured HRS to LRS ratio is 10^2 to 10^5.

Table 3-1 Summary of Electron Beam Deposition for Cu/TaO_x/δ-Cu/Pt Devices.

Material	Pt	TaO_x	δ-Cu	Cu
Layer Thickness (nm)	50	32	6.5	150
E-Beam Deposition Rate (Å/s)	1	1	0.7	5
Melting Temperature (°C)	1768	1872	1085	1085
E-Beam Current (mA)	180	150	80	120
E-Beam Base Pressure (Torr)	2×10^{-6}	2×10^{-6}	2×10^{-6}	2×10^{-6}
Density (g/cm^3)	21.45	8.2	8.93	8.93
Z-ratio	0.245	0.3	0.437	0.437
Tooling Factor	140	140	140	140

We postulate that the reason for the spontaneous dissolution of the CF is an upset balance between the field-supported Cu^+ flux (F_{Cu}^+) and the self diffusion flux of Cu (F_{Cu}) in the CF and through the interface between the Cu bridge and the Cu δ-layer on the Pt electrode as shown conceptually in Fig. 3-7(a). In the absence of Cu δ-layer (i.e. the case of conventional devices), the Cu diffusion flux at the interface of CF with Pt electrode is null because of the inert electrode's ion stopping power. When the device is in the SET condition, only the flux F_{Cu}^+ is significant. The F_{Cu} flux which may deplete Cu atoms from the bridge exists only at the tip of the bridge touching the Cu electrode. Since the radius of the contact cross-section between the filament and Cu electrode is less than 10 nm, F_{Cu} must be perforce small. Hence, while operated in the positive voltage regime the bridge tends to strengthen decreasing its resistance in the

process. The self-diffusivity of Cu is almost two orders of magnitude higher than its intrinsic diffusivity in Pt [12]–[14]. The activation energies of Cu self-diffusion are extracted as 2.48 eV (57.2 kcal/mol) in Ref. [12] and 2.04 eV (47.14 kcal/mol) in Ref. [13], respectively. The surface diffusivity of Cu on Cu is even higher than in the bulk Cu. The activation energy of surface diffusion is 0.9 eV [15]. The insertion of Cu δ-layer enables a Cu diffusion flux from the established Cu bridge at its broad base (opposite end to the tip of the bridge) into the δ-layer and the flux is additionally enhanced by the elevated local temperature resulting from Joule heating. Thus the bridge at the interface with Cu δ-layer is enhanced both by geometry of the bridge and by the thermal effect. This Cu self-diffusion flux (F_{Cu}) tends to remove Cu from the CF. If the removal of Cu is larger than the incoming Cu^+ flux ($F_{Cu}{}^+$), the CF is bound to dissolve. For 5 nm to 8 nm Cu δ-layers, a thicker Cu δ-layer may lead to larger F_{Cu}. The dependence on δ-layer thickness will be noticeable only for 5 nm to 8 nm Cu δ-layers. Beyond a critical thickness, the F_{Cu} flux will cease to depend on the

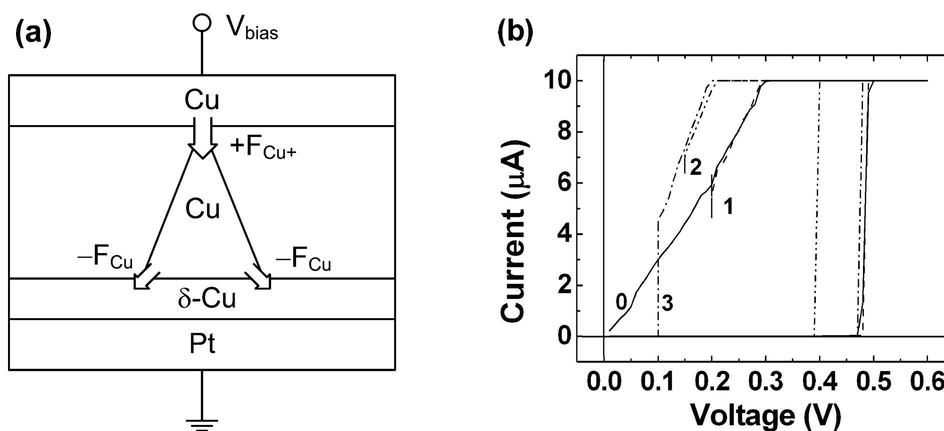

Fig. 3-7. (a) Conceptual view of the Cu^+ and Cu fluxes in volatile switching devices. (b) Resistive state transition during the volatile switching operations. For curves 1, 2, and 3, the sweep is halted at a small but non-zero voltage.

thickness of the δ-layer and would start to behave like a bulk Cu electrode.

To verify this hypothesis, we have manufactured Cu/TaO_x/Cu devices and confirmed that Cu bridge formation is not the same memory switching as Cu/TaO_x/Pt devices. The Cu atoms of CF formation can dissolve quickly in the Cu counter electrode due to elevated local temperature. To test this hypothesis of Cu self-diffusion flux further, voltage for the SET operation for the δ-Cu devices has been swept in positive direction and then back toward zero. However, before reaching 0 V, the voltage sweep has been suspended at a finite voltage and let sit for some time. The results of the interrupted sweep are shown in Fig. 3-7(b). For curves 1 and 2, the negative sweep has been halted at 0.2 V and 0.15 V, respectively. An abrupt current drop can be observed (equivalent to Cu bridge resistance increase) but stabilizes at a lower value indicating an unruptured Cu bridge with higher R_{ON} resistance. CF appears to stabilize itself by increasing R_{ON}, thus reducing the current, Joule heating, and, by extension, F_{Cu}. For curve 3, however, the negative voltage sweep has been halted at 0.1 V, and the resistance increased to the R_{OFF} state, indicating that CF has ruptured. In case of curves 1 and 2 the voltage across the electrolyte is still large enough to support F_{Cu}^{+} that is larger than the F_{Cu}. However, for curve 3, F_{Cu}^{+} sufficiently decreased allowing F_{Cu} to rupture the bridge. Curve labeled 0 shows uninterrupted sweep back to 0 V.

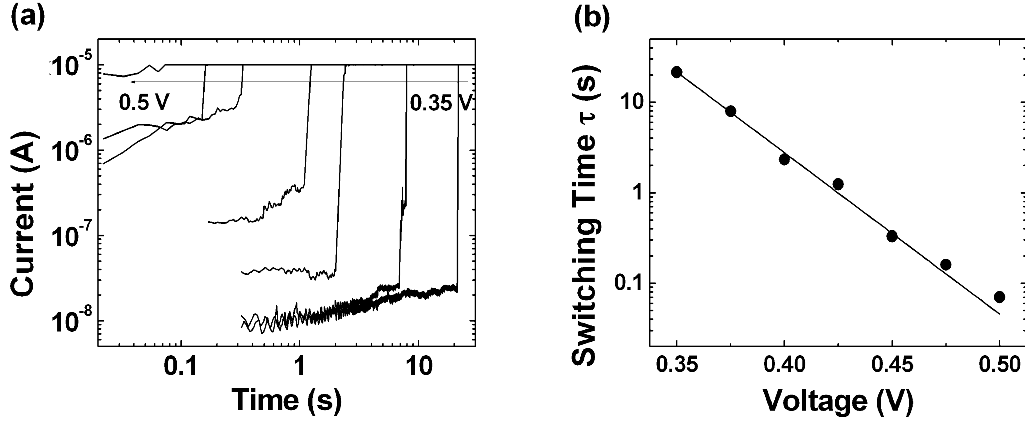

Fig. 3-8. (a) I–t characteristics of the volatile device. The device is biased at constant voltages with the step of 0.025 V. (b) Dependence of switching time on bias voltages of the volatile Cu bridge.

In Fig. 3-8(a), the switching time τ of the device is shown for a constant applied voltage at various values between 0.35 V and 0.5 V. It can be seen that as the voltage increases, the transition from HRS to LRS becomes less abrupt. The switching time τ can be fitted by an exponential function $\tau = \tau_0 \exp(-V/V_0)$ as shown in Fig. 3-8(b).

The exponential relation has been explained by the hopping of Cu^+ ions, the redox reaction on the electrode, and the nucleation of Cu atoms [16]–[18]. The ion hopping velocity v in high electric field is described by:

$$v = 2af \exp\left(-\frac{E_a}{kT}\right)\sinh\left(\frac{zeaE}{2kT}\right) \approx 2af \exp\left(-\frac{E_a}{kT}\right)\exp\left(\frac{zeV}{2kT}\frac{a}{L}\right) \tag{3-1}$$

where a is the ion hopping distance, f the Debye frequency, E_a the diffusion activation energy, z the charge states of ion, e the elementary charge, L the thickness of electrolyte layer, V the applied voltage, T the temperature in units of K, and k the Boltzmann constant. The current density i in redox reactions can be modeled by the Butler-Volmer equation:

$$i = i_0 \left[\exp\left(\frac{\alpha z e}{kT} V \right) - \exp\left(-\frac{(1-\alpha) z e}{kT} V \right) \right] \approx i_0 \exp\left(\frac{\alpha z e}{kT} V \right) \tag{3-2}$$

where α is the electrode charge transfer coefficient (between 0 and 1) and i_0 the exchange current density. In this experiment, the applied voltage V (0.5 V) is much larger than thermal energy kT (26 mV). Therefore the current density equation can be simplified to an exponential relation. Assuming the total charge to build a Cu nanobridge is Q_{crit}, the following integration results in the exponential τ–V relation:

$$Q_{crit} = \int_0^{\tau} i_0 \exp\left(\frac{\alpha z e}{kT} V \right) dt \tag{3-3}$$

$$\tau = \frac{Q_{crit}}{i_0} \exp\left(-\frac{\alpha z e}{kT} V \right) = \tau_0 \exp\left(-\frac{V}{V_0} \right) \tag{3-4}$$

In our volatile switching devices, V_0 = 24 mV and $\tau_0 = 3.75 \times 10^7$ s. The nucleation rate J is given in accordance to the atomistic model for electrocrystallization by:

$$J = J_0 \exp\left(\frac{(N_C + \alpha) e}{kT} V \right) \tag{3-5}$$

where J_0 (nuclei/s) is the pre-exponential term which is constant at given constant thermodynamic conditions, and N_C the number of atoms constituting the critical nucleus [19]. Assuming that the switching time is only determined by the nucleation time which is inversely proportional to nucleation rate J (τ~1/J), $V_0 = kT/[(N_C + \alpha)e]$ can be derived from Eqs. (3-4) and (3-5). The value of α in experiment is usually 0~0.5, then we can extract $N_C \approx 1$ according to the τ–V relation [19], [20].

The SET voltages at different voltage ramp rate1s are shown in Fig. 3-9(a). In contrast to conventional nonvolatile devices [21], V_{SET} is largely independent of the voltage ramp rate. Compared to conventional Cu/TaO_x/Pt devices the V_{SET} is

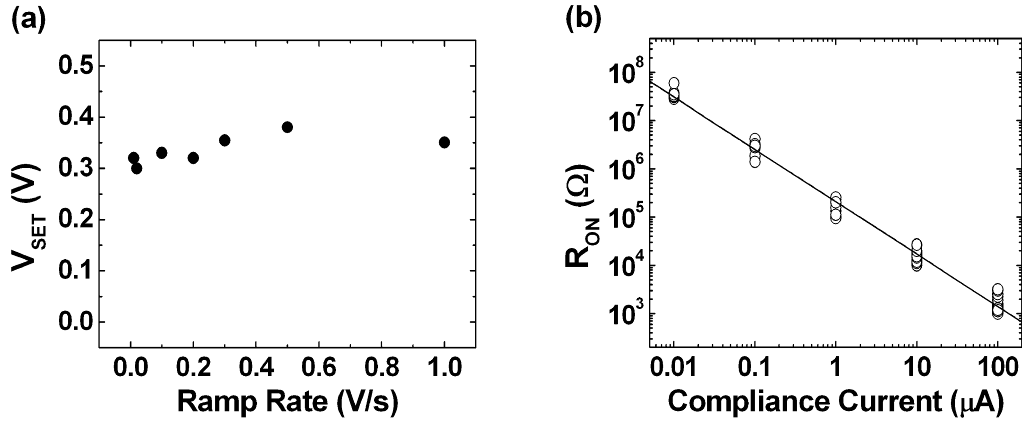

Fig. 3-9. (a) V_{SET} of volatile switching devices at different ramp rates. (b) Dependence of R_{ON} on compliance current of the volatile Cu bridge.

significantly lower for Cu/TaO_x/δ-Cu/Pt devices. Similarly to the nonvolatile resistive switches, the ON-state resistance R_{ON} depends on the compliance current I_{CC} during the set operation. The relation can also be fitted by a reciprocal function, $R_{ON} = K / I_{CC}$, as shown in Fig. 3-9(b).

Figs. 3-10 show R_{ON} and R_{OFF} for different device area. The device cells are squares with length of 15, 20, 25, 30, and 35 μm. As the off-state current increases with the bias voltage nonlinearly as shown in Fig. 3-6(b), the resistance is not constant for the high resistance state. The off-state resistance R_{OFF} is read at 0.1 V in Fig. 3-10. R_{OFF} decreases with the area, inferring that the leakage current in HRS is homogeneous in the cell. Since the current flows through an insulator layer instead of a metal layer, R_{OFF} does not follow the reciprocal relation R~1/A in the resistance equation. The homogeneous conduction across the insulating layer does not necessarily mean the whole area conducts current at the same level.

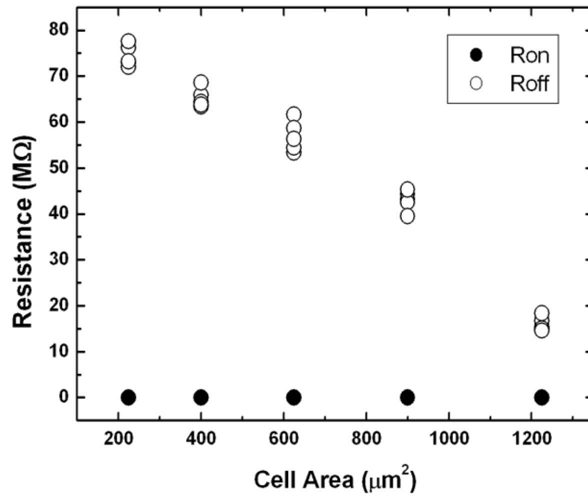

Fig. 3-10. R_{OFF} at different device area. R_{OFF} decreases with the area, which indicates the switching in OFF-state is homogeneous across the device cell. Very high HRS/LRS ratio is also achieved in the device.

R_{ON} is constant at different read voltages and does not show strong correlation with the cell area, as shown in Fig. 3-11. The independence of R_{ON} on cell area indicates the filamentary conduction mechanism. The conduction path in the dielectric only occupies a small area instead of the whole electrode area. The compliance

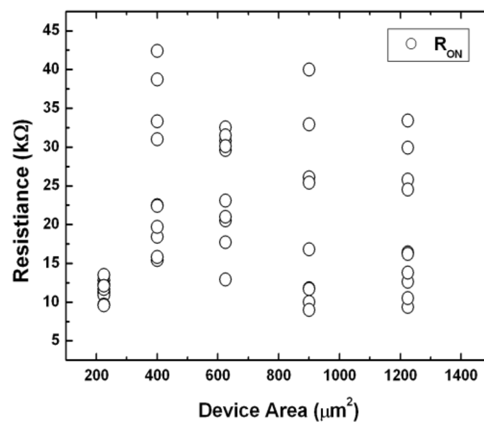

Fig. 3-11. R_{ON} at different device area. R_{ON} does not depend on device area, which indicates the filamentary type switching in the devices.

current is 10 μA for the measurements. The fluctuation appears between 10 kΩ to 45 kΩ, which can be attributed to the shape, structure, and defects of the conductive nanofilaments.

When the same device is operated at high current of about 1 mA, a transition from volatile to nonvolatile switching is observed. In Fig. 3-12 the same device has been tested under a high compliance current of 1 mA. The Cu bridge becomes now nonvolatile and a RESET operation is needed to rupture the bridge. The V_{RESET} voltage is about −0.6V. After the RESET, the device can be again reliably operated in the volatile mode if the compliance current is 10 and 100 μA and characteristics as shown in Fig. 3-6(b) are fully recovered. Thus the δ-Cu device can be switched reliably from volatile to nonvolatile I–V behavior.

The transition from nonvolatile to volatile behavior is governed by the balance between transport of Cu atoms and ions. When the Cu^+ flux overwhelms the Cu sinking flux, the Cu atoms start to accumulate and the CF grows. When the Cu^+ flux

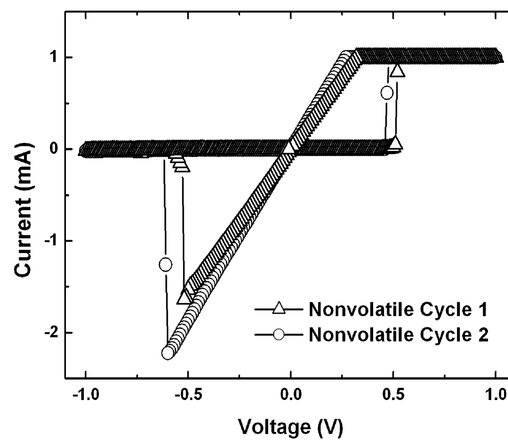

Fig. 3-12. Nonvolatile switching of Cu/TaO_x/δ-Cu/Pt devices at high compliance current of 1 mA.

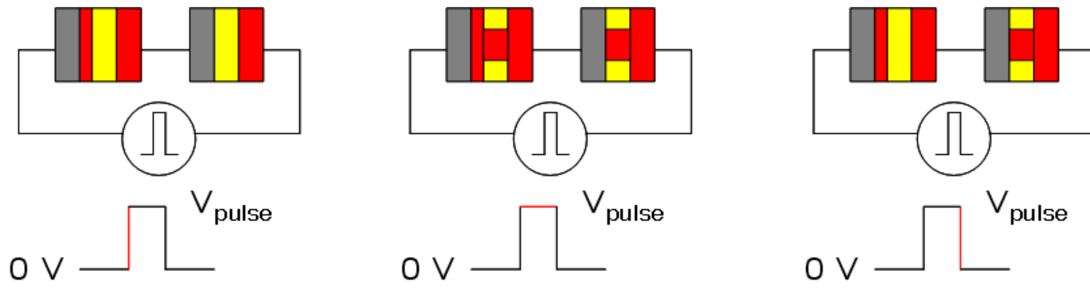

Fig. 3-13. Application of volatile switching Cu/TaO_x/δ-Cu/Pt as selection devices.

is very low, the ions can easily dissolve in the δ-Cu layer or diffuse laterally on the inert electrode. Therefore the nonvolatile resistive switching appears at high compliance current whereas volatile resistive switching appears at low compliance current.

The volatility of Cu/TaO_x/δ-Cu/Pt device does not allow it to work as the nonvolatile memory. However, it can work for the purpose of selection switch as shown in Figs. 3-3 and 3-4. The volatile device can be serially connected to a nonvolatile resistive switching device such as Cu/TaO_x/Pt. When a voltage pulse is applied to the two devices series, the volatile switching device can conduct current only in the time interval that a pulse is non-zero. Once pulse voltage diminishes, the volatile device restores the high resistance state and isolates the nonvolatile switch from the sneak current path. For this configuration, the nonvolatile and volatile switching devices can be fabricated in the same process based on Cu, TaO_x, and Pt deposition. The switching and selection process is shown in Fig. 3-13.

3.4 Effect of Interfacial Layers on Device Fluctuations

The distributions of R_{ON}, R_{OFF}, and V_{SET} are shown in Fig. 3-14. With the Cu δ-layer, tighter distribution of V_{SET}, R_{OFF}, and R_{ON} have been obtained in Cu/TaO_x/δ-Cu/Pt devices than in nonvolatile Cu/TaO_x/Pt devices. Insertion of a Cu δ-layer with thickness below 6.5 nm offers a new control parameter to optimize nonvolatile switching performance of Cu CF based resistive switching devices.

The Cu δ-layer provides homogeneous nucleation sites for Cu ions which is important for the initial phase of Cu nanofilament growth. Cu nanocrystals have also been embedded at the electrolyte-electrode interface for narrowing the fluctuation of SET voltages as well as ON-resistances [22]. The non-uniformity of embedded Cu nucleation sites also disturb the electric field distribution in the solid-electrolyte and thus accelerate the Cu^+ migration locally. Accelerating Cu^+ is equivalent to thinning the electrolyte and will result in lower forming voltage. The nucleation sites also controls the location of conductive filament which could enhance the device

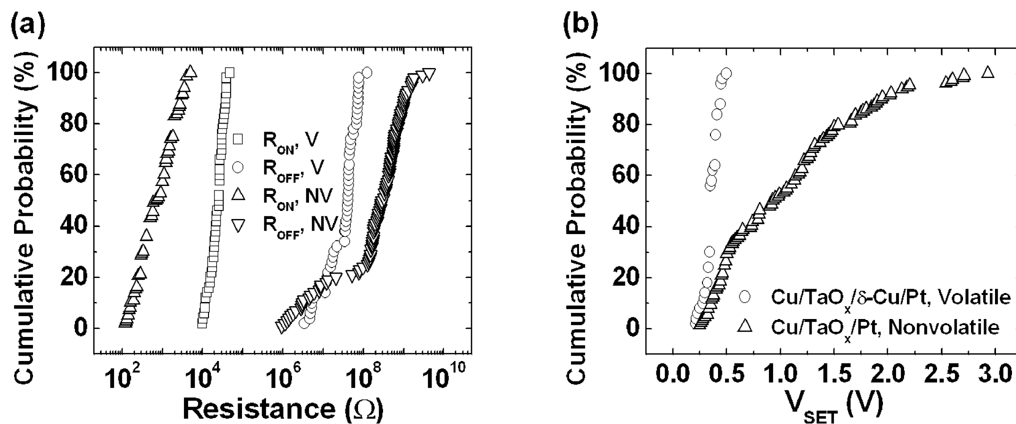

Fig. 3-14. (a) R_{ON} and R_{OFF} distributions of volatile (V) and nonvolatile (NV) devices. (b) V_{SET} distribution of volatile and nonvolatile devices.

scalability and guide the memory cell design.

A thinner Cu layer is embedded between the solid electrolyte and the inert Pt electrode. The thickness of δ-Cu layer is 3.5 nm according to the quartz crystal microbalance in PVD 250. The layer is so thin that the Cu dissolving effect is not as good as the thick δ-Cu layer. The devices exhibit nonvolatile memory switching behavior as expected. The statistical distributions of resistances and voltages are shown in Fig. 3-15. Compared to the Cu/TaO_x/Pt nonvolatile memory devices, the

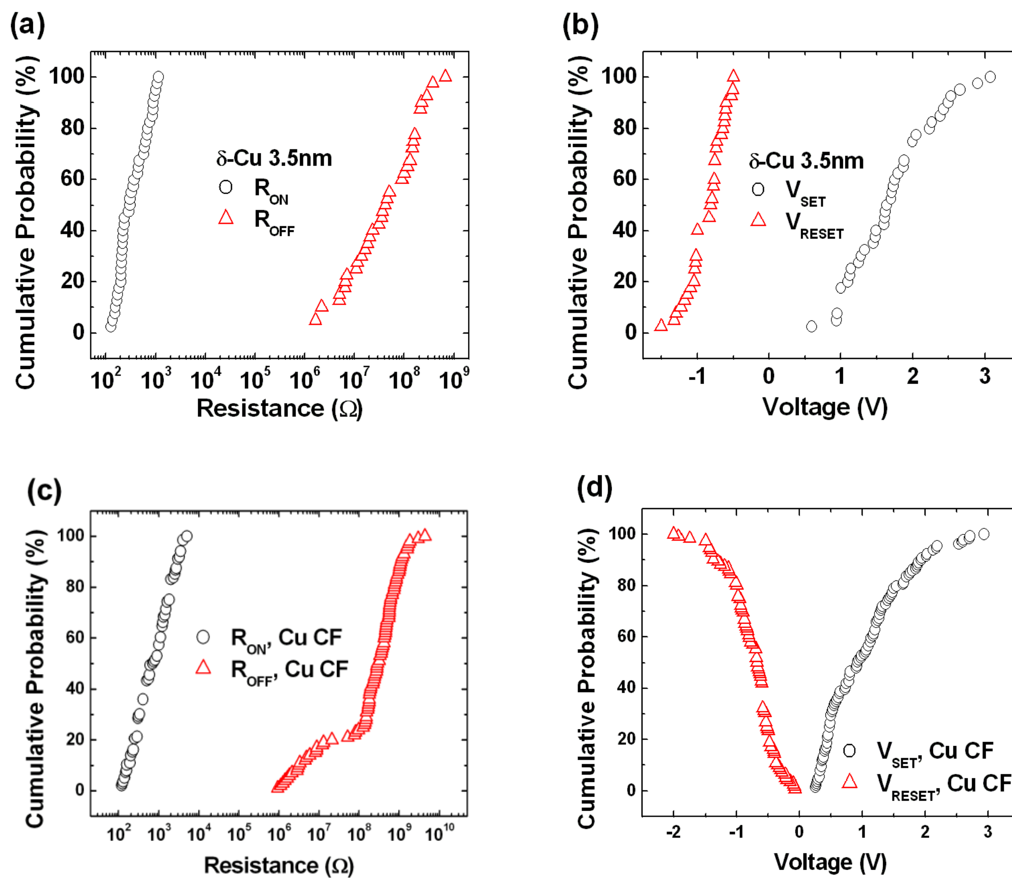

Fig. 3-15. Comparison between Cu/TaO_x/Pt devices and Cu/TaO_x/δ-Cu/Pt nonvolatile devices. The thickness of d-Cu layer is 3.5 nm. With thin δ-Cu layer, the devices are nonvolatile memory and the δ-Cu layer provides nucleation sites for Cu ions. (a) R_{ON} and R_{OFF} distribution of Cu/TaO_x/δ-Cu/Pt devices. (b) V_{SET} and V_{RESET} of Cu/TaO_x/δ-Cu/Pt devices. (c) R_{ON} and R_{OFF} distribution of Cu/TaO_x/Pt devices. (d) V_{SET} and V_{RESET} of Cu/TaO_x/Pt devices.

fluctuations of $Cu/TaO_x/\delta$-Cu/Pt devices are decreased. Therefore the Cu δ-layer offers another technology parameter for improving the performance of resistive memory devices.

3.5 Summary

A thin layer of Cu on the inert Pt electrode can help the nucleation of Cu ions and improve the switching voltage uniformity of resistive memory devices. As the thickness of this δ-Cu layer increases, the resistive nonvolatile switching is possible to transistion to volatile switching. The volatile switching does not need a reset operation and shows SET voltage that is independent of the ramp rate. In a volatile CF switch the low resistance on-state can be maintained only for an applied voltage larger than a minimum voltage. The flux of Cu^+ is driven by the applied voltage. The flux of Cu atoms is controlled by the thickness of Cu δ-layer. The volatile resistive switching does not rely on the device area, meaning a filamentary type conducting path appears in the insulating film. Based on the I–t characteristics at constant bias voltages, we conclude that the formation of temporary Cu conductive filament is because of the electrochemical reaction at the inert electrode. The volatile switching is explained by the upset of Cu-Cu^+ flux balance. The local Joule heating will enhance the self-diffusion of Cu and destroy the tiny contact between Cu nanofilament and the δ-Cu layer. This model has been justified by the I–V characteristics at constant bias voltages. The volatile resistive switches can be used as the selection device in the nanocrossbar memory architecture.

Chapter 4 Circuit Elements Based on $Cu/TaO_x/Pt$ Devices

In this chapter, circuit elements based on $Cu/TaO_x/Pt$ devices are designed and discussed. The circuit elements consist of two or three identical resistive switches in parallel or serial connections. By utilizing the memristive properties of the single devices, nonlinear I–V characteristics have been achieved in the composite circuit elements. These elements can be used for chaotic circuits and neural networks.

4.1 Introduction

The importance of resistive switches is not only the non-volatile memory applications, but also the potential of working as logic devices. Their memristive properties have been attracting interest from many areas, particularly neuromorphic computation and neural networks. Hardware learning and electronic synapse have been implemented based on the bridge resistive devices [1], [2]. The aim is to build a new kind of "intelligent" computing machine which has similar form, function and architecture to the mammalian brain [3]. This neuromorphic computer, or "artificial brain", can scale to the biological neural system in terms of total number of electronic neurons and synapses and their connectivity. The resistive switching devices have demonstrated similar electrical behaviour to the synapse in the biological neural system. Therefore it is being developed as the nanoscale electronic synaptic component for the connection between electronic neurons [1], [4]. On the other hand, the resistive switching devices are called "the fourth element" in addition to resistor,

capacitor, and inductor [5], [6]. Their unique memristive characteristics enable the chaotic circuits. In this chapter, we investigated the performances of circuit elements in circuit applications. The circuit elements consist of several resistive devices in particular connections to realize interesting functions. The experimental device characteristics should provide references to the circuit model and hardware development.

4.2 Complementary Resistive Switches (CRS)

The complementary resistive switches (CRS) are the first circuit element fully built upon conductive bridge resistive memory devices. It is proposed as one of the solutions for sneak path problem in the crossbar memory architecture. Different from 1T1R or 1D1R selection device (transistor, threshold switching devices or diodes as the switching element serially connected to the memory switching device), two memory switching devices are anti-serially connected sharing the same central

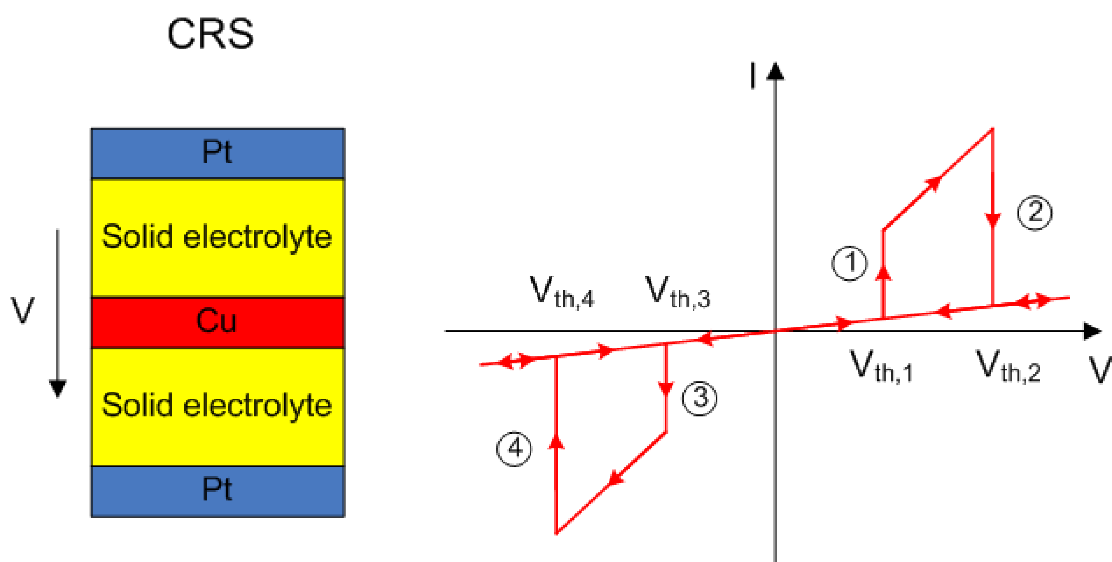

Fig. 4-1. Device structure and I–V characteristics of complementary resistive switches [7].

electrode [7]. If both devices are identical, this composite device shows symmetric behavior. The two resistive memory devices alternatively set and reset, i.e. when the top device is ON, the bottom device is OFF. Only during a short switching period the two connected devices are in ON state and the current flowing through CRS is high. This high current causes significant amount of heat melting one of the conductive filaments and the CRS transitions from low resistance state to high resistance state. The device structure and I–V characteristics of CRS are shown in Fig. 4-1. Recently, the CRS has been demonstrated not only in CBRAM devices, but also in oxide-based RRAM devices [8]–[11]. The CRS is also one of the memristor combinations realizing symmetrical memristive properties [12].

4.3 Antiparallel Resistive Switches (APS)

Antiparallel resistive switches have been conceived recently for chaotic circuit

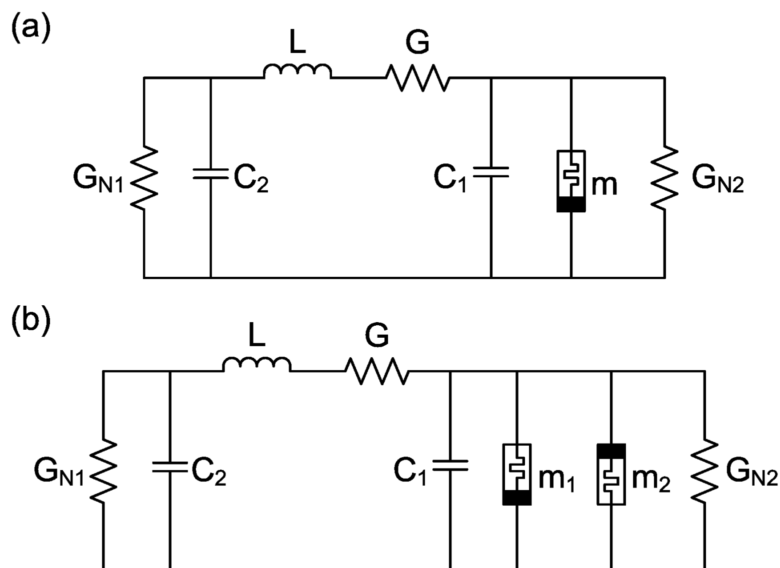

Fig. 4-2. (a) The chaotic circuit based on one memristor (canonical Chua's oscillator). (b) The chaotic circuit based on two memristors in antiparallel. The elements m, m_1, and m_2 represent memristors [13].

applications [12]–[14]. Fig. 4-2 shows the typical chaotic circuit under investigation where the antiparallel resistive switches may be used. It has been found that a neural circuit using a memristive synapse with symmetric charge-flux nonlinearity can behave chaotically. Though theoretical modeling has been done, the experimental verifications are still insufficient for the aforementioned chaotic circuits. Our work demonstrated the first APS with CBRAM type memristors.

The circuit and single device of APS are shown in Figs. 4-3(a) and 4-3(b), where two Cu/TaO_x/Pt cells are connected in an antiparallel configuration by two pairs of external probes, one of which connects the Pt electrode of one switch with the Cu electrode of the second switch. The triangle inside the switch indicates CF formation within the solid electrolyte of the switch. The base of the triangle is anchored in the platinum inert electrode and the tip of the triangle points toward the Cu electrode. As soon the tip makes a contact with the Cu electrode, the device is in a conductive ON

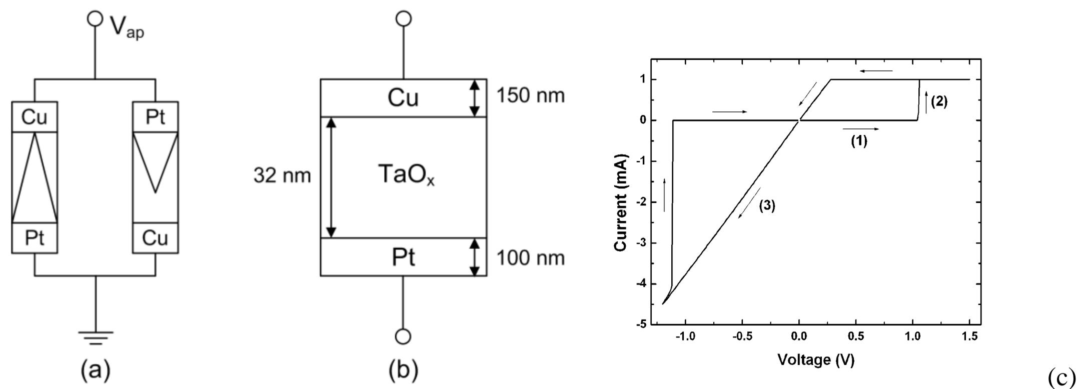

Fig. 4-3. (a) The device structure of anti-parallel resistive switches (APS). (b) Layer structure of a single switch. The shown layer thicknesses are not drawn to scale. (c) The bipolar switching characteristics of a single Cu/TaO_x/Pt cell. The set voltage is 1.05 V and the reset voltage is −1.11 V. The set and reset voltages of Cu/TaO_x/Pt cell are typically ± (1 to 2) V and the reset current is 1 to 5 mA.

state.

In order to explain the switching behavior of a circuit of two anti-parallel resistive switches, the single devices have been thoroughly characterized. Fig. 4-3(c) shows a typical behavior of one switching cycle of an individual switch. Initially the switch is disconnected. The voltage is ramped (1) from 0V on the positive voltage axis. As long as the switch is in the OFF state the current is very small. When the voltage reaches V_{SET}, the CF is established (2) and the current jumps abruptly being only limited by compliance current lest the device be damaged. Then the voltage is swept back and, for voltages close to zero, an ohmic behavior is observed (3) until a negative voltage V_{RESET} is reached when the CF is ruptured, and the current collapses to a small value. For our devices, V_{SET} = 0.9 to 1.5 V, V_{RESET} = (−1.0) to (−2.0) V, and reset currents I_{RESET} are in the range of 1 to 5 mA.

A typical behavior of I–V characteristics of APS is shown in Fig. 4-4, after one switch has been pre-programmed into an ON state. The switches have been characterized individually with following results: the set and reset voltages are −2 V and 1.34 V for switch 1, and 1.72 V and −1.12 V for switch 2, respectively. The initial programming of one of the switches switch can be done individually or in the context of APS device. The latter programming is always possible, since under either voltage polarity one of the switches will be amenable to CF formation while the other will be precluded from forming CF by the virtue of CF formation and rupture dynamics. In Fig. 4-4 we apply first a voltage on the positive axis creating a condition either to rupture the CF in the switch 1 or to form CF in the switch 2. It can be seen from the

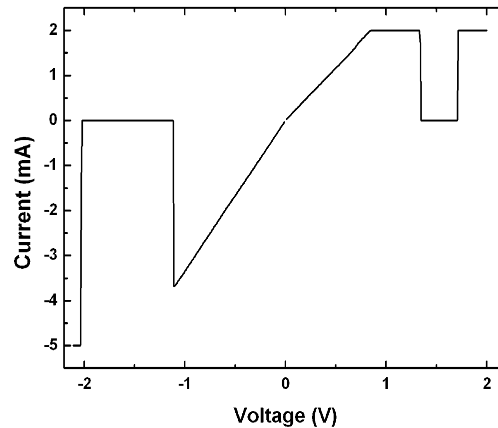

Fig. 4-4. I–V characteristics of two anti-paralleled resistive switches. The set and reset voltages are –2.0 V and 1.34 V for switch 1, and 1.72 V and –1.12 V for switch 2. On the positive switching side, cell 1 switched off before cell 2 switched on. With negative voltage bias, cell 2 switched off before cell 1 switched on. The compliance current is 2 mA for the positive switching and 5 mA for the negative switching.

Fig. 4-4 that the CF formed in switch 1 ruptures at 1.34 V and the current drops to very small values and remains at zero until the CF in the switch 2 is formed at 1.72 V. At this point, the initial state ON/OFF in (switch 1)/(switch 2) configuration has been flipped to OFF/ON state. The flipped device is now subjected to a negative voltage sweep and exhibits an ohmic behavior. One notices that the slope on the negative voltage axis is different from the slope on the positive axis. The slope on the positive axis is determined by the $R_{ON}(1) = 430\ \Omega$ resistance of the switch 1, while the slope on the negative voltage axis is determined by the $R_{ON}(2) = 305\Omega$ resistance of the switch 2. When the voltage reaches –1.12 V, CF in switch 2 ruptures and the APS device as a whole is again in a non-conductive (OFF) state. As the negative voltage sweep continues it reaches subsequently the $V_{SET} = -2.0$ V at which the CF in switch 1 is formed again. Such I–V characteristics could be cycled a couple of times with

slight shift of the V_{SET} and V_{RESET} voltages for both switches.

It is of interest to compare the I–V characteristics of APS device with those of the CRS device [7] and RFED device [15]. APS device exhibits a high current in voltage interval containing the origin, whereas CRS and RFED display zero current. Then on both negative and positive voltage axis there is a finite voltage interval where for APS device has zero current whereas CRS and RFED display a high current. Moreover, beyond these finite voltage intervals APS yields a high current whereas CRS and RFED zero current. When looking at the I–V characteristic with no compliant currents applied the APS I–V characteristic looks like a ruptured or truncated Ohm's relation, i.e., the current is linear with the voltage except in two finite voltage intervals on the positive and negative voltage axis where the current drops virtually to zero. A related manifestation of the switching behavior is the temporal evolution of the current as function of a constant voltage stress. Again, the initial state of APS is one where switch 1 is in ON state while switch 2 is in OFF state.

The applied constant voltage polarity is applied such that it tends to rupture CF in switch 1 and to form CF in switch 2. A result of such voltage stress for a bias of V_{ap} = 2.5 V is shown in Fig. 4-5. For a long time from 0 s about 16.6 s APS is conductive owing to the ON state of switch 1. At t_1 = 16.6 s the CF in switch 1 ruptures and the current drops to zero. After an additional time interval of about 1.5 s at t_2 = 18.1 s the CF is being formed in switch 2 and the APS is again in a conductive state. The times t_1, t_2, and $\Delta t = t_2 - t_1$, can be controlled by the level of voltage stress. For voltages below ~2 V no switching transitions in single device could be observed. In both cases

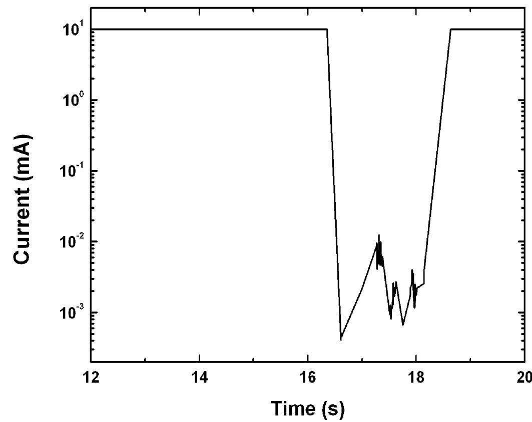

Fig. 4-5. I–t characteristic of APS device. The bias voltage is 2.5 V. The duration of high resistance state is 1.5 s.

shown in Figs. 4-4 and 4-5 the CF of the switch 1 ruptures first before the CF of the second switch can be formed.

This is so since the voltage drop across the APS device is determined by the R_{ON} of the switch 1. As R_{on} is small the voltage drop determined by R_{ON} of switch 1 is too small to attain $V_{SET}(2)$ of the switch 2. As the current is increased further to produce larger voltage drop, it will reach at some point I_{RESET} for switch 1 at which point the CF in switch 1 ruptures before CF in switch 2 can be formed. From this analysis one can derive a condition for both bridges being in an ON state. For this situation, the voltage across APS has to be equal or larger than $V_{SET}(2)$ but smaller than $I_{RESET}R_{ON}(1)$. In Fig. 4-6 an interesting border case of both switches coexisting in conductive states is shown. Initially only switch 1 is in ON state. With increasing voltage current increases linearly, its slope being determined by $R_{ON}(1)$. At V_{ap} = 1.5 V there is an indication that the CF in switch 1 is about to rupture as the current is very close to $I_{RESET}(1)$, but at the same voltage the CF in switch 2 is already being

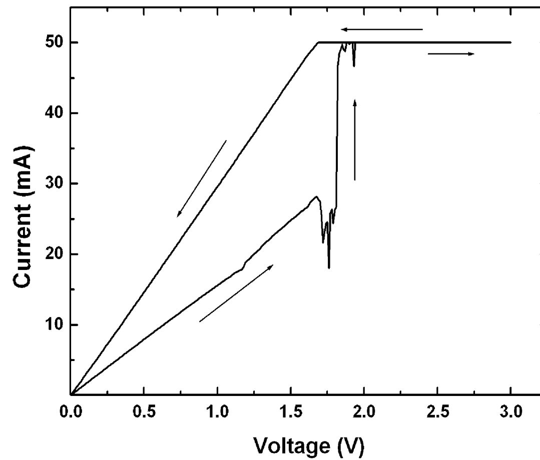

Fig. 4-6. I–V characteristics of anti-paralleled resistive switches different from those in Fig. 4-4. $R_{ON}(1) = 64\ \Omega$ when CC = 15 mA, and $R_{ON}(2) = 162\ \Omega$ when CC = 50 mA.

formed. Hence, the resistance of switch 2 decreases dramatically and the current through switch 1 drops due to the parallel arrangement of both switches significantly below the $I_{RESET}(1)$ level. Due to the reduced current level through switch 1 both switches can now coexist in ON states. The formation of CF in switch 2 leads to a current jump by at least a factor of 2 under a compliance current of 50 mA. When the voltage is swept back the slope of the current is now determined by $R_{ON}(1) \times R_{ON}(2)$ / [$R_{ON}(1) + R_{ON}(2)$] = 34 Ω, confirming a parallel arrangement of both CFs.

The single switches, when stressed at high negative voltage V_{ap}, displayed in some cases switching behavior that cannot be attributed to Cu^+ ion migration but to oxygen vacancies V_O. However, the forming voltages for switching behavior of V_O bridges were all found to be between |4.5 V| and |7 V| and of opposite polarity as for Cu bridges. Other samples at such high voltages resulted in permanently damaged devices. This observation has been addressed in Chapter 2. Hence it is unlikely that

oxygen vacancies play a role in the switching behavior of the anti-parallel switches shown in Figs. 4-4, 4-5, and 4-6 where the voltage has been kept under |3 V| and V_{SET} and V_{RESET} never exceed |2 V|. The switching of APS is fully consistent with the values for forming (V_{SET}) and rupture (V_{RESET}) voltages Cu bridges in single resistive switches.

4.4 APS in Single Cells

The I–V characteristics of anti-parallel resistive switches can be demonstrated in a *single* Cu/TaO_x/Pt device cell. By virtue of Cu and oxygen vacancy V_O nanofilaments, the APS can be realized as shown in Fig. 4-7(a). The V_O and Cu filaments can form and rupture alternatively under the bias voltage of opposite polarities, constituting an anti-parallel connection of two, electrically, nearly identical memristors.

In Fig. 4-7(b) a typical stable switching cycle of an integrated APS switch is

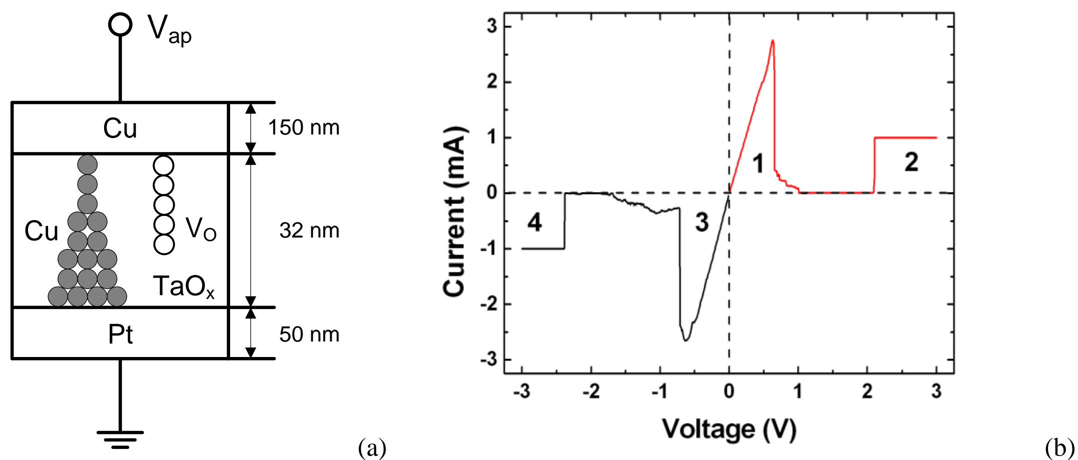

Fig. 4-7. (a) Cu and V_O bridges in the same device cell. (b) One switching cycle of anti-parallel switching Cu and V_O CFs in a single 10 μm Cu/TaO_x/Pt cell. Multiple switching cycles have been measured in the voltage sweeping mode.

shown in a compact form. The bias voltage sweeps between −3 V and 3 V. The compliance current is 1 mA for SET operation whereas 10 mA for RESET operation. When the positive voltage sweep begins at 0 V, a V_O CF has been already formed. The current increases linearly according to $V_{bias}/R_{ON}[V_O]$, where $R_{ON}[V_O] = 237\ \Omega$. At $V_{RESET}[V_O] = 0.8$ V the oxygen vacancy filament ruptures and the device transitions into the OFF state (segment 1). As the voltage increases the forming of the Cu bridge is observed at $V_{SET}[Cu] = 2.1$ V (segment 2). In order not to obscure the plot the voltage is not swept back but a new negative voltage sweep begins at 0 V. The current increases on the negative *x*-axis according to $V_{bias}/R_{ON}[Cu]$, where $R_{ON}[Cu] = 206\ \Omega$. The Cu bridge ruptures at $V_{RESET}[Cu] = -0.8$ V (segment 3). As the negative voltage sweep continues the oxygen vacancy filament is formed at $V_{SET}[V_O] = -2.5$ V (segment 4). At this point, a new identical cycle can begin. The unique I–V characteristic is caused by the forming and rupture of Cu and V_O conductive filaments within a single cell. The cell switches alternatively on and off in one cycle displaying the same characteristic as two anti-parallel connected individual cells. To avoid irreversible damage, compliance current is applied to the device for the SET operations.

Multiple switching cycles are shown in Fig. 4-8. The magnitude of negative SET voltage is generally higher than the positive SET voltage. This V_{SET} variation implies the different conduction mechanisms for the positive and negative SET processes. With a current compliance, the LRS resistance is regulated and therefore the endurance of APS switching is improved.

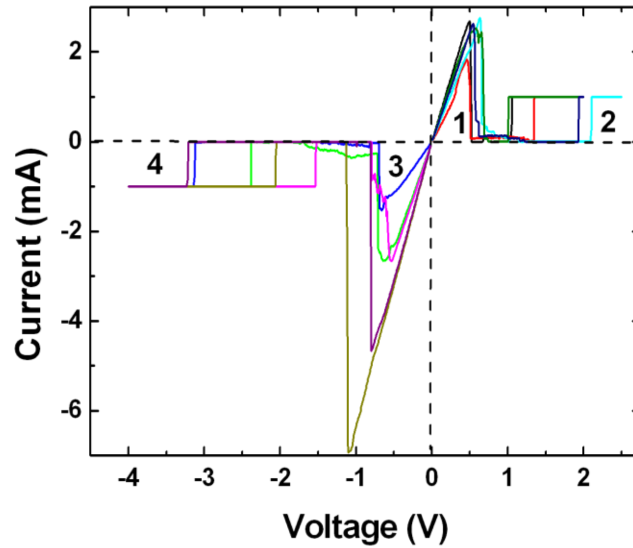

Fig. 4-8. Multiple switching cycles of APS in single devices. Steps 1 to 4 are the same as Fig. 4-7.

4.5 Cascaded Resistive Switches

At a given applied constant voltage V_{ap} across the switch, a finite time τ is required to establish a conductive filament. For large enough V_{ap}, an exponential relation between V_{ap} and τ is observed, $\tau = \tau_0 \exp(-V_{ap}/V_0)$, where τ_0 and V_0 are material constants [16]–[18]. This equation is derived from Eqs. (3-2) to (3-4) by considering

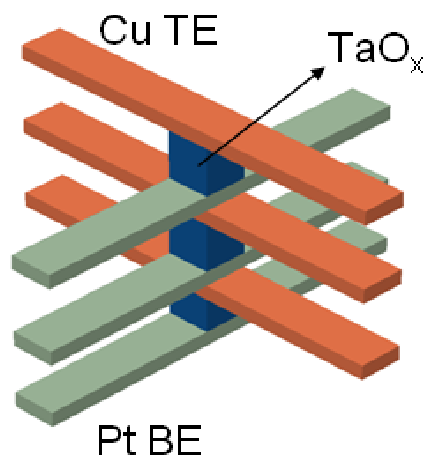

Fig. 4-9. Conceptual illustration of three cascaded resistive switches. TE and BE mean the top electrode and bottom electrode. Orange, blue and green materials represent Cu, TaO_x, and Pt.

redox reaction and atomistic nucleation. The cascaded resistive switches are conceived based on the exponential τ–V relation. The conceptual illustration of cascaded resistive switches is shown in Fig. 4-9. Three Cu/TaO_x/Pt devices are connected in a serial way, i.e. a Cu electrode is connected to a Pt electrode and only two outer electrodes (top Cu and bottom Pt) are available for electrical connection. The purpose of this cascade connection is to investigate the nonlinear switching characteristics of the cascaded SET processes. This SET process is schematically illustrated in Fig. 4-10. In the figure, resistors represent the LRS resistance R_{ON}. The switches represent the HRS resistance R_{OFF} when it is open, and $R_{ON} << R_{OFF}$. If the switch is closed, its resistance is zero. A resistive device consists of one resistor and one switch in series. When the switch is in its OFF state, the resistance of the device is roughly R_{OFF}. When the device is set, the switch is in its ON state and the resistance of the device is R_{ON}. If the three switches in

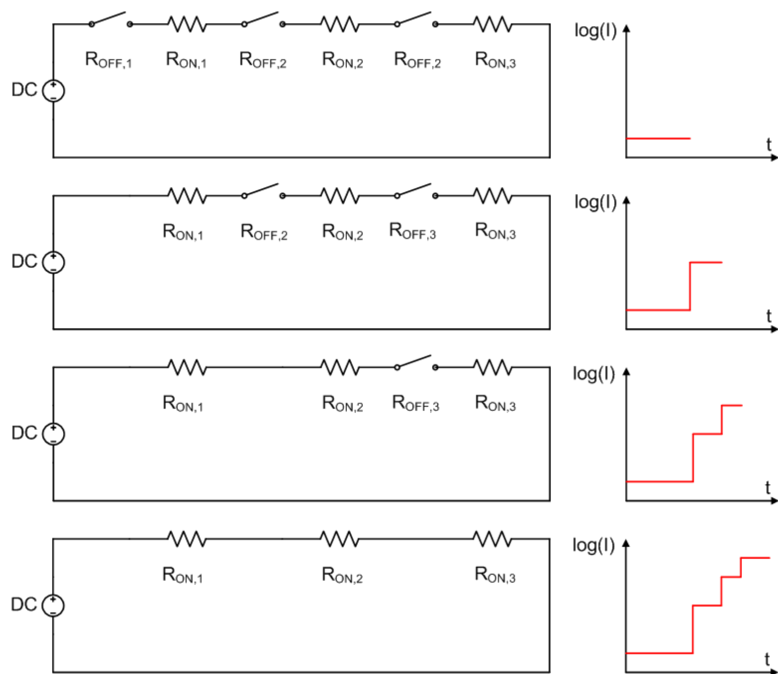

Fig. 4-10. Schematic illustration of the SET process of cascaded resistive switches.

Fig. 4-10 are turned off one by one, the staircase-like current characteristics can be observed in the semilog scale.

Two and three single resistive switches have been selected, characterized individually, and then serially connected externally with 4 and 6 probes. When R_{OFF} and R_{ON} of the resistive switches are selected judiciously, then, based on Eq. (3-4) and on the voltage division principle, one can estimate which switch at what time will transition from the OFF-state to the ON-state. As a result, the transitions from OFF to ON states for individual switches will proceed in a cascaded manner at predetermined times and at predetermined current levels. The concept is demonstrated on two and three serially connected switches.

Fig. 4-11 shows the measured output current I_{out} of two serially connected switches as function of time for V_{ap} = 0.5 V. It can be seen that the I_{out} displays 3 distinct current levels over a time range of 30 s. The first current level corresponds to the OFF state of

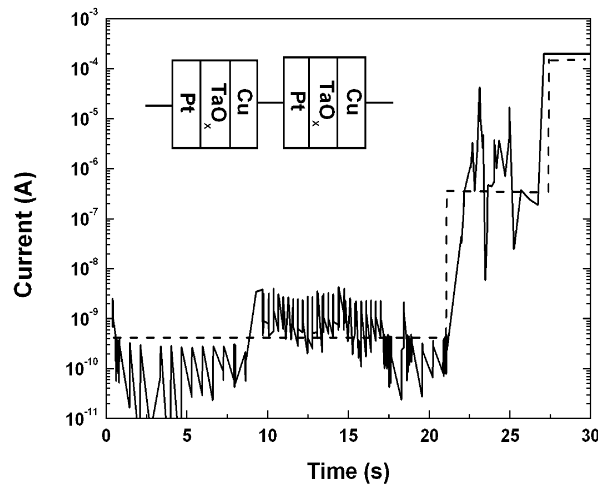

Fig. 4-11. Current characteristics as a function of time of two serially connected resistive switches under a collective voltage stress of 0.5 V.

two bridges, the second level to ON state in one switch while the other is still in OFF state, and the third level corresponds to both bridges in ON state. The stochastic current variations, typical for charge transfer phenomena and random telegraph noise in such systems, have been observed and explained elsewhere [19], [20].

The same arrangement of switches has been measured for V_{ap} = 1.5 V and similar I(t) characteristics is shown in Fig. 4-12. Because of Eq. (3-4) the time scale for the switching transitions shrinks from 30 s to 1.2 s. It is observed that the time between the creation of the two conductive filaments is about 0.1 s for V_{ap} = 1.5 V whereas it was 5 s for V_{ap} = 0.5 V. Increasing V_{ap} beyond 1.5 V decreases further the time scale of current level transitions. At a high enough voltage transitions of the two switches will merge into one, as the creation of conductive filament in the first switch is immediately followed by the creation of conductive filament in the second device. No switching

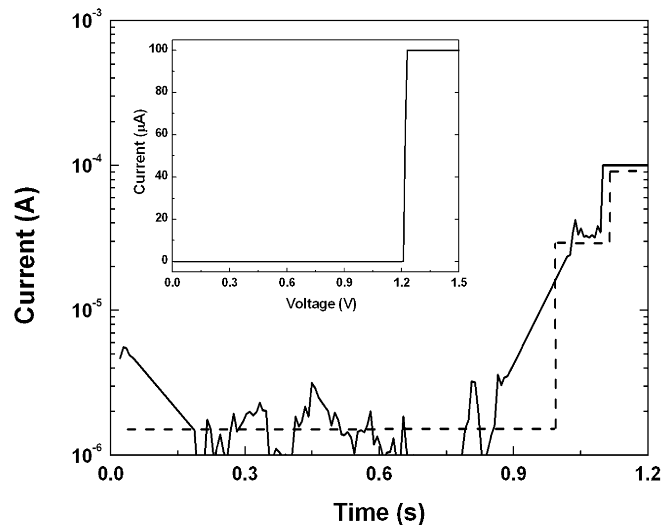

Fig. 4-12. Current characteristics as a function of time of two serially connected resistive switches under a collective voltage stress of 1.5 V. The inset shows switching behavior of the 2nd individual cell.

transitions could be observed for V_{ap} substantially smaller than 0.5 V (in general, a cell-specific minimum voltage V_{ap}) even for long time of several minutes.

Fig. 4-13 shows I–V characteristics of three serially connected switches. The single cells have been characterized individually before being subjected to a collective voltage stress resulting in: $R_{ON}(1)$ = 1700 Ω, $R_{OFF}(1)$ = 9 GΩ, $R_{ON}(2)$ = 1400 Ω, $R_{OFF}(2)$ = 12 MΩ, $R_{ON}(3)$ = 219 Ω, $R_{OFF}(3)$ = 145 MΩ. The I(t) curve in Fig. 4-8 exhibits three sharp transitions at 5.5 s, 7.5 s, and 8.1 s. From the resistance values given above the four current levels can be estimated as follows: the first level 2×10^{-10} A, the second level 10^{-8} A, the third level 10^{-7} A, and the fourth 1 mA. The fourth current level is the current when all three cells are in ON states. This current level has been indeed observed. However, in Fig. 4-13 the maximum current level has been limited by a compliance current of 0.2 mA lest the switches are damaged irreparably. The estimated current levels correspond to the measured ones except for the third

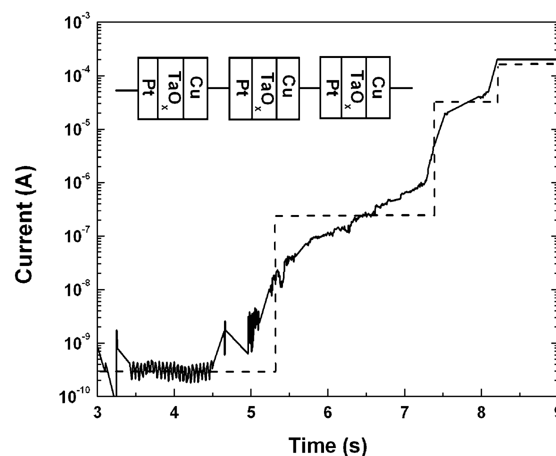

Fig. 4-13. Current characteristics as a function of time of three serially connected resistive switches under a collective voltage stress of 1.4 V.

level which is measured as close to 5×10^{-5} A. This may be attributed to a degradation of $R_{OFF}(3)$ during the initial stages of the stress. As can be seen in the I(t) curve, the I_{out} between the transitions displays a positive slope. This slope can be explained by R_{ON} decrease of the connected cells due to experienced current levels flowing through the cells. After all three bridges have been subjected to the collective voltage stress, the cells have been re-characterized individually: $R_{ON}(1) = 500\ \Omega$, $R_{ON}(2) = 400\ \Omega$, $R_{ON}(3) = 200\ \Omega$. Comparing the values before and after the collective voltage stress, the R_{ON} of the first two cells has decreased by more than a factor of three. This dependence is relevant for the two and three switches in series as the current I_{out} passing through all the switches is kept at a range of values (corresponding effectively to a compliance current constraint). These currents are limited to few μA as long as one of the cells is still in an OFF state.

The switching times observed in Figs. 4-11, 4-12, and 4-13 can be estimated from voltage drops $V_{cell}(j)$ across the cells from Eq. (4-1) based on the single switch characteristics, where

$$V_{cell}(j) = \frac{V_{ap} R_{cell}(j)}{\sum R_{cell}(i)} \qquad (4\text{-}1)$$

The equations for the current levels are given by

$$I_{out} = \frac{V_{ap}}{\sum R_{cell}(i)} \qquad (4\text{-}2)$$

with $R_{cell}(i)$ (i = 1, 2, 3) being the resistance of cell (i) during the voltage stress. Plugging $V_{cell}(j)$ into (3-4) determines the switching time τ_{crit} assuming that the cells have not subjected to a voltage stress before. This is an approximation, at least for all

cells but the first one, since all cells are stressed during the time period when the first cell undergoes a transition from OFF to ON state. It is noted that in Eq. (4-2) resistive voltage division principle has been invoked. However, capacitive voltage division between the switches in OFF states could be applicable as well. In either case, as a first approximation, $R_{cell}(i)$ is assumed to be equal either to $R_{OFF}(i)$ or $R_{ON}(i)$. One observes that $R_{ON}(i)$ can decrease gradually, particularly when other cells are still in the OFF state and elevated voltage bias is kept in place for an extended period of time. This effect of decreasing R_{ON} in a single cell is known in literature [16], [21], [22] and plays a role in a series arrangement of switches as explained further below. The current levels in Figs. 4-11 and 4-12 are different due to wide range of R_{OFF} for TaO_x varying $10^6 \sim 10^9$ Ω. Fig. 4-14 shows the times for each SET process and ON-state resistances for each current level in Fig. 4-13. They can be roughly fitted by an exponential equation which justifies the switching mechanisms.

A single solid atomic switch with learning and unlearning abilities has been

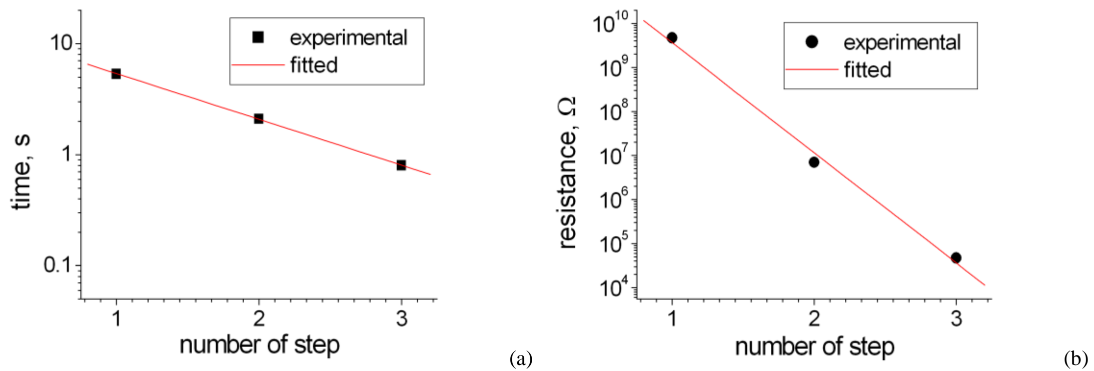

Fig. 4-14. (a) Time for each SET process and (b) ON-state resistances for each current level of three serially connected resistive switches under a collective voltage stress of 1.4 V.

proposed in the past by Hasegawa et al [22] and S.-J. Choi et al [23]. Hasegawa et al observed that the conductive filament can be strengthened by widening the diameter of CF after the bridge has been fully established across a 1 nm gap. This phenomenon has been identified as the key feature of the learning/unlearning capability of switches consisting of Ag_2S electrode separated by a vacuum gap of about 1 nm from a Pt electrode [22]. The widening of the bridge diameter caused the R_{on} to decrease gradually with time. However, sensing such slow and gradual decrease of R_{ON} is difficult. In our serial arrangement of switches, the key feature to decrease the resistance of the device is the cascade of individual switches in distinct quantized current levels spanning six orders of magnitude and at predetermined times from nanosecond to second range. Both times and current levels can be tightly controlled by the choice of material properties and the geometry of the constituent switches. Two and three serially connected switches have been selected for demonstration purposes only. More than three switches can be serially connected generating more current levels. For a serial connection of switches in order to keep the current low, one switch staying all the time in an OFF state would be desirable. It would effectively limit the circuit power consumption while still allowing voltages to be around 1 V.

The programming operation of the cascade can be partially reversed. Partial erasure of the cascade occurs when a voltage of opposite polarity is applied. Stressing the device of three switches all in ON states at $V_{ap} = -2$ V results in only two current levels. The reason for this is that the rupture of a conductive filament is determined by the reset current I_{RESET}. The cell with the lowest I_{RESET} ruptures first bringing about

transition from ON- to OFF-state. Consequently, current collapses and is too low to bring about a rupture of conductive filaments in the remaining switches. Thus case of reversing the state in one switch can be termed as partial unlearning. Complete unlearning as well as accelerated learning can be achieved by supplying the simple serial circuit with two additional branches of antiserially connected switches allowing dedicated access to an individual switch. Using control pulses one could then reverse the state in all the individual switches. Control pulses could also accelerate the learning by forcing a certain individual switch in ON state before this may occur due to the regular input wave form.

The entire circuit with the additional branches can be integrated in the crossbar array occupying only 3 crossbar intersections. The metal electrodes between switch 1 and switch 2 as well as between switch 2 and switch 3 may share floating metal plates encapsulated between the top and bottom electrodes. The schematic cross section is shown in Fig. 4-15.

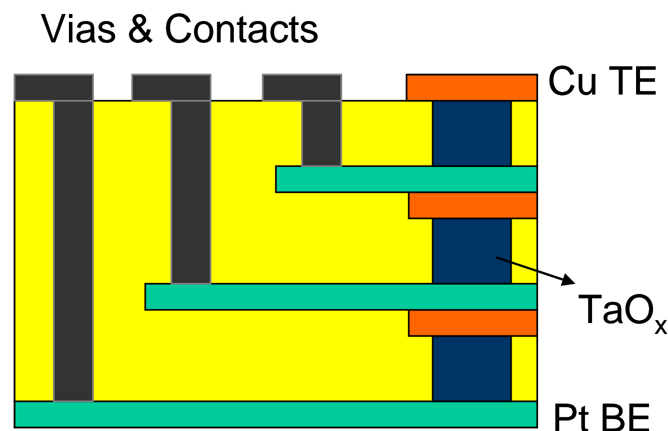

Fig. 4-15. Schematic cross section of integrated cascaded resistive switches in the crossbar array.

4.6 Summary

Antiparallel resistive switches and cascaded resistive switches have been proposed and analyzed. The principle of antiparallel resistive switches has been demonstrated for the case where the voltage sweeps from −3 V to 3 V. The measured symmetric I−V characteristics show truncated Ohm's law. The border case has also been observed for APS during switching. The principle of cascaded switches has been demonstrated for the case where a constant voltage stress in time has been applied collectively to three devices in series. In a general case, the voltage stress may be a function of time, i.e. $V_{ap} = V_{ap}(t)$. The state variable of total injected charge will then be a time integral of the applied voltage stress $V_{ap}(t)$. The desired behaviors have been achieved. Both kinds of circuit elements can be easily implemented in nanocrossbar architecture and be applied to nonlinear neural chaotic circuits.

Chapter 5 Multilevel Cell of CBRAM

Multilevel cell (MLC) is an efficient way to increase the storage capability of the existing device technology. The method is to store more than one bit of data in a single memory cell. This result can be achieved by controlling the physical parameters such as write/erase current or voltage. Without significant modifications of memory architecture or device structure, the volume of data storage is dramatically increased. The multilevel cell technology has been applied to the advanced flash memory and solid-state drive. By carefully control the tunneling current in the floating gate FET device, MLC has been realized. In the CBRAM, the controllable LRS is also observed by controlling the compliance current. This effect enables the MLC based on CBRAM devices.

5.1 Introduction

The R_{ON} and R_{OFF} statistics of $Cu/TaO_x/Pt$ devices have been shown in Chapter 2. The ON/OFF resistance ratio of CBRAM is usually higher than 10^3, allowing multilevel switching in a single memory cell to store more than one bit of data. Compared to CBRAM, the present STTRAM technology can only achieve the ON/OFF resistance ratio less than 10, which is too small to insert multiple distinct resistance levels. Therefore the multilevel cell capability is one of the advantages of CBRAM.

The multilevel cell of CBRAM is realized by the proper current control during SET process. When different levels of compliance current (I_{CC}) are applied to a

CBRAM device, a characteristic dependence of LRS resistance (R_{ON}) on I_{CC} is observed:

$$R_{ON} = \frac{K}{I_{CC}^{n}} \tag{5-1}$$

where K is a constant in units of volt, and n is a fitting parameter close to 1. This phenomenon is the foundation of MLC in CBRAM devices. The R_{ON}–I_{CC} relation in Eq. (5-1) is universally valid for numerous anode/electrolyte/cathode material systems [1]–[6]. Experimental results have shown that K depends on the materials, process, and structure of the device. The area of device under test is square and the size is 10 μm.

5.2 Physics of Multilevel Cell

The wide range of multilevel switching in CBRAM cell involves different physical mechanisms in the SET process. When the resistive device is in its HRS state, the gap between filament tip and the anode is large. Only small cation flux contributes to the

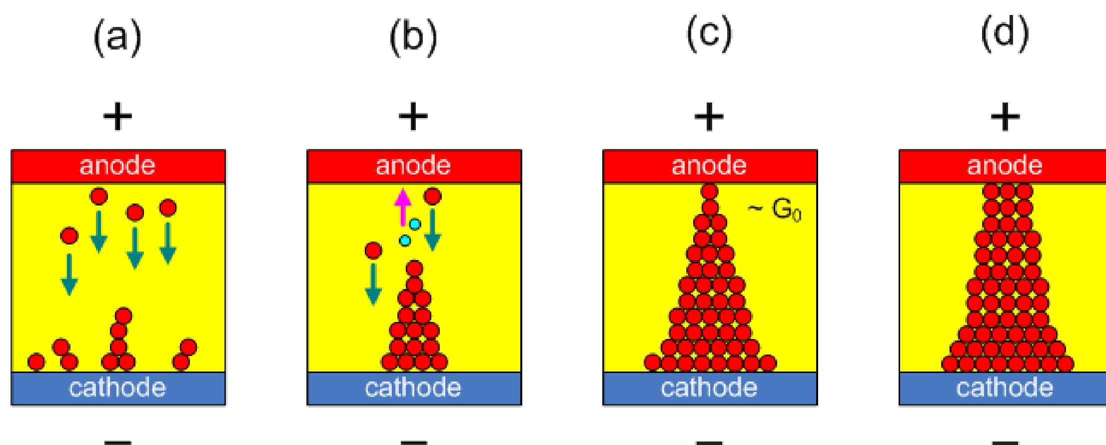

Fig. 5-1. Schematic illustration of physical mechanisms of SET process in a CBRAM cell. Red circles represents Cu atoms and cations. Blue circles represent electrons. The yellow rectangle represents the solid electrolyte. The "+" and "–" signs represent the voltage polarity relative to 0 V.

current as shown in Fig. 5-1(a). The transport of ions under the high electric field is described quantitatively by the hopping mechanism [7]. As the gap decreases, the electrons can tunnel through the oxide barrier. Thus the tunneling electron flux contributes to the current as well as cation flux, as shown in Fig. 5-1(b). When the gap is closed and the filament touches anode, metallic contact starts from just one single atom as shown in Fig. 5-1(c). The conductance of a single atom contact can be estimated from the one-dimensional charge transport [8]. After single atom contact, more and more atoms of the filament contact the anode and form new conduction channels. Finally the filament enters the radial growth regime and the resistance decreases [9]. All those processes can be regulated by the current compliance.

Menzel's tunneling model matches an impressive R_{ON}–I_{CC} range from 10^{11} Ω to 10^4 Ω [10]. The simulation strongly justifies the existence of electron tunneling current. Fig. 5-2 shows the transition details in terms of quantized conductance steps extracted

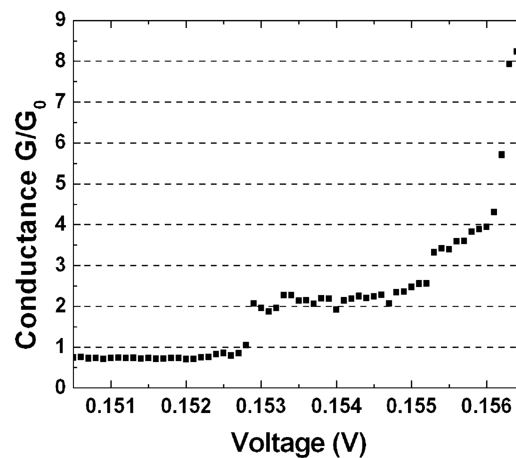

Fig. 5-2. Quantum conduction observed in I–V characteristic of Cu/TaO_x/Pt devices. The sweep rate ν is 0.002 V/s. $G_0 = 2e^2/h$, where e is the elementary charge and h is the Planck constant.

from I–V characteristics near $V_{SET} = 0.16$ V at the sweep rate of 2 mV/s. It can be seen that the conductance changes in quantum units of G_0 ($2e^2/h = 77.5$ μS, h being the Planck constant and e the elementary charge) from $1G_0$ to $2G_0$ and $4G_0$ reflecting the conductivity change due to electron tunneling from single atom to multiple single atoms during I–V sweeping [11]–[17]. After the voltage reaches 0.156 V (close to V_{SET}), the current increase is already too fast to show more distinct quantized conductance levels. The experiment is done at room temperature with the standard setup of I–V measurement. A very low voltage sweep rate is important for measuring the quantum conductance because the SET process can be monitored with high time resolution and the details of filament growth are revealed.

5.3 Voltage Constant in Multilevel Switching

The R_{ON}–I_{CC} relation reflects the final outcome of the abrupt current jump in the SET process. Remarkably, the R_{ON} dependence on I_{CC} in Eq. (5-1) spans two physical regimes based on different conduction mechanisms. When LRS is higher than 12.9 kΩ, the I–V dependence has been attributed to the non-ohmic conduction of direct tunneling of electrons through the gap between the growing filament and the electrode [10]. When the filament resistance is 12.9 kΩ ($= h/2e^2$), a single atom contact forms between the anode and the filament, and the metallic contact occurs for lower R_{ON} [11]–[17]. Below 12.9 kΩ, models have been proposed for R_{ON}–I_{CC} based on the ohmic conduction invoking radial growth of the nanofilament [9], [10]. Interestingly, experiments have shown the two mechanisms yield the same voltage constant K in the R_{ON}–I_{CC} relation, which means that K is independent of the fundamental mechanisms

of resistive switching and must have a more universal significance. In the previous research, the voltage constant K is usually treated as a fitting parameter without a clear physical meaning. In this section, the relation between K and the SET voltage is analyzed and verified with data obtained on $Cu/TaO_x/Pt$ devices.

Fig. 5-3 shows the I–V characteristics of a $Cu/TaO_x/Pt$ CBRAM device cell in quasi-static switching at three different voltage sweep rates ν spanning almost two orders of magnitude where the bias voltage is increased at a constant sweep rate. It can be seen that not only does the SET voltage decrease with decreasing ramp rate, but also the transition slope increases with decreasing ramp rate. When the applied voltage is less than V_{SET}, the current level remains low. At the time V_{SET} is reached, the current starts to increase abruptly to the current compliance level. In the transition region between low and high current, the voltage on the filament stays more or less constant

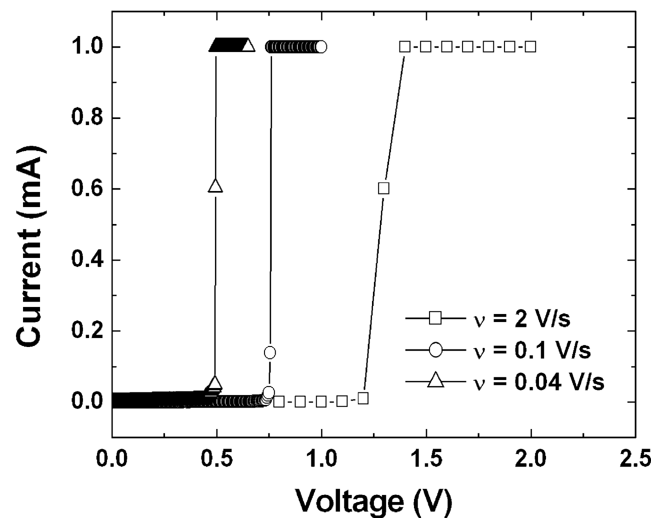

Fig. 5-3. I–V characteristics of a 10 μm ×10 μm $Cu/TaO_x/Pt$ resistive switching device. The voltage sweep rates ν are 0.04 V/s, 0.1 V/s and 2 V/s. The dimension of the measured device cell is 10 μm by 10 μm and the compliance current is 1 mA.

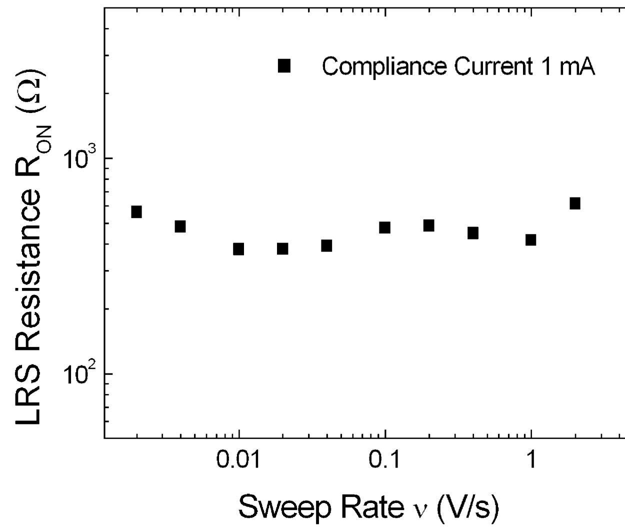

Fig. 5-4. LRS R_{ON} for different sweep rates. The current compliance is 1 mA.

at the relatively high SET voltage. It should be noted that because of the same I_{CC} level, R_{ON} is approximately constant independent of the sweep rate as shown in Fig. 5-4.

After the compliance current is reached, the voltage across the filament V_{CF} drops abruptly to a value significantly lower than V_{SET} and is determined by the final resistance of the cell R_{ON} as shown schematically in Fig. 5-5(a). This experimental observation implies that there is a minimum voltage $V = I_{CC}R_{ON}$ below which the

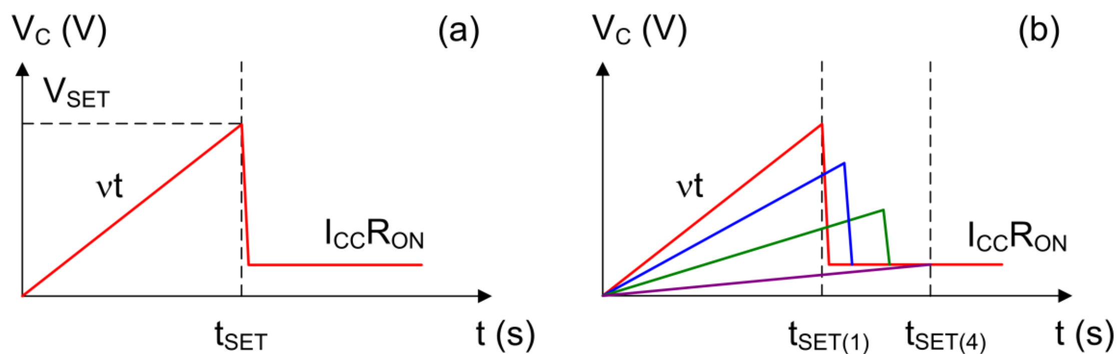

Fig. 5-5. Conceptual I–V and V–t characteristics. (a) Voltage drop on the device cell with time. (b) Cell voltages with different voltage sweep rates. V_C is the bias voltage on the device cell and R_{ON} is the final LRS resistance. ν is the voltage sweep rate and $V_{SET} = \nu t_{SET}$. Different SET times are labeled as $t_{SET(i)}$.

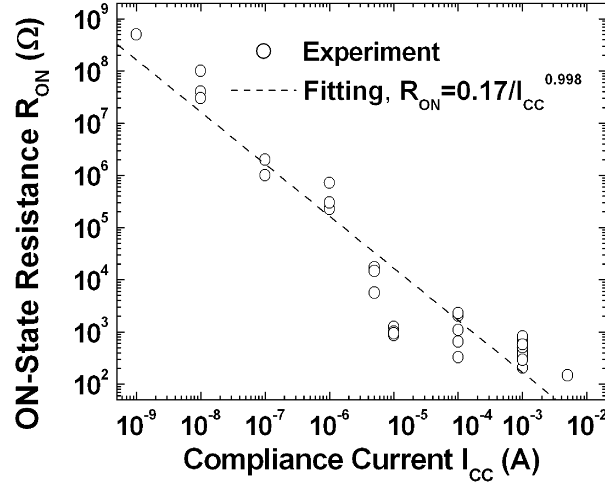

Fig. 5-6. Dependence of ON-state resistance on compliance current for $Cu/TaO_x/Pt$ devices. The dash line is the fitting curve for $R_{ON} = 0.17/I_{CC}^{0.998}$.

filament growth comes to a halt. This constant value of voltage may be extracted from the experimental R_{ON}–I_{CC} plot as shown in Fig. 5-6 for our $Cu/TaO_x/Pt$ devices.

The experimental data are fitted by $R_{ON} = 0.17/I_{CC}^{0.998}$. The fitting parameter n = 0.998 is very close to 1 and the voltage constant K is 0.17 V. In the transition regime from HRS to LRS, the Ohm's law can be expressed as

$$I_{CF}(t) = V_{CF}/R_{CF}(t) \approx V_{SET}/R_{CF}(t) \quad (5\text{-}2)$$

where the time dependence of current I_{CF} through the filament is mainly driven by the time dependence of the momentary filament resistance R_{CF}. At the end of the SET operation under the current compliance regime, the Ohm's law can be expressed as

$$V_{CF} = I_{CC}R_{ON} \quad (5\text{-}3)$$

where I_{CC} is the compliance current, and R_{ON} the final ON-state resistance depending on I_{CC}. In Fig. 5-5(b) it is schematically shown how the voltage across the device ends in the universal $I_{CC}R_{ON}$ voltage independent of the sweep rate applied as long as V_{SET}

has been reached. If the sweep rate keeps decreasing, the voltage drop at $t_{SET(i)}$ diminishes and eventually reaches the lower limit $V_{SET} = I_{CC}R_{ON}$. Hence, this particular V_{SET} equals K in Eq. (5-1) and can be identified with the minimum SET voltage $V_{SET(min)}$. $V_{SET(min)}$ is independent of the specific physical mechanisms. The physics of the constant K is that below $K = V_{SET(min)}$ the filament growth cannot be completed. This circumstance is universal to all $R_{ON} = K/I_{CC}$ relations in resistive switching cells reported in literature [3], [18].

For example, from R_{ON}–I_{CC} relation of $Ag/Ge_{0.3}Se_{0.7}/Pt$ resistive memory devices, the voltage constant is extracted as 0.08 V, which is very close to the SET voltage at the sweep rate of 0.01 V/s [2], [3]. In $Ag/GeS_2/W$ devices, the voltage constant and minimum SET voltage are both 0.2 V [1], [18]. Similar conclusions can be drawn from characterization of Cu/SiO_2-based resistive devices [19], [20].

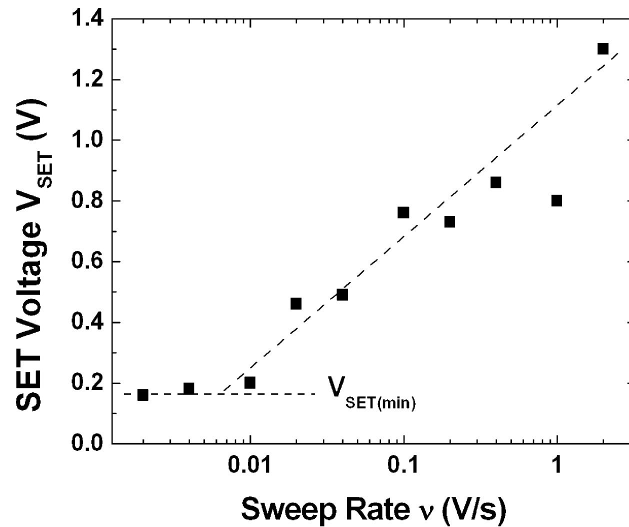

Fig. 5-7. Dependence of SET voltage on voltage sweep rate for the $Cu/TaO_x/Pt$ devices. The horizontal dash line is the saturated SET voltage which is 0.17 V. The inclined dash line is the fitting curve for the SET voltage at high sweep rates.

The same experiment method as in Ref. [19] has been applied to our $Cu/TaO_x/Pt$ devices. Fig. 5-7 shows the SET voltage dependence on the voltage sweep rate ν. When ν is from 0.01 V/s to 2 V/s, the SET voltage is almost proportional to the logarithmic of ν. When ν is less than 0.01 V/s, the SET voltage stays more or less constant. A minimum SET voltage is reached when the sweep rate is small enough. Comparing this minimum V_{SET} to the voltage constant in Fig. 5-6, we have K = $V_{SET(min)} = 0.17$ V.

In the current compliance (CC) regime, a small portion of the applied voltage drops across the filament. As R_{ON} keeps decreasing due to the filament radial growth, the voltage drop across the filament can be expressed as

$$V_{CF} = I_{CC} R^{*}_{ON} \tag{5-4}$$

where R^{*}_{ON} is the resistance caused by the assumed continuous R_{ON} reduction due to the radial growth, for example, or some other mechanism if present. Because of the gradual resistance drop under constant compliance current, $R^{*}_{ON} < R_{ON}$, then we obtain the inequality

$$V_{CF} = I_{CC} R^{*}_{ON} < I_{CC} R_{ON} = V_{SET(min)} \tag{5-5}$$

Because $V_{SET(min)}$ is the limiting SET voltage at small sweep rates, a voltage less than $V_{SET(min)}$ cannot cause resistive switching (growth of filament or nucleation of cations) even for reasonably long time intervals. Therefore, the R_{ON} stays constant in CC regime and $R^{*}_{ON} = R_{ON}$, $R_{ON} = V_{SET(min)}/I_{CC}$, and the resistance reduction comes to a halt. Because V_{SET} increases slowly with time even at small voltage sweep rate (Fig. 5-3), it will not stay constant for different I_{CC} levels. Therefore the R_{ON}–I_{CC} relation

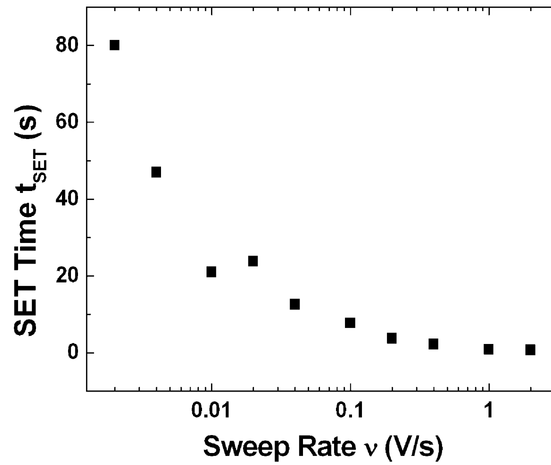

Fig. 5-8. Dependence of SET time on voltage sweep rate. t_{SET} is proportional to ln(ν)/ν and thus increases as ν decreases.

shows small nonlinearity (parameter n in Eq. (5-1)) in log scale as shown in Fig. 5-6. Nevertheless, the value of n is close to 1 which means that the transition from HRS to LRS is rather abrupt. For our Cu/TaO_x/Pt devices n is 0.998.

Fig. 5-8 shows the SET time as a function of the voltage sweep rate. While the SET voltage decreases with decreasing sweep rate, the SET time increases with decreasing sweep rate. This is explained by the dependence of t_{SET} as a function of the sweep rate ν: $t_{SET} = V_{SET}/\nu \sim \ln(\nu)/\nu$ [19]. The logarithmic increase of ν is weaker than the linear increase ν. When the SET voltage is low, the switching time is long enough to allow exploration of details of the SET transition near V_{SET}. Fig. 5-9 shows the I–V characteristics of device at low sweep rates. The device undergoes SET process but the current does not reach I_{CC} that has been set to 1 mA at the SET voltage. This is a common observation for the pinched hysteresis of a memristor. Once the lower resistance limit R_{min} is reached, the voltage drop on the filament cannot support further

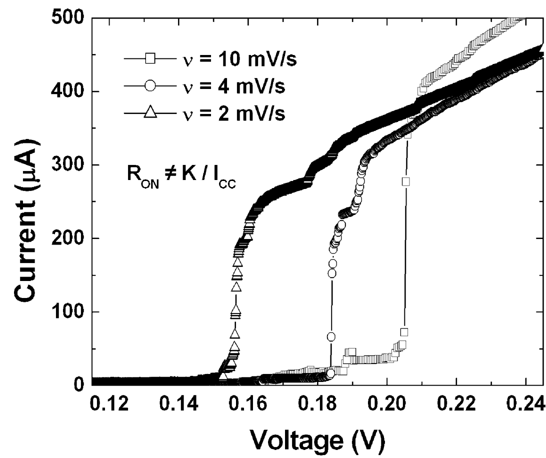

Fig. 5-9. I–V characteristics of Cu/TaO_x/Pt devices at low sweep rates. The compliance current is 1 mA. The device current does not reach the compliance current at the SET voltage.

decrease of R_{ON}. Here R_{min} includes the resistances of filament, electrodes, contacts, and interconnects. Fig. 5-10 shows R_{min} for different sweep rates. The resistances are measured in voltage sweeping mode without setting the current compliance. The data points scatters in a reasonably small range less than one order of magnitude. R_{min} with an average value of 400 Ω is independent of sweep rate ν. The limitation implies that

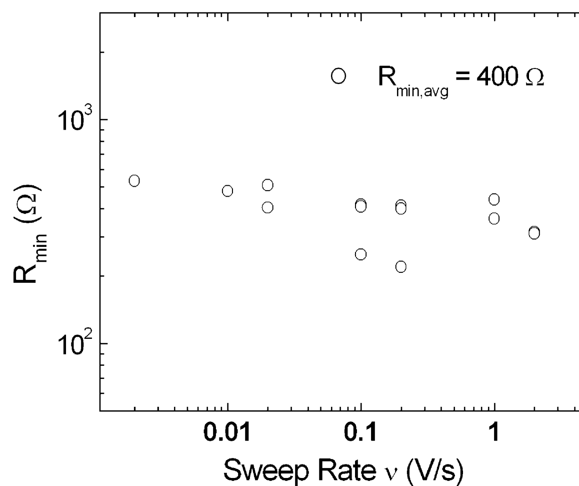

Fig. 5-10. LRS R_{min} for different sweep rates. The current compliance is not applied.

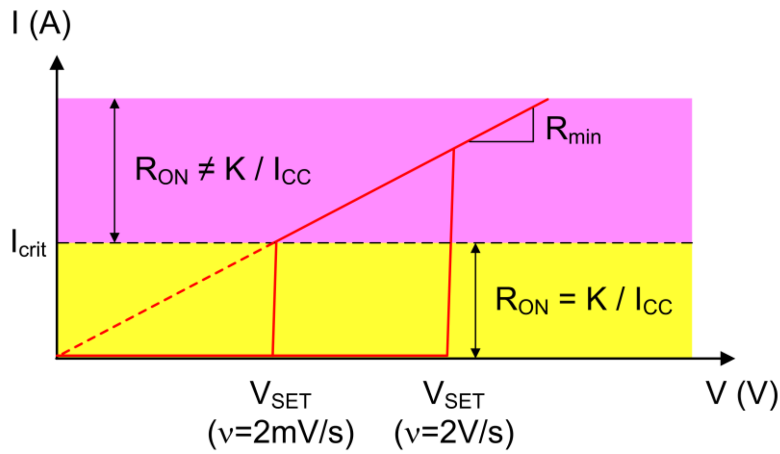

Fig. 5-11. Conceptual I–V characteristic of resistive devices. If there is no current compliance, the device ends in a constant resistance. The R_{ON}–I_{CC} relation is invalid if the compliance current is set in the region above the dashed line.

the R_{ON}–I_{CC} relation of Eq. (5-1) can be justified only for $I_{CC} < K/R_{min}$ and not for arbitrarily high I_{CC}. The measured lower bound of R_{ON} on our Cu/TaO_x/Pt devices is several hundred ohms. Therefore the device resistance saturates for the compliance current above 1 mA instead of following the K/I_{CC} behavior (Fig. 5-6). Fig. 5-11 shows the domain of validity for Eq. (5-1) in a schematic illustration of I–V characteristics for two extreme voltage sweep rates. The device resistance ends in a constant value beyond V_{SET} and I–V exhibits linear dependence. V_{SET} at a very low sweep rate is equal to the voltage constant K. A critical current $I_{crit} = K/R_{min}$ is the boundary between the validity and invalidity of Eq. (5-1). If the compliance current is set higher than I_{crit} (in the upper shaded region of Fig. 5-11), the $R_{ON} = K/I_{CC}$ relation no longer holds. The practical impact for the switching behavior is that $R_{ON} = \text{const} = R_{min}$ for all $I_{CC} > I_{crit}$. In our devices $I_{crit} \approx 300$ μA.

5.4 Radial Growth Model for Conical Filament

According to the SET process described in Fig. 5-1, Menzel et al. have proposed a simulation model for the multilevel switching of CBRAM in the low compliance current regime [10]. The I–V dependence has been attributed to the non-ohmic conduction of direct tunneling of electrons through the gap between the growing filament and the electrode. On the other hand, there are $R_{ON}(I_{CC})$ models proposed based on ohmic conduction invoking radial growth of the nanofilament assumed to be of cylindrical geometry [21]–[23]. For high compliance current, a metallic contact is formed and therefore the R_{ON} is determined by the radial growth of the filament. Truncated cone has also been considered as an alternative shape of the conductive filament in the resistive switching devices [24]–[28]. In Ref. [29] a transmission electron microscopy image shows a conductive filament in Al/Cu/$GeSe_x$/TaO_x/W devices to be of a truncated cone shape with top and bottom diameters of 17 nm and 24 nm, respectively. In this section, we present a model for the radial growth of a truncated cone-shaped Cu conductive filament and verify it on data obtained for Cu/TaO_x/Pt devices of 32 nm TaO_x thickness. Process and electrical characterization of these devices have been reported in detail in Chapter 2.

Usually, the forming or SET operation of a resistive device is shown as a structureless vertical jump of current at a sharp voltage value V_{SET} during a voltage sweep [30]–[33]. However, the seemingly quantum-like transition follows an evolution characteristic shown in Fig. 5-12 on a finer time scale. Here, current is plotted on a logarithmic scale with high time resolution of a voltage step of 1 mV and time interval

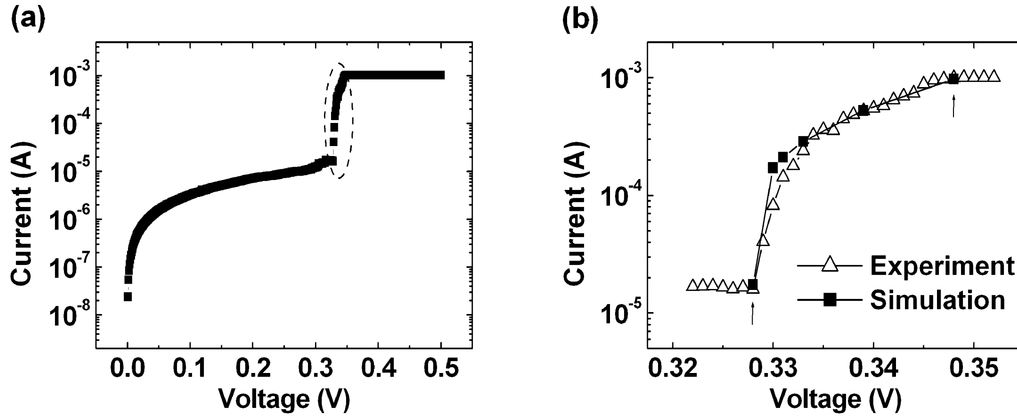

Fig. 5-12. (a) I–V characteristic of a 10 μm ×10 μm Cu/TaO_x/Pt resistive switching device. The voltage sweep rate is 0.02 V/s. (b) Experimental and simulated I–V characteristics of the resistance state transition. The quasi-static voltage sweep is applied on the Cu/TaO_x/Pt device. The time interval between two experimental data points is 50 ms and the voltage step is 1 mV.

between two data points of 50 ms. As the bias voltage sweeps from 0 to 0.2 V, the device current increases slowly from 0 to about 10 μA. At 0.328 V, the current increases from 15 μA to 1 mA within a voltage interval of 0.03 V, as shown in Fig. 5-12(a). This transition is further enlarged in Fig. 5-12(b) and compared to our model predictions. One can see from both figures that there is a characteristic inflection point at about 15 μA and V = 0.328 V (R = 21.9 kΩ) indicated by the lower arrow shown in Fig. 5-12(b). This inflection point separates two physical regimes of non-ohmic and ohmic behavior. As it will be shown in the following, the ohmic behavior can be described by dynamics of radial growth model, whereas the non-ohmic part may be explained by models such as proposed by Menzel et al [10]. Here we concentrate on the physics of the ohmic transition between the two arrows in Fig. 5-12(b). It should be stressed that Fig. 5-12 is a typical result of time resolved characteristics of a HRS-to-LRS transition. In this particular case, the compliance current I_{CC} = 1 mA and

the time between the two arrows in Fig. 5-12(b) is about 1 s. Similar results have been observed for lower I_{CC} values at a reduced transition time. For example, for I_{CC} = 50 μA one obtains a corresponding ohmic transition time within 100 ms. The ohmic regime begins when a metallic contact is established between the growing nanofilament and the Cu electrode. It is assumed that the metallic contact is established when one Cu atom connects the filament to the Cu electrode. The minimum diameter of the contact area is thus dictated to be about 3 Å, the size of a Cu atom, whereas the remainder of the existing portion of the filament has larger cross-sections. A simple model to describe such situation is truncated cone geometry of the Cu filament (Fig. 5-13(a)). At a specific time t, counted from the moment the current exceeded the inflection point of 15 μA, the ON-state resistance R_{ON} of the filament is calculated according to

$$R_{ON}(t) = \frac{\rho L}{\pi r(t) R(t)} \qquad (5\text{-}6)$$

where ρ is the electrical resistivity, L is the length of the filament, r(t) and R(t) are the radii of filament top and bottom of the truncated cone. At the inflection point $R_{ON}(I = 15\ \mu A)$= 21.9 kΩ. Since the quantum resistance of a single Cu atom at the contact is $R_K = h/2e^2 = 12.9$ kΩ, the residual resistance of 9 kΩ is consistent with Eq. (5-1) for the remaining partial ohmic filament. To set up a dynamical growth equation for r(t) and R(t) we need to calculate the local transport of Cu ions as a function of position of the surface of the nanofilament. The transport of Cu cations in CBRAM devices can be described by the hopping mechanism modeling the enhanced ion diffusion in oxide

under the high electric field [1], [7], [9]. The Cu^+ ion flux F in the solid electrolyte is driven by the local electric field and can be expressed as

$$F = 2N_i af \exp\left(-\frac{E_a}{kT}\right)\sinh\left(a\frac{qE}{2kT}\right) \tag{5-7}$$

where E_a is the activation energy, k the Boltzmann constant, T the temperature in the unit of K, E the electric field, *a* the distance of a single hopping step, N_i is the cation concentration in the solid electrolyte, f is the attempt frequency, and q is the charge of a cation. In order to use this transport mechanism for the growth of the truncated cone the local electric field on the CF surface has to be determined. As the filament grows, the local electric field will change substantially due to the change in resistance and hence in the resulting local voltage drop.

Fig. 5-13(a) shows the geometry and voltage distribution of the conical filament. In the figure, the length of the filament is L, the top radius is r, the bottom radius is R, the

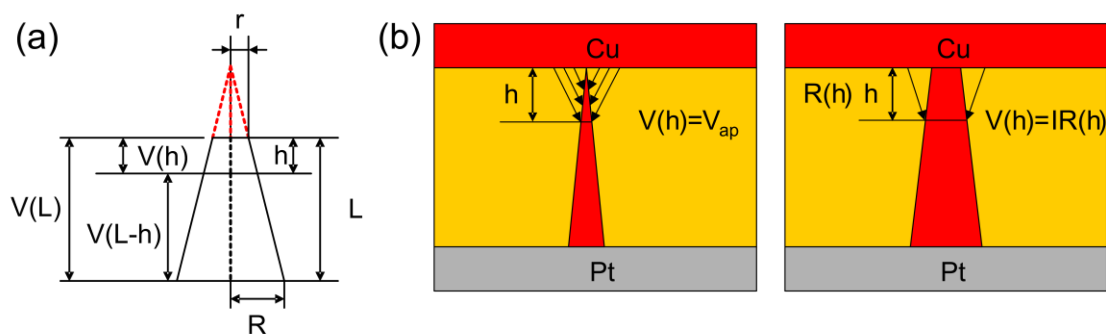

Fig. 5-13. (a) Geometry of the truncated conical filament. The electric field depends on the position h away from the filament tip. L is the length of the filament, h is the height of the top part, r and R are the radii of filament top and bottom respectively. V(L) is the voltage drop on the filament. V(L) and V(L–h) are voltages drop on the top and bottom parts (V(L)=V(h)+V(L–h)). (b) Conceptual view of the metallic contact, radial growth of filament, and the local electric field in the Cu/TaO_x/Pt CBRAM device. V(h) and R(h) are voltage drop and resistance of the top part filament, respectively. V_{ap} is the voltage between Cu and Pt electrode and I is the current. The arrow lines represent the electric field. The denser the arrow lines, the higher the local electric field.

height of the top part is h, the voltage on the filament is V(L), and the voltages on the top and bottom parts are V(h) and V(L–h). h denotes the variable of the local electric field of interest. For a truncated conical metallic filament, the resistance of the filament tip is larger than the resistance of the broad base. When the top radius is very small, almost all of the total filament resistance is concentrated in the tip. This means the voltage drop V(h) on top part of the filament is higher than the voltage drop V(L–h) on the bottom part of the filament. As a result, the electric field around the top of filament is much higher than that at the bottom when the filament is initially established (see Fig. 5-13(b)). The local electric field depends not only on the bias voltage but also on the radii of filament and the position along the filament. The resistance of the top and bottom part of the filament is calculated with Eq. (5-6):

$$\frac{R_{top}(t)}{R_{tot}(t)} = \frac{R(t)h}{r(t)L + (R(t) - r(t))h} \tag{5-8}$$

$$\frac{R_{bot}(t)}{R_{tot}(t)} = \frac{r(t)(L - h)}{r(t)L + (R(t) - r(t))h} \tag{5-9}$$

where R_{top}, R_{bot}, and R_{tot} are the resistance of top part, bottom part, and the complete filament, respectively. Before the compliance current is reached during the SET process, the voltage drop on the filament is the relatively high SET voltage. When the compliance is reached, the voltage on the filament is small and the effective electric field is small. Therefore the ion flux is suppressed and the radial growth comes to a halt. According to Eq. (5-8), the voltage distribution along the axial direction of filament can be calculated. Assuming V = 0 V at CF bottom (h = L) and V = V(t) at CF top (h = 0), V(h, t) is a function of position h from the top:

$$V(h,t) = V(t) - V(t)\frac{R_{top}(t)}{R_{tot}(t)} = \frac{V(t)r(t)(L-h)}{r(t)L + (R(t) - r(t))h} \tag{5-10}$$

For example, let V(t) = 0.3 V, R(t) = 6 nm, r(t) = 1.2 nm, L = 32 nm, then the voltage distribution V(h, t) is plotted in Fig. 5-14. The slopes of the red and blue lines represent the average electric field across the corresponding distance. It is easy to see that the real electric field (dV/dh) is close to the average electric field V_{top}/h at the top of the filament (red line for 0 < h < 5 nm), whereas dV/dh is close to V_{bot}/h at the bottom of the filament (blue line for 20 nm < h < 32 nm). Therefore the electric field can be approximately expressed by the ratio of voltage drop and distance instead of the derivative in order to simplify the simulation model. Based on Eqs. (5-8) and (5-9), we can derive the average electric field for the top part and the bottom part:

$$E_{top}(h) = \frac{V(t)}{h}\frac{R_{top}(t)}{R_{tot}(t)} = \frac{V(t)R(t)}{r(t)L + (R(t) - r(t))h} \tag{5-11}$$

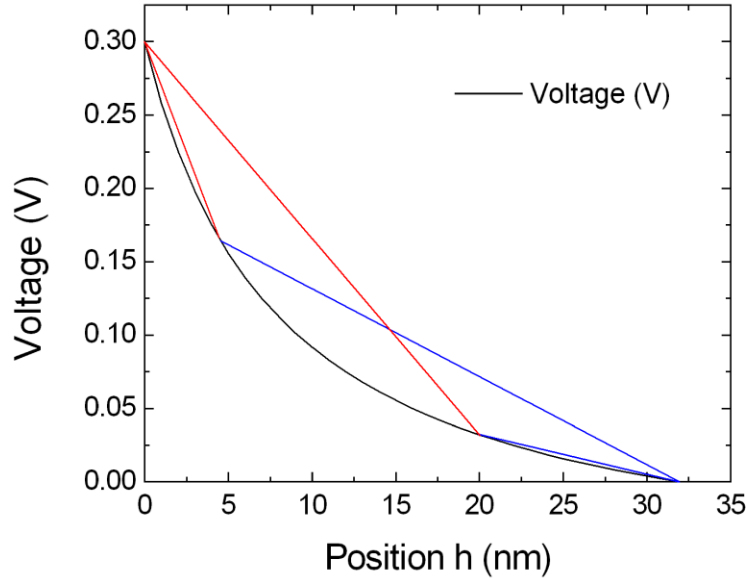

Fig. 5-14. Voltage distribution along the axial direction of filament. The slopes of red and blue lines represent the approximate electric field at the top and bottom of the filament.

$$E_{bot}(h) = \frac{V(t)}{L-h}\frac{R_{bot}(t)}{R_{tot}(t)} = \frac{V(t)r(t)}{r(t)L + (R(t)-r(t))h} \tag{5-12}$$

where V(t) is the total external bias voltage across the filament. Due to the nonlinear distribution of the local resistance and voltage, the average electric field in the top part of filament is higher than the bottom part of filament. Thus depending on the position of interest, either Eq. (5-11) or Eq. (5-12) should be used to compute the approximate electric field.

According to Eqs. (5-11) and (5-12), the electric field at the position h on the top part of the filament is proportional to the filament bottom radius, whereas the electric field at the position H at the bottom part of the filament is proportional to the filament top radius. The geometrical form factors are defined as the ratio of local electric field E and average electric field V(t)/L, which represent the electric field non-uniformity caused by the filament geometry. The equations are derived for the filament top and bottom as:

$$g(h,t) = \frac{R(t)L}{r(t)L + (R(t)-r(t))h} \tag{5-13}$$

$$E(h,t) = \frac{V(t)}{L} g(h,t) \tag{5-14}$$

$$G(H,t) = \frac{r(t)L}{r(t)L + (R(t)-r(t))H} \tag{5-15}$$

$$E(H,t) = \frac{V(t)}{L} G(H,t) \tag{5-16}$$

where g and G are the geometrical form factors for filament top and bottom, and E is the approximate local electric field. In an extreme case, we consider the two terminals of the conductive filament, i.e. h = 0 and H = L. The Cu nanobridge is a cone in the simulation so that only the radius evolution on the top and bottom is important.

The electrochemical deposition of cations increases the filament radius. According to Faraday's law, the radial growth rate of filament is proportional to the cation flux. Since a conical filament is being considered, the electric field distributes differently at the top and bottom of the cone, which is accounted for by the geometrical form factors g and G. By combining Eq. (5-6) and Eqs. (5-13) to (5-16), we have

$$\frac{dr(t)}{dt} = v_r \exp\left(-\frac{E_a}{kT}\right)\sinh\left(\beta g \frac{a}{L}\frac{qV(t)}{kT}\right) \tag{5-17}$$

$$\frac{dR(t)}{dt} = v_r \exp\left(-\frac{E_a}{kT}\right)\sinh\left(\beta G \frac{a}{L}\frac{qV(t)}{kT}\right) \tag{5-18}$$

where v_r is the prefactor of the Arrhenius equation of growth rate, β is a fitting parameter for the temperature increase due to Joule heating and the nonlinearity of local electric field caused by the curvature of the filament.

Fig. 5-13(b) shows the schematic view of the radial growth process in a Cu/TaO_x/Pt CBRAM device. When the filament forms a point contact with the Cu electrode, the filament resistance is infinite neglecting the quantum effect. The voltage drops completely on the filament tip and creates extremely high electric field. In the following very short time interval, the radius of the filament tip quickly increases. An extremely high rate is expected for the beginning of filament growth, and it decreases as the top radius increases. The geometrical change results in voltage redistribution and thus the electric field at the tip decreases. Once the filament resistance is low enough, the current reaches the compliance and the radial filament growth is completed.

Table 5-1 shows the values of parameters used in the numerical computation to fit the experimental data. As mentioned before r_0 was assumed to be one atom size, i.e. 2 Å. ρ is extracted from experimental data to be 3300 Ω-nm which is within the range but at lower bound of data reported in the literature [1], [29]. From these data and the resistance measured at the inflection point in Fig. 1(a), the initial bottom radius is determined to be 6 nm. The bias voltage is expressed as

$$V(t) = V_0 + k_S t \tag{5-19}$$

where V_0 is the voltage at the inflection point (t = 0) and k_S (= 0.02V/s) is the experimental voltage sweep rate. Eqs. (5-17) and (5-18) are solved then simultaneously with $t = 0$ marking the inflection point. R_{ON} is calculated according to Eq. (5-6) and the I–V characteristic is derived from Ohm's law (Eq. (5-20)) shown as the filled squares in Fig. 5-12(b).

$$I(t) = V(t) / R_{ON}(t) \tag{5-20}$$

The growth end time is determined when the current through the cell would exceed I_{CC}, when the actual voltage drop over the device decreases stopping the lateral growth of the filament rendering ultimate filament resistance is more or less fixed. In Eqs. (5-17) and (5-18) it is important that the sinh term be not replaced by an exp term as often done in applications of the Butler-Volmer equation [9], [34]. Our simulations show that sinh term provides more physical description of the radial growth. The reason is that for small fields the sinh term stops the radial growth whereas exp term keeps the growth rate finite. The sinh term explains in a natural way why the radial

growth comes essentially to zero and the R_{ON} remains more or less constant after the current has reached the set I_{CC} value.

Table 5-1 Values of parameters in the radial filament growth model.

Parameter	Numerical Value	Parameter	Numerical Value
v_r	8 cm/s	a	1 nm
E_a	0.4 eV	ρ	3300 Ω-nm
kT	0.026 eV	β	0.8
r_0	0.2 nm	L	32 nm
R_0	6 nm	k_S	0.02 V/s

The results of model calculations are summarized as follows: Fig. 5-15(a) shows the simulated top and bottom radii and growth rate of the Cu filament according to Eqs. (5-17) and (5-18). At the beginning the growth rate is much higher at the tip of the filament than at its bottom and decreases then quickly to a constant value which is the upper asymptote for the growth of the bottom radius. As a result, the difference between the radii of top and bottom reduces as the filament grows. By the end of growth, the top and bottom radii increase at almost the same rate. Fig. 5-15(b) shows that over time the top and bottom radii converge to a similar value driving the shape of nanofilament from truncated cone geometry to that of a cylinder. Our model suggests that the shape of the nanofilament will resemble truncated cone for low I_{CC} and a cylinder at high I_{CC}. Direct observations by TEM have confirmed the cylindrical metal filament for compliance currents in excess of 1 mA [35], [36].

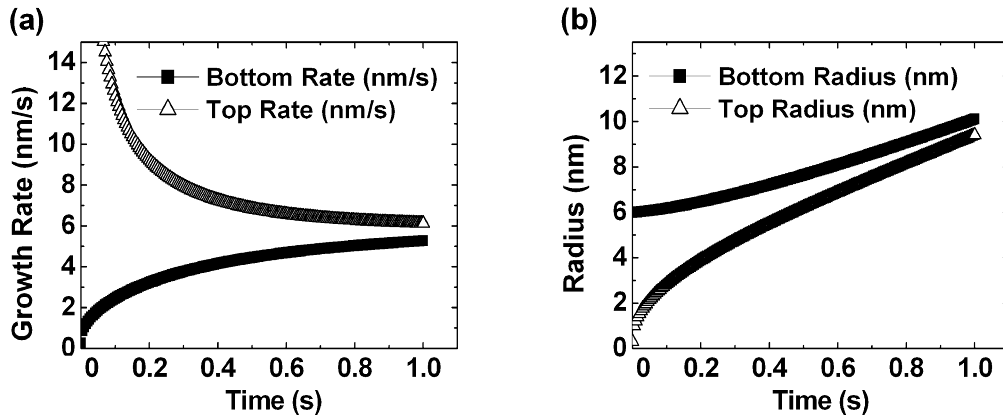

Fig. 5-15. (a) Simulated growth rates of the top and bottom of filament. The initial growth rate of filament tip is extremely high whereas the growth rate of filament base is close to zero. At the end of radial growth, the two growth rates stabilize and converge. (b) Simulated radii of the top and bottom of filament. The final radii of filament tip and base are close rendering a more cylindrical geometry.

In Fig. 5-12(b), the simulated I–V characteristic in the transition region between HRS and LRS shows a surprisingly good agreement with the experimental data within 10% error. The corresponding resistance as a function of time is shown in Fig. 5-16(a) with an excellent agreement between simulation and experiment. The resulting dependence of resistance on the current is shown in Fig. 5-16(b).

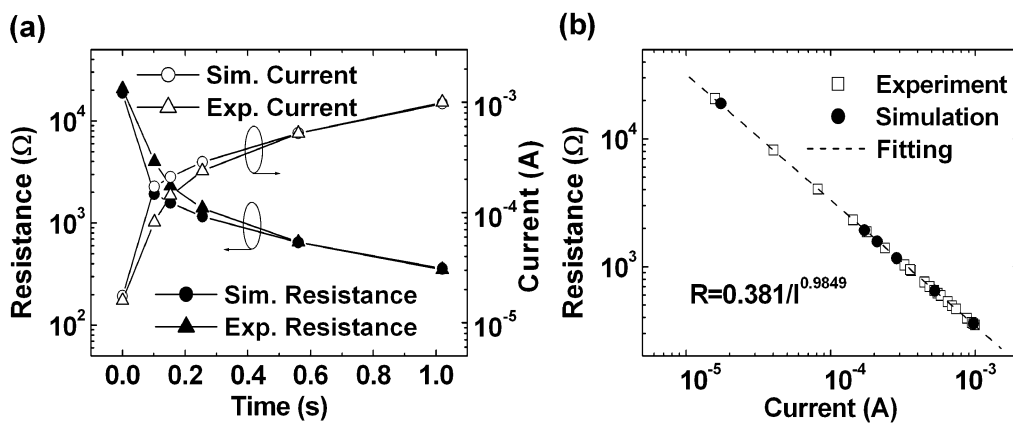

Fig. 5-16. (a) Dependency of device resistance and current on radial growth time. The time of 0 s is recorded when the HRS to LRS transition starts (current higher than 15 μA in Fig. 1). (b) Experimental and simulated resistance-current relation in the transition region between HRS and LRS.

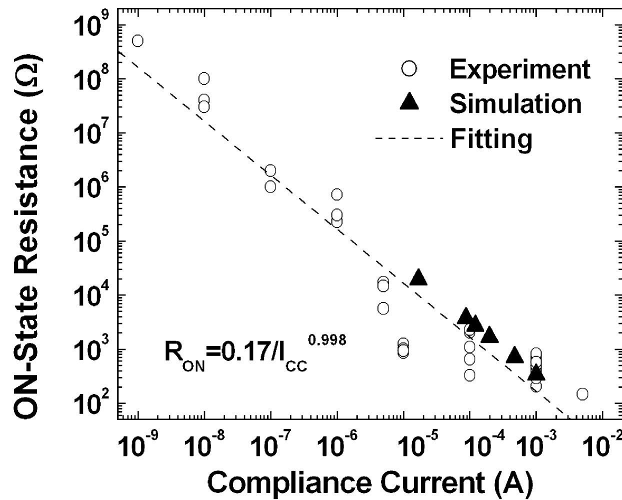

Fig. 5-17. Experimental and simulated multilevel switching property of $Cu/TaO_x/Pt$ devices. The ON-state resistance R_{ON} is inversely proportional to the compliance current I_{CC}.

Fig. 5-17 shows the multilevel switching property measured on multiple $Cu/TaO_x/Pt$ CBRAM devices. The simulated ON-state resistance is compared with the experimental data. The experimental data are fitted by $R_{ON} = 0.17/I_{CC}^{0.998}$. The simulated results match accurately the resistance data with I_{CC} from 10 μA to 1 mA. The corresponding resistance range is 20 kΩ to 200 Ω. For higher R_{ON}, the metallic contact is not yet formed and the electron tunneling may be the major contribution to the current [10]. The consistence of the experimental and simulated multilevel switching implies that the radial filament growth causes the resistance reduction in the high current regime, and the driving force of growth is the hopping and electrochemical deposition of Cu ions at high electric fields.

At the boundary between transition regime and current compliance regime, the SET current I_{SET} increases to I_{CC}, and I–V complies with Ohm's law. For example, I_{CC} = 1 mA and V_{SET} = 1 V, then the resistance at the boundary is 1 kΩ. Note that the

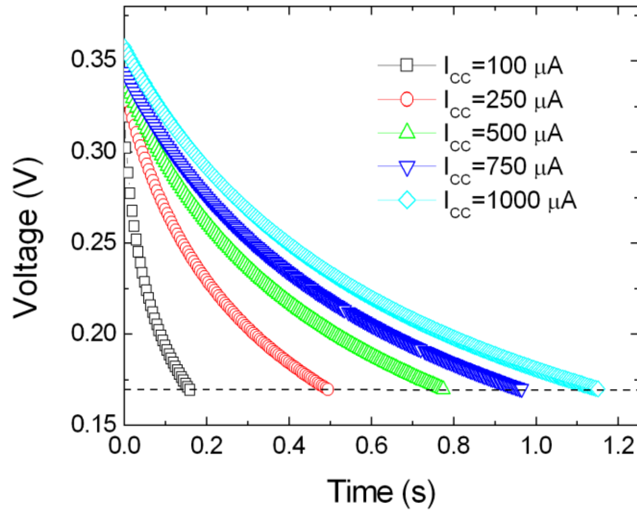

Fig. 5-18. Simulation of CF voltage decrease with time due to the continuous radial growth in the current compliance regime. The voltage decreases until the voltage constant K is reached.

voltage drop on the CF at the boundary is 1 V which still induces high electric field and the Cu^+ cation flux. At the time reaching the boundary, the voltage is the highest in the transition region and the electric field is the strongest. As a result, the CF keeps growing, but the current is fixed, so the voltage drop on the CF decreases and the voltage drop on the external circuit increases. As the resistance decreases to a certain value, the voltage drop on CF is small compared to an overpotential value, or the shape of the filament is more cylinder-like and the radial electric field is too small to provide sufficient Cu flux. Consequently, the CF stops radial growing and the final resistance stabilizes. Experiments in Section 5.3 have shown the threshold is the voltage constant K. Based on Eqs. (5-17) and (5-18) and Table 5-1, the decay time can be estimated for the current compliance regime. The instant voltage drop on the filament is the product of CF resistance and compliance current:

$$V(t) = I_{CC} R_{ON}(t) \tag{5-21}$$

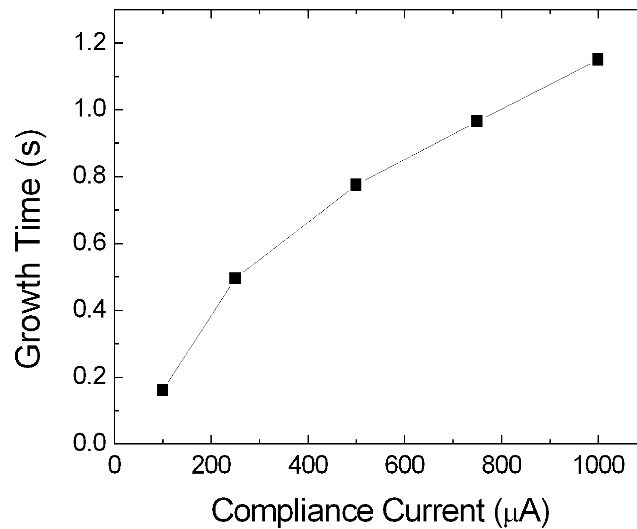

Fig. 5-19. Continuous radial growth time for different compliance current level.

Fig. 5-18 shows the voltage decrease with time in the current compliance regime (I_{CC} = 1 mA). The starting top and bottom radii, current, and voltage are derived from the end of radial growth in the transition regime. The end of transition regime, i.e. the beginning of current compliance regime, is labeled as 0 s in the continuous growth simulation. When different compliance current is selected, the decay time varies. Fig. 5-19 shows the dependence of decay time on compliance current. A higher compliance current requires longer time for the device voltage to decay to the final constant value K.

5.5 Temperature Effect

In Section 5.4, the temperature effect is included in the fitting parameter β. In a more realistic model, a lumped thermal resistance can be used to account for the heat dissipation in CBRAM cells:

$$T = T_0 + P \cdot R_{th} = T_0 + \frac{V^2}{R_{ON}} R_{th} = T_0 + I^2 R_{ON} R_{th} \tag{5-22}$$

In this temperature model, the equilibrium state is assumed so that there is enough time for the temperature to stabilize for a given instant power consumption P. A constant R_{th} is estimated to be $6\times10^4 \sim 10^5$ K/W for CBRAM devices [2], [37]. For a cylindrical conductive filament, the ratio between R_{th} and R_{ON} is a constant determined by the electrical resistivity ρ and thermal conductivity k_{th} [38], [39]:

$$\frac{R_{th}}{R_{ON}} = \frac{1}{8\rho k_{th}} \tag{5-23}$$

For bulk metals, the heat spread is based on the charge carrier, i.e. electrons. Therefore Wiedemann-Franz law validates at room temperature and we have

$$\frac{R_{th}}{R_{ON}} = \frac{1}{8\rho k_{th}} = \frac{1}{8LT} \tag{5-24}$$

where L is Lorenz number and T the temperature. Combining Eqs. (5-22) and (5-24), an equation about temperature T is derived:

$$T = T_0 + \frac{V^2}{R_{ON}} R_{th} = T_0 + \frac{V^2}{8LT} \tag{5-25}$$

Thus the temperature T can be obtained from Eq. (5-25), which is irrelevant to the thermal conductivity and resistivity:

$$T = \frac{1}{2}\left(T_0 + \sqrt{T_0^2 + \frac{V^2}{2L}} \right) \tag{5-26}$$

However, the properties of bulk materials may not hold for our resistive devices where a Cu nanofilament is embedded in an oxide matrix. The experimentally extracted ρk_{th} product has implied that the phonons could play an important role in the heat transfer in resistive devices [38], [39]. In this research, the minimum effective

thermal conductivity is k_{th} of the TaO_x matrix, and the experimentally extracted Cu CF resistivity is much higher than that of bulk Cu. Therefore, the Wiedemann-Franz law may not be valid for the Cu filament in CBRAM devices. The effective k_{th} can be estimated by the summation of k_{th} of the phonons in the oxide matrix and k_{th} of the electrons based on Wiedemann-Franz law:

$$k_{th} = k_{th,ph} + k_{th,el} = k_{th,ph} + \frac{LT}{\rho} \tag{5-27}$$

where $k_{th,ph}$ is the Ta_2O_5 thermal conductivity (33 W/(Ω·m) [40]), and ρ the fitted electrical conductivity of Cu filament (200~330 μΩ-cm [1], [29]). Based on the temperature model (Eqs. (5-22)~(5-27)), Eqs. (5-17)~(5-18) are solved again and compared to the experimental data. Since the thermal model is added in the radial growth model, the value of fitting parameter β is set to 1. Fig. 5-20 shows the simulated I–V characteristics based on the thermal model. The temperature increase

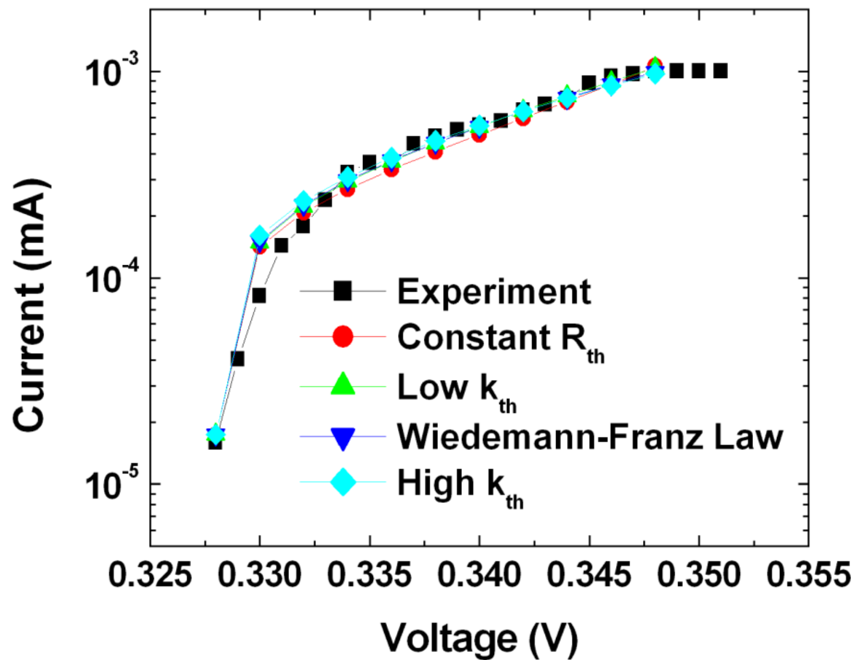

Fig. 5-20. Simulated I–V characteristics with different thermal models.

results in more realistic fitting parameters, i.e. smaller hopping distance *a* and growth rate prefactor v_r. The fitting parameters are summarized in Table 5-2 and other parameters are the same as those in Table 5-1. By comparing the physics of four thermal models, it is concluded that the ρk_{th} model with k_{th} = 35 W/(Ω·m) is more reasonable for the simulation of CBRAM devices.

Table 5-2 Parameters in simulation models considering thermal effect.

Parameter	R_{th} model, Constant R_{th}	ρk_{th} model, low k_{th}	Wiedemann-Franz Law	ρk_{th} model, high k_{th}
a (nm)	0.55	0.3	0.5	0.5
v_r (cm/s)	8	0.38	0.00125	8
R_{th} (K/W)	6×10^4	–	–	–
k_{th} (W/(Ω·m))	–	35	–	401
β	1	1	1	1

5.6 Summary

The universal physics behind the $R_{ON} = K/I_{CC}$ relation has been identified for all resistive switching devices based on filamentary conduction mechanism. The constant K corresponds to the minimum value of the SET voltage. The limiting SET voltage can be extracted by choosing a small sweep rate in the I–V characteristic measurement. Below the saturated V_{SET}, the device cannot be switched ON in a reasonably long time. Experimentally extracted voltage constant matches well with the saturated SET voltage of Cu/TaO_x/Pt devices. The transition between tunneling and ohmic regime of conduction is characterized by quantized conductance transitions

that can be readily observed at room temperature with sufficiently small voltage sweep rates.

A phenomenological model has been developed for the radial growth of a truncated conical shape metallic filament in CBRAM devices. The model describes only a part of the $R_{ON}(I_{CC})$ curve attributed to ohmic resistance decrease for sufficiently high I_{CC}. For our devices the regime of validity is $I_{CC} > 15$ μA. Below this value, the R_{ON} dynamics is ruled by non-ohmic conduction mechanisms such as electron tunneling [10]. The model is able to describe with great accuracy the dynamic details of the transition. In reality, the filament geometry is hardly a perfect cone. However, as long as the cross-section areas are similar for real filament and conical filament, their resistance can be calculated accurately with the radial growth model applied to the cone-shape geometry.

Chapter 6 Simulation of CBRAM Switching

This chapter describes the modeling of SET/RESET processes for CBRAM. The electroforming and SET voltages depends on the gap between the cathode (Pt or filament tip) and anode (Cu) [1], [2]. The continuum approach is used to model a switching cycle, including ion migration, filament growth and rupture. The governing partial differential equation system consists of drift-diffusion equation under high electric field, Poisson's equation, Faraday's law of electrolysis, heat equation, and moving boundary. The simulation provides an in-depth understanding of the resistive switching mechanism and a method for device structure design.

6.1 Introduction

Various mechanisms have been proposed to explain the behaviors of resistive switching (RS) [3]. The formation and rupture of a conductive filament has been widely recognized as the core concept of resistive switching [4]. However, a comprehensive model is still missing for the resistive memory. In this chapter, a phenomenological model is proposed for the forming/SET process of CBRAM, which captures three physical mechanisms: transport of Cu ions, potential redistribution in the electrolyte, and growth of the conductive filament in presence of a moving boundary. The predicted temperature, thickness, sweep rate, and trap density dependence of the forming voltage are verified with the data obtained on Cu/TaO_x/Cu resistive switches.

The electrochemical dissolution is usually used to explain the RESET process of CBRAM. However, the high RESET current observed for Cu/TaO_x/Pt CBRAM devices implies non-negligible local heating effect. In this chapter, the thermal effect is evaluated as the major contribution to the RESET process. Computational models are established to evaluate the Joule heating and Thomson effect which could possibly coexist during the rupture of a conical conductive filament.

6.2 Rate-Limiting Process in Resistive Switching

The CBRAM devices consist of two interfaces: anode/electrolyte interface (Cu/TaO_x) and cathode/electrolyte interface (Pt/TaO_x). The filament grows by migration of cations (Cu^{z+}, z is the charge state of cation) from the anode/electrolyte interface to the cathode/electrolyte interface. In the resistive switching, the oxidation reaction takes place at the anode/electrolyte interface such as

$$Cu \rightarrow Cu^{z+} + ze^- \quad (6\text{-}1)$$

while the reduction reaction takes place at the cathode/electrolyte interface such as

$$Cu^{z+} + ze^- \rightarrow Cu \quad (6\text{-}2)$$

An illustration of the one-dimensional CBRAM structure is shown in Fig. 6-1. Three fluxes appear in the MIM stack: (1) the oxidation flux at the anode/electrolyte interface (Cu/TaO_x), (2) the cation transport flux in the electrolyte (TaO_x), and (3) the reduction flux at the cathode/electrolyte interface (Pt/TaO_x). The filament growth rate is proportional to the reduction flux according to Faraday's law. The transport of cations consists of a drift flux driven by the electric field and a diffusion flux driven by the concentration gradient of ions. The equations of three fluxes are

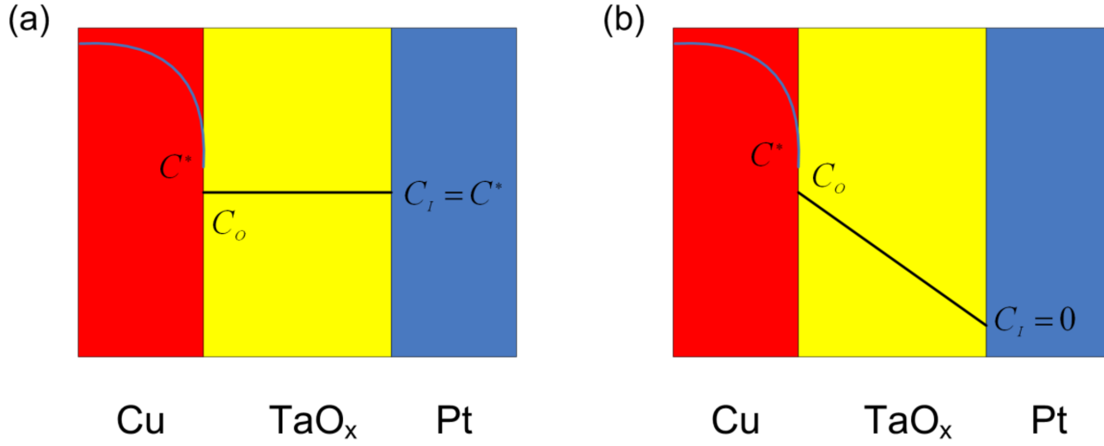

Fig. 6-1. Cation concentration in CBRAM devices in two extreme cases: (a) Uniform distribution when reduction reaction is the rate-limiting process. (b) $C_I = 0$ when transport is the rate-limiting process.

$$F_1 = h\left(C^* - C_O\right) \tag{6-3}$$

$$F_2 = -D\cosh\left(\frac{zqaE}{2kT}\right)\frac{\partial C}{\partial x} + \frac{2}{a}D\sinh\left(\frac{zqaE}{2kT}\right)C \tag{6-4}$$

$$F_3 = k_S C_I \tag{6-5}$$

where F_1, F_2, and F_3 are fluxes of oxidation, transport, and reduction, D is the ion diffusivity, *a* is the distance of each hopping step, E the electric field, kT the thermal energy, q the elementary charge, h the transfer coefficient, and k_S the reaction rate, C is the ion concentration in the electrolyte, C_O the ion concentration at the anode/electrolyte interface, C_I the ion concentration at the cathode/electrolyte interface, C^* the equilibrium ion concentration in the electrolyte. For oxidation reaction, the transfer rate is usually high, resulting in $C_O = C^*$ which is constant for particular anode and electrolyte materials. In the steady state, three fluxes are equal.

$$F_1 = F_2 = F_3 \tag{6-6}$$

According to the electrochemistry, the cation reduction flux is proportional to the charge transfer flux at the electrode/electrolyte interface. For the high bias voltage, the

Butler-Volmer equation becomes Tafel equation. Therefore we have the reduction reaction ion flux for,

$$F_3 = k_S C_I = \frac{i}{zq} = \frac{i_0}{zq}\exp\left(\frac{(1-\alpha)zq}{kT}\eta\right) \tag{6-7}$$

where α is the charge transfer coefficient ($\alpha \approx 0.5$) and η is the overpotential.

Since C_O is constant in steady state, the concentration C_I at the cathode/electrolyte interface depends on the oxide thickness between the anode (Cu layer) and cathode (CF tip), i.e. the gap distance x_O. When the gap distance is large, the cations cannot immediately move from anode to cathode, and there is sufficient time for redox reactions. The ion transport is the rate-limiting process. When the gap distance is small, the ion migration is fast enough across the short distance. The redox reaction or charge transfer is the rate-limiting process. The concentration C_I at the cathode/electrolyte interface depends on the reduction reaction rate k_S and transport rate.

Two extreme cases of cation concentration are illustrated in Fig. 6-1. In Fig. 6-1(a), the diffusivity D is high while the reduction rate k_S is low. The filament growth is controlled by the reduction at the interface. In steady state the ion concentration is uniformly distributed in the electrolyte. In Fig. 6-1(b), the reduction rate k_S is high while the diffusivity D is low. The filament growth is controlled by the ion transport in the electrolyte. All the ions at the cathode are reduced to neutral atoms and therefore the ion concentration C_I at cathode/electrolyte interface is nearly zero.

6.3 Forming Process Simulation

In the ultrathin dielectric of CBRAM, the magnitude of electric field is as high as that of breakdown field. The ions can acquire enough energy to overcome the potential barriers to migrate in the solid electrolyte. The ion migration is illustrated in Fig. 6-2. Without electric field, the ions move between potential barriers of equal height E_a and jump back and forth with equal probability. The random walk process causes the diffusion of ions under the thermal energy and concentration gradient. When an external electric field is applied to the dielectric, the potential barriers are skewed along the direction of electric field. The potential barrier shows lower height on one side whereas higher barrier height on the other side. Therefore the hopping probability of ions is higher on the lower barrier side causing the ion drift flux. When the drift flux overwhelms the diffusion flux under the extremely high electric field, the hopping mechanism becomes dominant [5], [6].

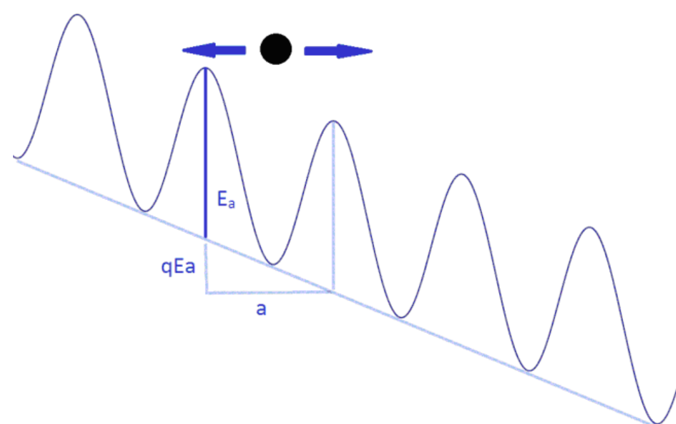

Fig. 6-2. Potential barriers seen by an ion in solid electrolyte under high electric field. The electric field distorts the random ion jump between potential wells. The unbalanced ion hopping results in ion current.

The switching process of CBRAM includes the anodic dissolution, ion transport in the solid electrolyte, nucleation and charge transfer on the electrode, and the filament growth [7]. The SET process has been modeled by the drift flux and constant ion concentration in the electrolyte [8]. With the continuum approach, the electroforming process can be simulated by solving coupled Poisson's equation, continuity equation, and moving boundary simultaneously in one dimension (1-D). The ion transport in the solid electrolyte is modeled by a high-field drift-diffusion flux (Eqs. (6-8) and (6-9)) which is deduced based on 1-D random walk theory in the high electric field [9]. The bias on activation energy results in the enhancement of ion hopping and diffusion. The Poisson's equation (Eq. (6-10)) accounts for the perturbation of the electric field due to the mobile ion distribution and fixed charges in the electrolyte. The possibly existing trapping effect is incorporated in the continuity equation (Eq. (6-11)) by the recombination term.

$$D = a^2 f \exp\left(-\frac{E_a}{kT}\right) \tag{6-8}$$

$$J = -D\cosh\left(\frac{qEa}{2kT}\right)\frac{\partial C}{\partial x} + \frac{2}{a}D\sinh\left(\frac{qEa}{2kT}\right)C \tag{6-9}$$

$$\frac{\partial^2 V}{\partial x^2} + \frac{q}{\varepsilon_r \varepsilon_0}\left(C + C_f\right) = 0 \tag{6-10}$$

$$\frac{\partial C}{\partial t} + \frac{\partial J}{\partial x} = -k_t C_{trap} C \tag{6-11}$$

where J is the flux, C is the ion concentration, D is the diffusion coefficient, *a* is the hopping distance, f is the attempt frequency, E_a is the activation energy, C_{trap} is the trap density, C_f is the fixed charge density, q the electron charge, kT the thermal energy, ε_r the dielectric constant, and k_t the trapping probability. The first term in Eq.

(6-9) is the diffusion current and the second term in Eq. (6-9) is the drift current. The Cu^+ ions are assumed to be the major charge carriers in the oxide due to the difficulty of double ionization [10]. In the forming process, the ion transport could be slower than the reduction on the electrode. Therefore, the ion transport is the rate-limiting process. The cathode acts as an ion sink and the Cu^+ concentration is nil at the moving tip of Cu nanobridge. The bias voltage is applied on the anode and the cathode is always grounded. Eqs. (6-12) to (6-15) show the boundary and initial conditions.

$$\frac{dh}{dt} = \left. \frac{|J|}{N_{Cu}^{mol}} \right|_{x=T_{ox}-h(t)} \tag{6-12}$$

$$x = 0,\ C(0,t) = C_{ss},\ V(0,t) = R_{sweep} t \tag{6-13}$$

$$x = T_{ox} - h(t),\ C(0,t) = 0,\ V(0,t) = 0 \tag{6-14}$$

$$t = 0,\ C(x,0) = 0,\ V(x,0) = V_{bias}\left(1 - \frac{x}{T_{ox}}\right) \tag{6-15}$$

where h is the length of Cu filament, R_{sweep} is the voltage sweeping rate, T_{ox} is the electrolyte thickness, h is the filament length, C_{ss} is the equilibrium Cu^+ concentration in oxide, V_{bias} is the initial bias voltage, and N_{Cu}^{mol} is the atomic density of copper. The moving boundary problem is solved by Arbitrary Lagrangian-Eulerian (ALE) method [11]. The fixed charge distribution is modeled as a uniform function or localized Gaussian density

$$C_f = C_{f0} \exp\left[-\left(\frac{x - x_0}{\sigma}\right)^2\right] \tag{6-16}$$

As the nanobridge grows, the 1-D solution applies only to a small cross-section of the bridge tip approaching the Pt electrode, whereas at the beginning of the bridge

nucleation the cross-section is the entire active cross-section of the memory cell. This funnel effect is captured in the model by a ratio of the relative cross-sections of the bridge and cell area. In our samples the cell area ranges from 1 μm^2 to 1000 μm^2, but the cross section area of the Cu bridge is few nm^2. Thus the effective high current density at the Cu bridge has to be reduced significantly when applied to the total cell cross-section. The model parameters used, respectively fitted to the experimental data for $Cu/TaO_x/Pt$ are listed in Table 6-1. Solid solubility C_{ss} in the electrolyte and the hopping distance *a* are the fitting parameters in our model. The activation energy E_a is extracted from SIMS results [12].

Table 6-1 Parameters for the simulation model of forming process in $Cu/TaO_x/Pt$ CBRAM cells.

Parameter	Description	Value and Unit
a	Hopping Distance	2.6 nm
f	Attempt Frequency	10^{13} Hz
k_t	Trapping Probability	10^{-11} cm^3/s
E_a	Activation Energy	0.63 eV
C_{ss}	Equilibrium Cu concentration	10^{19} cm-3
R_{sweep}	Voltage Sweeping Rate	1 V/s
T_{ox}	Oxide Thickness	32 nm
N_{Cu}^{mol}	Cu Atomic Density	7.3×10^{22} cm^{-3}
T	Device Temperature	298 K
ε_r	Dielectric Constant	25

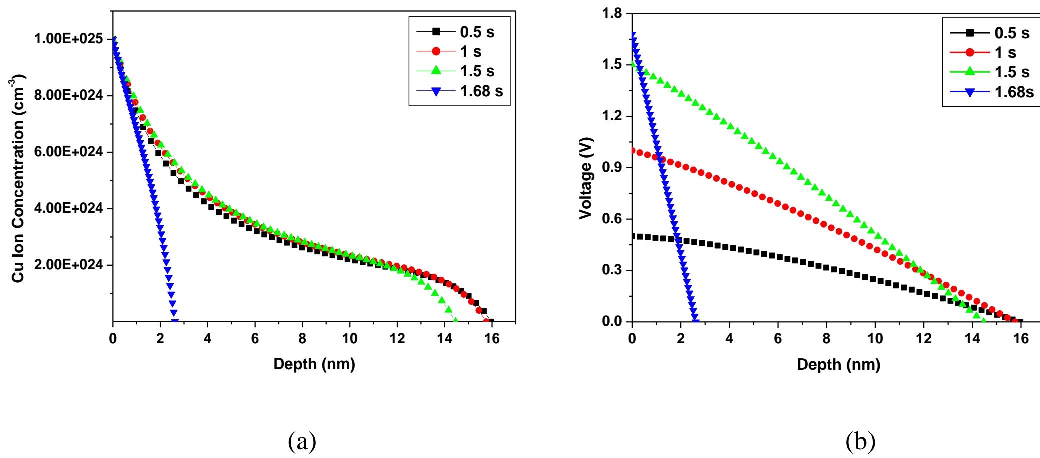

(a) (b)

Fig. 6-3. Simulation of 16 nm TaO_x devices at 298 K. The voltage ramp rate is 1 V/s. (a) Cu ion distribution in TaO_x at different times. The simulation shows most growth of the nanobridge happens within a narrow voltage range. (b) Voltage distribution in TaO_x for the Cu ion distributions given in (a). The electric field enhancement at the bridge front is within 20%.

Fig. 6-3(a) shows the simulated ion concentration distributions as the nanobridge grows. The simulated Cu^+ ions inside the solid electrolyte result in nonlinear distribution of the voltage as shown in Fig. 6-3(b). As a result, the electrical field is enhanced in the electrolyte, especially at the cathode side. Fig. 6-4(a) shows the impact of ambient temperature on the bridge evolution. The simulated result is

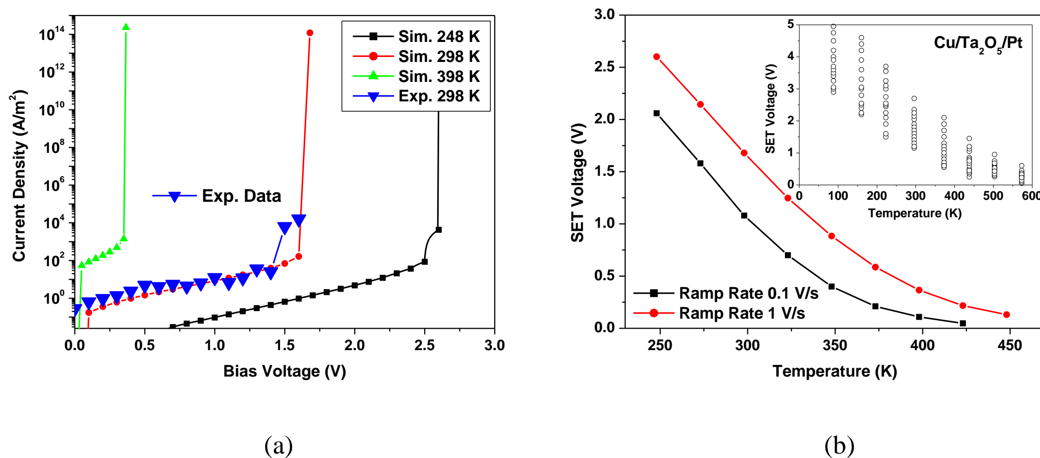

(a) (b)

Fig. 6-4. (a) Simulated and measured J–V characteristics of Cu/TaO_x/Pt CBRAM at different temperatures. (b) Simulated dependence of SET voltage on operating temperature for Cu/TaO_x/Pt cell. The inset shows the experimental SET voltages as a function of temperature [13].

compared with the experimental data obtained at room temperature. As the temperature increases, the forming voltage decreases due to the increase of diffusion coefficient and migration velocity. Table 6-2 lists the increasing growth rate h(t) at different bias voltages V_{bias}. The simulation shows most growth of bridge happens in a very narrow range of voltage. The resistance of nanobridge is neglected due to the relatively high conductivity of Cu. In HRS, the current density is almost uniform across the area of the memory cell. When the bridge front approaches the Cu electrode, the current density rises dramatically and the device shows LRS. The higher sweep rate causes the higher V_{SET}, which has been observed in experiments.

Table 6-2 Simulated growth rate of Cu nanobridge in Cu/TaO_x/Pt CBRAM cells.

V_{bias} (V)	0	0.5	1.0	1.5	1.68
dh/dt (nm/s)	1.47×10^{-2}	1.24×10^{-1}	7.04×10^{-1}	5.89	1.03×10^{13}

Fig. 6-5(a) shows the J−V characteristics of bridge formation for T_{ox}=8 nm, 16 nm, 32 nm, and 64 nm. When the oxide is thin, the transport time is short and forming voltage is low as show in Fig. 6-4(b). The dependence of the extracted V_{SET} on T_{ox} is nearly linear as confirmed by experiment [1]. The electroforming process has been eliminated for ultra-thin dielectric CBRAM devices [2].

Fig. 6-6(a) shows the same J−V characteristics as function of a uniform trapping of the drifting Cu ions. Trapping densities C_{trap} below 10^{15} cm^{-3} do not significantly affect the V_{SET}. However, at 10^{17} cm^{-3} uniform density the V_{SET} increases by more than 1 V. This result is contrasted with non-uniform trapping density of 10^{17} cm^{-3}

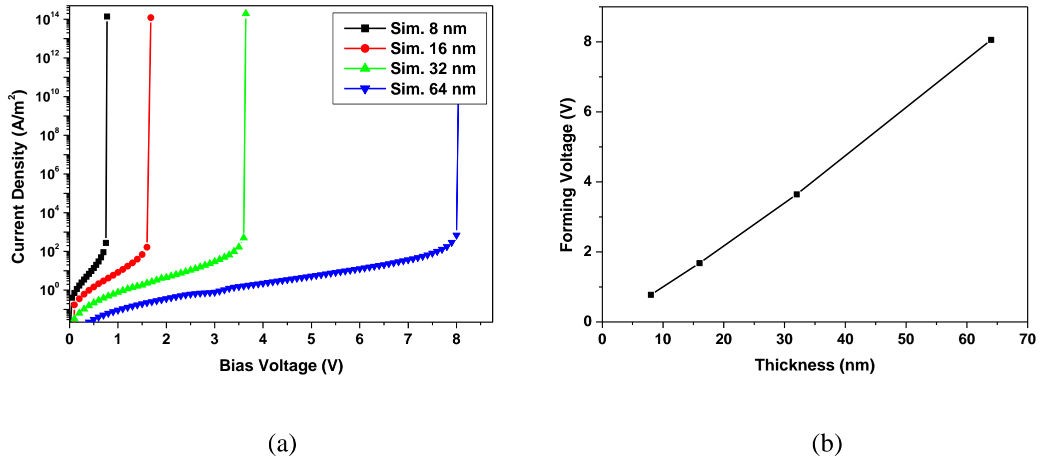

Fig. 6-5. Simulated (a) J–V characteristics and (b) electroforming voltages of Cu/TaO_x/Pt CBRAM for different oxide thickness.

peak value, Gaussian width of σ = 1 nm, and centered in the middle of the electrolyte thickness. The ion trapping may result in fixed charge in the solid electrolyte, which can be modeled as a spatial function of charge density in Poisson's equation. Fig. 6-5(b) shows the SET voltage increases when different Gaussian fixed charge densities C_f appear in the center of the solid electrolyte for three distribution widths of 0.0, 0.2 and 2.0 nm. It can be seen that wider trap distributions impact significantly V_{SET}. The ion trapping could be an important factor in the reliability and endurance of

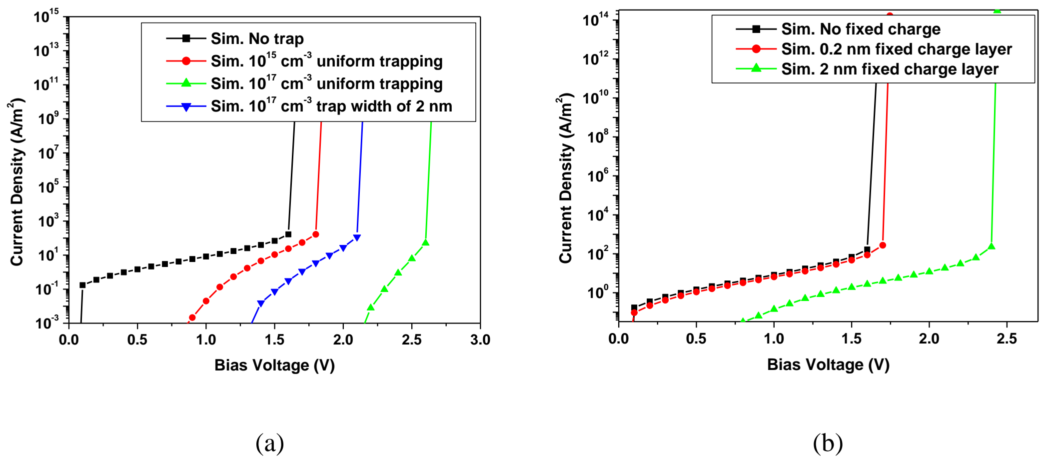

Fig. 6-6. (a) Simulated J–V characteristics of Cu/TaO_x/Pt CBRAM at different trapping densities. (b) Simulated J–V characteristics of Cu/TaO_x/Pt CBRAM at different widths of fixed charge layer.

the device and imposes a requirement on the dielectric deposition and purity.

It is of interest to note that the model parameters have been adjusted in such a way that the entire J–V characteristics shown in Figs. 6-4, 6-4, and 5-5 can be described by the Cu^{+} ionic current only, in remarkable agreement with the experimental data. No electronic contribution had to be invoked. Clearly, electronic contribution to the overall current does exist. Any electronic contribution typical of dielectrics at low voltages and any electron tunnel contribution at high voltages when the bridge is almost completed would necessitate readjustment of the model parameters resulting in lower contribution of Cu^{+} ionic current to the total measured current.

6.4 Modeling of Thermal Effect in RESET Process

The electrochemical dissolution of metallic nanofilament has been identified as the mechanism for the low power RESET process of CBRAM [4], [14]. However, high current and voltage are observed in the RESET process of $Cu/TaO_x/Pt$ devices.

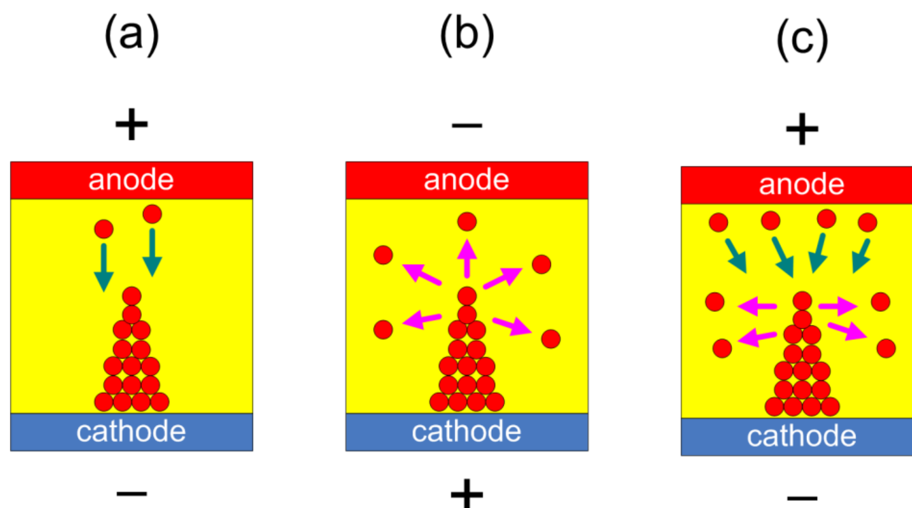

Fig. 6-7. Electrochemical dissolution in bipolar and unipolar switching. (a) SET process (b) RESET process in bipolar switching (c) RESET in unipolar switching.

Since the thermal power is dissipated in the nanoscale volume, a significant temperature rise is expected. In this section, numerical method is applied to evaluate the heating effect in the RESET process of $Cu/TaO_x/Pt$ devices. Fig. 6-7 shows the illustration of electrochemical dissolution processes in bipolar and unipolar switching. For bipolar switching, there is no ion flux from the anode since the overpotential on the anode surface impedes the oxidation reaction. The oxidation happens on the surface of Cu filament and the cations dissolve in the oxide from the CF. The net ion flux is destructive. In unipolar switching, the overpotential results in oxidation at the anode-electrolyte interface. The dissolved cations migrate to the filament and form a constructive flux. In the mean time, the destructive flux from the filament remains. Based on the hypothesis of electrochemical dissolution, it will be more difficult to rupture the filament in the unipolar mode than in the bipolar mode due to the additional constructive Cu ion flux. In our experiment, the RESET voltage distribution is symmetric for the bipolar and unipolar switching as shown in Fig. 6-8

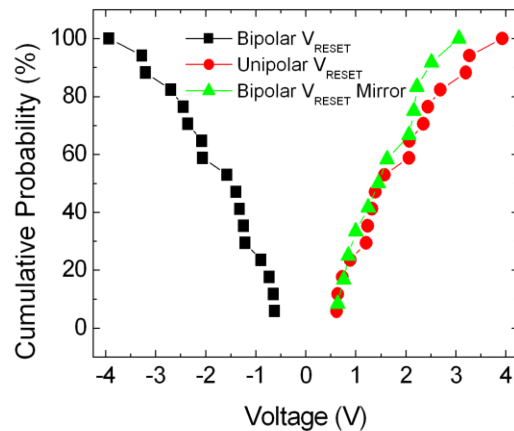

Fig. 6-8. Cumulative probability of RESET voltages of bipolar and unipolar switching for Cu filament. The V_{RESET} in bipolar switching is mirrored to its positive magnitude. It shows the cumulative probability is almost symmetrically distributed across the V_{RESET} range [15].

[15]. Therefore the thermal effect may be an important RESET mechanism for our CBRAM devices.

6.4.1 Joule Heating

When a current of mA flows through the nanobridge of hundreds of Ohms, the Joule heating is generated in the nanoscale volume and causes dramatically increasing local temperature [16]. At this temperature, Cu atoms from the CF gain enough thermal energy to overcome the potential barriers and diffuse in the dielectric. The physical processes can be modeled by the partial differential equation system. Eqs. (6-17) to (6-19) show the Poisson's equation, heat equation, and diffusion equation [17]. Eq. (6-20) considers the conductivity change with temperature. Eq. (6-21) defines the voltage sweeping rate. The material transition between Cu CF and oxide is modeled by a concentration dependent conductivity model in Eq. (6-22). A hyperbolic tangent function is used to unify the physical parameters of the metal phase and oxide phase. The initial Cu profile is described as Eq. (6-23).

$$\nabla(\sigma\nabla V)=0 \tag{6-17}$$

$$\frac{\partial T}{\partial t}=\nabla(k_{th}\nabla T)+\sigma E^2 \tag{6-18}$$

$$\frac{\partial C_D}{\partial t}=\nabla(D\nabla C_D) \tag{6-19}$$

$$\sigma=\sigma_0\left[1+\alpha(T-T_0)\right]^{-1} \tag{6-20}$$

$$\beta=\frac{dV}{dt} \tag{6-21}$$

$$\sigma=\sigma_{ox}+\frac{(\sigma_{CF}-\sigma_{ox})}{2}\left(1+\tanh\left[\frac{f(C_D-C_{crit})}{C_S}\right]\right) \tag{6-22}$$

$$C_D=\frac{C_S}{2}\left(1-\tanh\left[f(x-r_{CF})\right]\right) \tag{6-23}$$

where T is the temperature in units of Kelvin, σ is the electrical conductivity (CF or TaO_x), k_{th} is the thermal conductivity, E is the electric field, C_D is the Cu concentration, D is the diffusion coefficient, α is the temperature coefficient of resistivity (CF or TaO_x), σ_0 is the resistivity at room temperature, T_0 is the room temperature, β is the voltage sweep rate, f is the fitting factor for the transition region between Cu CF and oxide, r_{CF} is the CF radius, x is the coordinate along radial direction, C_S is the atomic density in Cu CF, and C_{crit} is the critical Cu concentration below which the Cu CF dissolves.

The three-dimensional finite element simulations are implemented and solved with COMSOL. A 3-D simulation domain is shown in Fig. 6-9. The nanofilament is modeled as a cone in the dielectric film. The electrical and thermal conductance of the metal filament and oxide electrolyte changes abruptly according to the Cu atom concentration. With the method of Cu concentration dependent parameters in Eq. (6-22), we avoid the complicated moving boundary between oxide and metal nanofilament and simplify the numerical problem. The simulated filament dissolution

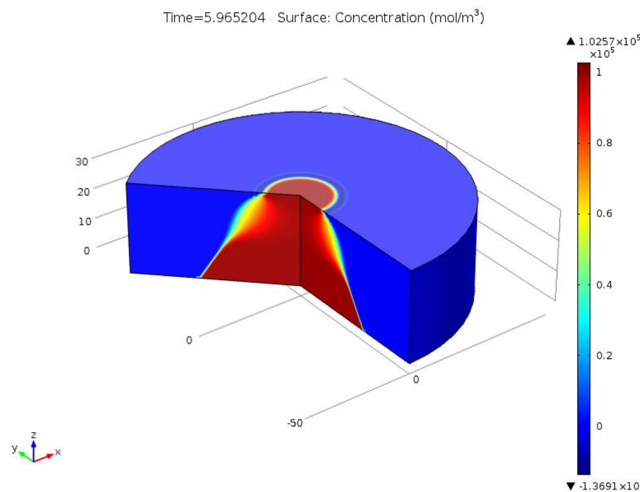

Fig. 6-9. Three-dimensional model for resistive switching simulation.

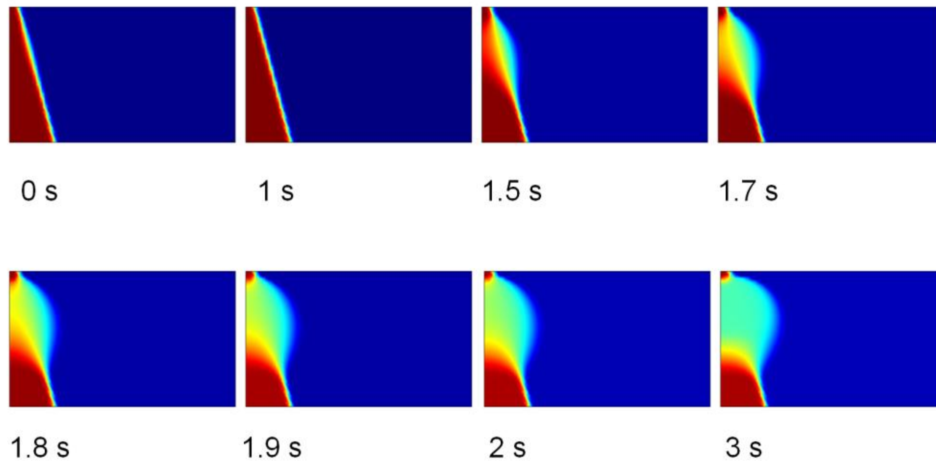

Fig. 6-10. Simulated Cu concentration at different time during CF dissolution. The color represents the ion concentration and the scale is the same as that in Fig. 6-9.

is shown in Fig. 6-10. As the time evolves, the bridge starts to weaken. However, the rupture happens from 1.8 s to 2 s, which is much shorter compared to the complete bias time period (2 s). Between 2 s and 3 s, the gap does not recess much due to the high resistance and low current state. During this time period, the residual heat is dissipated throughout the material stack. The peak temperature is below 1000 K according to the 3-D simulation.

The simulated I–t characteristic is shown in Fig. 6-11. The current characteristic includes three sections. The first section shows linear I–V characteristic which follows Ohm's law from 0 s to 1 s. In this time span the nanofilament does not dissolve much. At t = 1.2 s the nanofilament cannot sustain itself and starts weakening. From 1.2 s to 1.8 s, the nanofilament dissolves significantly and the resistance increases dramatically. At about t = 2 s, the nanofilament ruptures and the current drops to a low level close to 0 A.

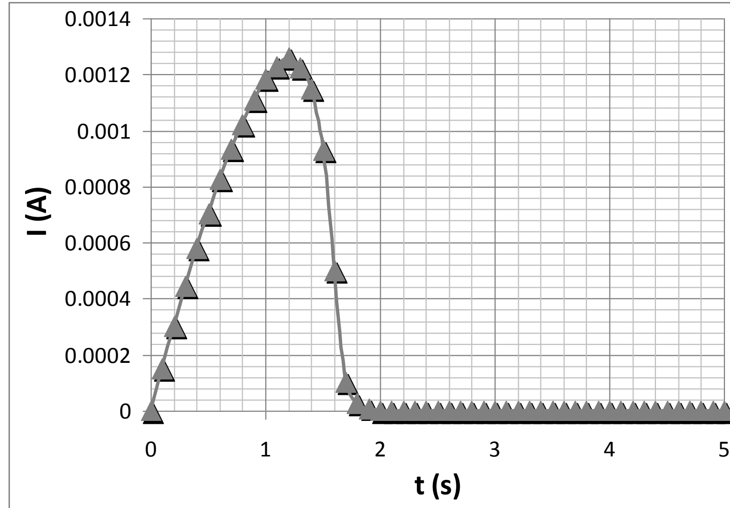

Fig. 6-11. Simulated device current at different time in RESET process.

6.4.2 Thomson Effect

Thomson effect discovered in 1851 describes the heating or cooling of a current-carrying conductor with a temperature gradient. If a current density *J* passes through a homogeneous conductor, the heat generation per unit volume *q* is:

$$q = \rho J^2 - \mu J \frac{dT}{dx} \tag{6-24}$$

where ρ is the resistivity of the material, dT/dx is the temperature gradient along the filament, J is the current density, and μ is the Thomson coefficient. The Thomson coefficient of bulk Cu is less than 10 μV/K for temperature below 1200 K [18]. The first term is the Joule heating and the second term is the Thomson heating. The Thomson heating depends on the direction of the current flowing through the filament. If the Thomson effect is significant, different RESET voltages of CBRAM could be observed for unipolar and bipolar switching since the current directions are opposite.

The numerical analysis is applied for investigating the Thomson effect. In the Fourier equation, we should consider the both the Joule heating and Thomson heating as the internal heat source. The model is described as

$$\frac{\partial T}{\partial t}=\frac{k_{th}}{\rho_m C_P}\left(\frac{\partial^2 T}{\partial x^2}+\frac{\partial^2 T}{\partial y^2}+\frac{\partial^2 T}{\partial z^2}\right)+\frac{1}{\rho_m C_P}\left(\rho J^2-\mu J\frac{dT}{dx}\right) \tag{6-25}$$

where T is the temperature, k_{th} is the thermal conductivity, C_P is the specific heat capacity, ρ_m is the mass density, ρ is the resistivity, μ is the Thomson coefficient, and J the current density. In order to simplify the model, we consider the heat diffusion in one dimension which is along the filament. A heat transfer coefficient *h* is introduced to model the heat transport from the Cu filament to the surrounding oxide [19]. Then Eq. (6-25) is rewritten as

$$\rho_m C_P\frac{\partial T}{\partial t}=k_{th}\frac{\partial^2 T}{\partial x^2}-h\frac{T-T_{ox}}{t_{ox}}+\sigma E^2-\mu\sigma E\frac{dT}{dx} \tag{6-26}$$

where T_{ox} is the oxide temperature, t_{ox} is the oxide thickness, E is the electric field, and σ the CF conductivity. The Thomson coefficient of bulk Cu is 3 to 6 μV/K between 600 and 1200 K and can be modeled as T/200 (μV/K) where T is the temperature in units of K [18]. The temperature is fixed at room temperature for each boundary of the 1-D simulation domain. The electric field E is computed by

$$E=I_0 R(x) \tag{6-27}$$

$$R(x)=\frac{1}{r_{CF}^2(x)\pi\sigma} \tag{6-28}$$

$$I_0=\frac{V}{\int_0^{t_{ox}}R(x)dx} \tag{6-29}$$

where I_0 is the total current flowing through CF, R(x)dx is the local resistance from x to x+dx, V is the bias voltage, and $r_{CF}(x)$ is the local CF radius [19].

In the metal nanowires, the resistivity and heat capacity are above bulk values [20]–[22], but the thermal conductivity and mass density are below the bulk values [23], [24]. The electrical and thermal conductivity do not strictly follow Wiedemann-Franz Law for CF because phonons may contribute significantly to the heat transfer [25]. The break of Wiedemann-Franz Law is usually observed for low dimensional metal materials [26]. Since Cu filament is embedded in the oxide matrix, the magnitudes of CF mass density ρ_m and specific heat capacity C_P are assumed between the values of TaO_x and bulk Cu. The heat transfer coefficient *h* is a fitting parameter. Its value is varied from 10^{-2} to 10^8 to investigate its effect on the Thomson effect. Simulations have shown that the magnitude of *h* only changes the temperature profile and peak temperature, but its effect on the temperature difference, or Thomson effect, is small for opposite current direction. This means it has limited impact on the Thomson effect.

In a cylindrical Cu filament, the temperature profiles will be the same for positively (unipolar) and negatively (bipolar) biased RESET voltages. The two profiles will show mirror symmetry about the center of filament. Therefore there is no difference in the RESET voltages because of the heating effect. Only asymmetric CF geometry can generate different temperature profiles along the filament due to the Thomson heating. In a conical filament, the bottom radius is $r_{CF(max)}$ and the top radius

is $\alpha \cdot r_{CF(max)}$ ($\alpha < 1$). For any position on the filament, if the distance between the filament tip and this position is *x*, the radius at this position is

$$r(x) = r_{CF(\max)}\left[(1-\alpha)\frac{x}{t_{ox}} + \alpha\right] \tag{6-30}$$

For Ta_2O_5, the mass density ρ_m is 6.85~8.2 g/cm^3, the thermal conductivity k_{th} is 0.33 W/(K·cm), and the heat capacity C_P is 0.306 J/(g·K) [27]. For bulk Cu, the mass density ρ_m is 8.96 g/cm^3, the resistivity is 1.68 μΩ·cm, the thermal conductivity k_{th} is 4.01 W/(K·cm), and the heat capacity C_P is 0.385 J(g·K). Table 6-3 shows the parameters in the simulation. As a result the direction of current flow in the conical CF can generate slightly different temperature profiles. The unipolar and bipolar RESETs are compared by reversing the bias voltage. In the model, a threshold temperature (< 1000 K) is defined for the RESET process. V_{RESET} is the voltage at which the peak of temperature profile reaches the threshold.

Table 6-3 Values of parameters in the Fourier equation.

Parameter	Numerical Value	Parameter	Numerical Value
T_{amb}	300 K	C_P	0.306 J/(g·K)
ρ_{CF0}	330 μΩ·cm	ρ_m	8.2 g/cm^3
k_{th}	0.35 W/(K·cm)	μ	T/200 μV/K
h	10^8 W/(K·cm^2)	t_{ox}	32 nm
α	0.1	T_{ox}	300 K
α_T	0.003	$r_{CF(max)}$	15 nm

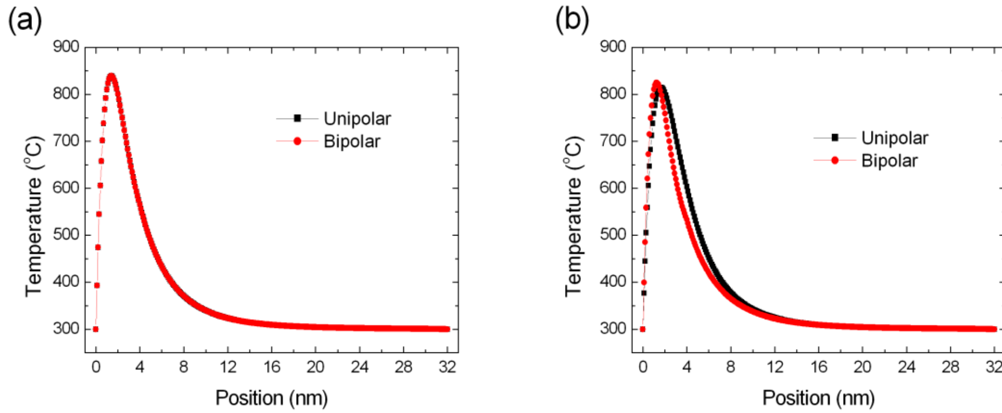

Fig. 6-12. Simulated temperature profiles of unipolar and bipolar switching in Cu/TaO_x/Pt CBRAM devices. (a) Thomson coefficient $\mu = T/200$ (μV/K). (b) Thomson coefficient $\mu = T$ (μV/K). The length of simulation domain is 32 nm.

Eqs. (6-26) to (6-30) are solved simultaneously in 1-D simulation domain for 32 nm-long Cu CF. According to parameters in Table 6-3, the simulated temperature profiles are shown in Fig. 6-12. In Fig. 6-12(a), the peak temperature difference is fairly small for bipolar and unipolar switching of Cu/TaO_x/Pt CBRAM devices. The corresponding V_{SET} difference is much smaller than that shown in Fig. 6-8 at $V_{SET} = 3$ V. In Fig. 6-12(b), the Thomson coefficient of Cu CF is increased to 200 times higher than value of bulk Cu. A slightly different temperature profile is observed in the simulation. This implies that the Thomson heating effect may not be a significant contributing factor in the RESET process of CBRAM.

6.5 Summary

A model has been proposed for simulating the resistive switching of CBRAM. The model captures main physical mechanisms in CBRAM, such as ion hopping, nucleation, filament growth, Joule heating, and diffusion. Numerically the moving boundary Stefan problem is solved by ALE method. The simulation results of

temperature dependent SET voltages are justified by the experimental results. The simulated electroforming voltage depends proportionally on the electrolyte thickness, which is also observed in experiments. Three dimensional simulations have been used to study the heating and rupture of conical shape conductive nanofilament. Due to the high local resistance and heating, the conical filament ruptures at its small tip where the filament touches the active electrode. The Thomson heating effect is also evaluated in the 1-D simulation of unipolar and bipolar switching. The TCAD simulation technology provides a better understanding of the metal-insulator-metal stack. It may also lead to a design approach of CBRAM devices, which is the same as its predecessor Si MOSFET.

Chapter 7 Summary and Future Works

This chapter summarizes the results obtained on Cu/TaO_x/Pt resistive switching devices. The switching mechanism is proposed to be based on the formation and rupture of a metallic conductive filament. Possible future areas of research are recommended for the improvement of resistive switches and nonvolatile memory based logic circuits.

7.1 Summary

The metal-oxide-semiconductor structure limits the future scaling of flash memory. To overcome this fundamental scaling obstacle, emerging device technologies have been proposed for the replacement of flash memory. These emerging memories are based on thin film stack structures compatible with CMOS back-end-of-line processes. Therefore the future scaling of nonvolatile memory is not only in 2D but also in 3D. In this research, Cu/TaO_x/Pt resistive switching devices are fabricated and characterized for understanding the physics of conductive bridge resistive memory. The works are summarized below:

(1) Conductive bridge Cu/TaO_x/Pt nonvolatile memory devices were fabricated with electron beam evaporation (PVD) and lift-off technologies. The static electrical characterization was performed extensively. Both unipolar and bipolar switching behaviors were observed on the same Cu cation-based resistive device. Two switching mechanisms appear in a single device. The formation and rupture of Cu and oxygen vacancy filaments are responsible for the SET and RESET processes of the devices

depending on the polarity of the bias voltage. The temperature dependences of the two filament resistances were measured to validate the two mechanisms. The bubble formed in the forming process is another evidence for the oxygen vacancy mechanism. When the compliance current was not applied, multilevel SET process was demonstrated at high bias voltages, indicating the formation of multiple filaments.

(2) The volatile resistive switching characteristics were observed in the $Cu/TaO_x/\delta$-Cu/Pt devices below 100 μA. The LRS did not depend on the area of device cells which implies the filamentary switching mechanism. The device switching time depended exponentially on the bias voltages. This experiment showed the volatile switching was also based on the electrochemical reactions. A flux balance model was proposed to explain the volatile behavior and validated by the experiments. The fluctuations of resistive devices are also reduced by inserting the δ-Cu layer. The volatile resistive switches can be applied as the selection devices in series with the memory elements in the nanocrossbar memory architecture.

(3) Antiparallel resistive switches (APS) and cascaded resistive switches were proposed for neural chaotic circuits and neuromorphic computation. The two circuit elements were based on the recent research of memristive property of resistive switches. The I–V and I–t characteristics were demonstrated on the novel circuit elements. The I–V characteristics of APS showed "truncated Ohm's law" behavior which is the complementary of well known CRS [1]. The cascaded resistive switches showed highly nonlinear I–t characteristics which were explained with the

Butler-Volmer equation. The integration of these circuit elements in the nanocrossbar architecture was discussed.

(4) The multilevel switching properties were demonstrated on the Cu/TaO_x/Pt devices and modeled. The quantum conduction was observed in the I–V characteristics at very low voltage sweeping rate. This was an evidence of the metallic contact between the Cu filament and the electrodes. The voltage constant is identified as the minimum SET voltage required for the resistive device based on the analysis of the electrical characterization results. Accordingly the validation range of the multilevel switching property was discussed. The transition from HRS to LRS in the metallic contact regime is explained with a radial growth model. The geometrical form factors were introduced in the radial growth model to explain the observed conical and cylindrical shape of the metallic filaments in TEM images. This model can fit very well the multilevel switching results obtained on the CBRAM devices.

(5) The electroforming/SET and RESET processes in the resistive switching were simulated based on a phenomenological model. The ion transport was the rate-limiting process in the electroforming, whereas the redox reactions were the rate-limiting process in the SET. In the electroforming model, the ion hopping equation, Poisson’s equation, and Faraday’s equation were coupled. The simulation results were verified with the experimental results. The thinner electrolyte film required less forming voltage. In the RESET model, the thermal effects were evaluated for the CBRAM devices. According to the measured high RESET current, the Joule heating dominated the RESET process in the simulation. The Thomson

heating showed much less effect than the Joule heating on the temperature profiles in the metallic nanofilaments.

7.2 Future Works

This research explores and evaluates the switching characteristics and mechanisms of nonvolatile and volatile resistive switching devices. In order to fully exploit the advantages of resistive switching devices, future investigation can be done in the following areas:

(1) Advanced resistive switching materials and processing technologies. To improve the electrical performance and reliability of resistive memory, the electrolyte material has to be refined. Although a substantial amount of materials have been demonstrated for the resistive switching, a comprehensive comparison is unavailable. The rationale for the ideal resistive switching material system has not been well developed. The material properties are closely related to the processing method (various PVD and CVD) which finally determines the device performances. Therefore further research is required to better understand the electrode-electrolyte interaction and refine the processing technologies.

(2) Advanced TCAD models for material and device design. The accurate TCAD models are required to reduce the cost of device design, shorten the technology development time, and improve the experiment efficiency. More experiments are needed to reveal the physics of resistive switching. Although a phenomenological model has been developed for the simulation of switching processes in this work, a

stochastic model is required in the future research to reproduce the fluctuations of electrical properties (such as I–V and SET/RESET time) in the resistive switches.

(3) Memristor-based chaotic neural circuits. So far most of the memristor-based chaotic circuits are limited to theoretical study. The circuit hardware has not been really built on memristors. Since the memristive characteristics of CBRAM have been demonstrated, these resistive switching devices can be applied to the chaotic circuits for realizing their functions. For example, both single memristor and antiparallel resistive switches (APS) can be applied in the hardware of Chua's canonical circuits. This research will be very useful for validating the chaotic circuit theory and possibly enable its practical applications.

(4) Nonvolatile memory (NVM) based logic circuits. The goal is to implement logic functions in NVM and integrate computing and memory units with same device and process. This kind of nonvolatile memory is considered as the universal device for future integrated circuits. The reconfigurable computing hardware is very suitable for this research, such as FPGA and PLD. The logic operation "implication" (IMP) has been identified as the bridge between memory and logic operations [2]. The IMP function consists of a few sequential switching operations on the parallel resistive or spin-transfer torque switches. It has been proved that IMP and FALSE operations can form a computationally complete logic basis [2]. Recently resistive multiplier has been demonstrated with memristive XOR gate [3]. In addition to digital gates, analog circuits are also being developed with conventional CMOS and memristors [4]. Although the system level design of the IMP-based computation is still not clear, high

speed and low power NVM devices are required to compete with the CMOS technology. In terms of the write/erase speed and power consumption, the emerging memory technologies such as CBRAM and STTRAM are more promising for NVM logic units than the conventional flash memory.

Bibliography

Chapter 1

[1] The International Technology Roadmap for Semiconductors, Semiconductor Industry Association, www.itrs.net.

[2] M. H. Kryder and C. S. Kim, “After hard drives—what comes next?” IEEE Trans. Magn., vol. 45, no. 10, pp. 3406-3413, Oct. 2009.

[3] J. E. Brewer and M. Gill, Nonvolatile memory technologies with emphasis on flash: a comprehensive guide to understanding and using NVM devices, John Wiley & Sons, Hoboken, 2008.

[4] N. Derhacobian, S. C. Hollmer, N. Gilbert, and M. N. Kozicki, “Power and energy perspectives of nonvolatile memory technologies,” Proc. IEEE, vol. 98, no. 2, pp. 283-298, Feb. 2010.

[5] H.-S. P. Wong, S. Raoux, S. B. Kim, J. Liang, J. P. Reifenberg, B. Rajendran, M. Asheghi, and K. E. Goodson, “Phase change memory,” Proc. IEEE, vol. 98, no. 12, pp. 2201-2227, Dec. 2010.

[6] H. Ishiwara, “Ferroelectric random access memories,” J. Nanosci. Nanotechnol., vol. 12, no. 10, pp. 7619-7627, Oct. 2012.

[7] W. W. Jang, J.-B. Yoon, M.-S. Kim, J.-M. Lee, S.-M. Kim, E.-J. Yoon, K. H. Cho, S.-Y. Lee, I.-H. Choi, D.-W. Kim, and D. Park, “NEMS switch with 30 nm-thick beam and 20 nm-thick air-gap for high density non-volatile memory applications,” Solid-State Electron., vol. 52, no. 10, pp. 1578-1583, Oct. 2008.

[8] D. S. Jeong, R. Thomas, R. S. Katiyar, J. F. Scott, H. Kohlstedt, A. Petraru, and C. S. Hwang, “Emerging memories: resistive switching mechanisms and current status,” Rep. Prog. Phys., vol. 75, no. 7, p. 076502, Jul. 2012.

[9] S. A. Wolf, J. Lu, M. R. Stan, E. Chen, and D. M. Treger, “The promise of nanomagnetics and spintronics for future logic and universal memory,” Proc. IEEE, vol. 98, no. 12, pp. 2155-2168, Dec. 2010.

[10] L. O. Chua, “Memristor—the missing circuit element,” IEEE Trans. Circuit Theory, vol. 18, no. 5, pp. 507-519, Sep. 1971.

[11] D. B. Strukov, G. S. Snider, D. R. Stewart, and R. S. Williams, “The missing memristor found,” Nature, vol. 453, no. 7191, pp. 80-83, May 2008.

[12] L. Chua, “Resistance switching memories are memristors,” Appl. Phys. A, vol. 102, no. 4, pp. 765-783, Apr. 2011.

[13] J. Borghetti, G. S. Snider, P. J. Kuekes, J. J. Yang, D. R. Stewart, and R. S. Williams, “‘Memristive’ switches enable ‘stateful’ logic operations via material implication,” Nature, vol. 464, no. 7290, pp. 873-876, Apr. 2010.

[14] M. Itoh and L. O. Chua, “Memristor oscillators,” Int. J. Bifur. Chaos, vol. 18, no. 11, pp. 3183-3206, Nov. 2008.

[15] K.-H. Kim, S. Gaba, D. Wheeler, J. M. Cruz-Albrecht, T. Hussain, N. Srinivasa, and W. Lu, “A functional hybrid memristor crossbar-array/CMOS system for data storage and neuromorphic applications,” Nano Lett., vol. 12, no. 12, pp. 389-395, Dec. 2012.

[16] K. Seo, I. Kim, S. Jung, M. Jo, S. Park, J. Park, J. Shin, K. P. Biju, J. Kong, K. Lee, B. Lee, and H. Hwang, “Analog memory and spike-timing-dependent plasticity characteristics of a nanoscale titanium oxide bilayer resistive switching device,” Nanotechnol., vol. 22, no. 25, p. 254023, Jun. 2011.

[17] S. Yu, B. Gao, Z. Fang, H. Yu, J. Kang, and H.-S. P. Wong, “A neuromorphic visual system using RRAM synaptic devices with sub-pJ energy and tolerance to variability: experimental characterization and large-scale modeling,” in Tech. Dig. – Int. Electron Devices Meet., 2012, pp. 239-242.

[18] T. Hasegawa, T. Ohno, K. Terabe, T. Tsuruoka, T. Nakayama, J. K. Gimzewski, and M. Aono, “Learning abilities achieved by a single solid-state atomic switch,” Adv. Mater., vol. 22, no. 16, pp. 1831-1834, Apr. 2010.

[19] Y. Kang, T. Liu, and M. K. Orlowski, “Pulse operation of a floating-electrode memristive device,” IEEE Trans. Electron Devices, vol. 60, no. 4, pp. 1476-1479, Apr. 2013.

[20] J. G. Simmons and R. R. Verderber, “New conduction and reversible memory phenomena in thin insulating films,” Proc. R. Soc. A, vol. 301, no. 1464, pp. 77-102, Oct. 1967.

[21] M. N. Kozicki, M. Yun, L. Hilt, and A. Singh, “Applications of programmable resistance changes in metal-doped chalcogenides,” Electrochem. Soc. Proc., vol. 99-13, pp. 298-309, 1999.

[22] A. Beck, J. G. Bednorz, Ch. Gerber, C. Rossel, and D. Widmer, “Reproducible switching effect in thin oxide films for memory applications,” Appl. Phys. Lett., vol. 77, no. 1, pp. 139-141, Jul. 2000.

[23] I. Valov, R. Waser, J. R. Jameson, and M. N. Kozicki, “Electrochemical metallization memories—fundamentals, applications, prospects,” Nanotechnol., vol. 22, no. 25, p. 254003, Jun. 2011.

[24] J. J. Yang, M. D. Pickett, X. Li, D. A. A. Ohlberg, D. R. Stewart, and R. S. Williams, “Memristive switching mechanism for metal/oxide/metal nanodevices,” Nature Nanotechnol., vol. 3, no. 7, pp. 429-433, Jul. 2008.

[25] R. Waser and M. Aono, “Nanoionics-based resistive switching memories,” Nature Mater., vol. 6, no. 11, pp. 833-840, Nov. 2007.

[26] M. Lanza, G. Bersuker, M. Porti, E. Miranda, M. Nafria, and X. Aymerich, “Resistive switching in hafnium dioxide layers: local phenomenon at grain boundaries,” Appl. Phys. Lett., vol. 101, no. 19, p. 193502, Nov. 2012.

[27] R. Symanczyk, R. Bruchhaus, R. Dittrich, and M. Kund, “Investigation of the reliability behavior of conductive-bridging memory cells,” IEEE Electron Device Lett., vol. 30, no. 8, pp. 876-878, Aug. 2009.

[28] M. Wang, H. Lv, Q. Liu, Y. Li, Z. Xu, S. Long, H. Xie, K. Zhang, X. Liu, H. Sun, X. Yang, and M. Liu, “Investigation of one-dimensional thickness scaling on Cu/HfO_x/Pt resistive switching device performance,” IEEE Electron Device Lett., vol. 33, no. 11, pp. 1556-1558, Nov. 2012.

[29] Q. Mao, Z. Ji, J. Xi, “Realization of forming-free ZnO-based resistive switching memory by controlling film thickness,” J. Phys. D: App. Phys., vol. 43, no. 39, p. 395104, Oct. 2010.

[30] I. Valov, I. Sapezanskaia, A. Nayak, T. Tsuruoka, T. Bredow, T. Hasegawa, G. Staikov, M. Aono, and R. Waser, “Atomically controlled electrochemical nucleation at superionic solid electrolyte surfaces,” Nature Mater., vol. 11, no. 6, pp. 530-535, Jun. 2012.

[31] S. Maikap, S. Z. Rahaman, T. Y. Wu, F. Chen, M.-J. Kao, and M.-J. Tsai, “Low current (5 pA) resistive switching memory using high-k Ta_2O_5,” in Proc. Euro. Solid-State Device Res. Conf., 2009, pp. 217-220.

[32] C. Schindler, M. Meier, R. Waser, and M. N. Kozicki, “Resistive switching in Ag-Ge-Se with extremely low write currents,” in Proc. Non-Volatile Memory Technol. Symp., 2007, pp. 82-85.

[33] C. Park, S. H. Jeon, S. C. Chae, S. Han, B. H. Park, S. Seo, and D.-W. Kim, “Role of structure defects in the unipolar resistive switching characteristics of Pt/NiO/Pt structures,” Appl. Phys. Lett., vol. 93, no. 4, p. 042102, Jul. 2008.

[34] H. Schroeder and D. S. Jeong, “Resistive switching in a Pt/TiO_2/Pt thin film stack – a candidate for a non-volatile ReRAM,” Microelectron. Eng., vol. 84, no. 9-10, pp. 1982-1985, Sep.-Oct. 2007.

[35] T. Tsuruoka, K. Terabe, T. Hasegawa, and M. Aono, “Forming and switching mechanisms of a cation-migration-based oxide resistive memory,” Nanotechnol., vol. 21, no. 42, p. 425205, Oct. 2010.

[36] P. J. Gellings, and H. J. M. Bouwmeester, The CRC Handbook of Solid State Electrochemistry, CRC Press, Boca Raton, 1997.

[37] K. Szot, W. Speier, G. Bihlmayer, and R. Waser, "Switching the electrical resistance of individual dislocations in single-crystalline $SrTiO_3$," Nature Mater., vol. 5, no. 4, pp. 312-320, Apr. 2006.

[38] X. Liu, S. Md. Sadaf, M. Son, J. Park, J. Shin, W. Lee, K. Seo, D. Lee, and H. Hwang, "Co-occurrence of threshold switching and memory switching in $Pt/NbO_x/Pt$ cells for crosspoint memory applications," IEEE Electron Device Lett., vol. 33, no. 2, pp. 236-238, Feb. 2012.

[39] S.-L. Li, D. S. Shang, J. Li, G. L. Gang, D. N. Zheng, "Resistive switching properties in oxygen-deficient $Pr_{0.7}Ca_{0.3}MnO_3$ junctions with active Al top electrodes," J. Appl. Phys., vol. 105, no. 3, p. 033710, Feb. 2009.

[40] W. Yu, X. Li, Y. Rui, X. Liu, Q. Wang, and L. Chen, "Improvement of resistive switching property in a noncrystalline and low-resistance $La_{0.7}Ca_{0.3}MO_3$ thin film by using an Ag-Al alloy electrode," J. Phys. D: Appl. Phys., vol. 41, no. 21, p. 215409, Nov. 2008.

[41] X. A. Tran, H. Y. Yu, B. Gao, J. F. Kang, X. W. Sun, Y.-C. Yeo, B. Y. Nguyen, and M. F. Li, "Ni electrode unipolar resistive RAM performance enhancement by AlO_y incorporation into HfO_x switching dielectrics," IEEE Electron Device Lett., vol. 32, no. 9, pp. 1290-1292, Sep. 2011.

[42] X. Sun, B. Sun, L. Liu, N. Xu, X. Liu, R. Han, J. Kang, G. Xiong, and T. P. Ma, "Resistive switching in CeO_x films for nonvolatile memory application," IEEE Electron Device Lett., vol. 30, no. 4, pp. 334-336, Apr. 2009.

[43] Y. Wu, B. Lee, and H.-S. P. Wong, "Al_2O_3-based RRAM using atomic layer deposition (ALD) with 1-μA RESET current," IEEE Electron Device Lett., vol. 31, no. 12, pp. 1449-1451, Dec. 2010.

[44] S. Tappertzhofen, I. Valov, and R. Waser, "Quantum conductance and switching kinetics of AgI-based microcrossbar cells," Nanotechnol., vol. 23, no. 14, p. 145703, Apr. 2012.

[45] M. Morales-Masis, S. J. van der Molen, W. T. Fu, M. B. Hesselberth, and J. M. van Ruitenbeek, "Conductance switching in Ag_2S devices fabricated by in situ sulfurization," Nanotechnol., vol. 20, no. 9, p. 095710, Mar. 2009.

[46] T. Sakamoto, H. Sunamura, H. Kawaura, T. Hasegawa, T. Nakayma, and M. Aono, "Nanometer-scale switches using copper sulfide," Appl. Phys. Lett., vol. 82, no. 18, pp. 3032-3034, May 2003.

[47] J. van den Hurk, I. Valov, and R. Waser, "Preparation and characterization of GeS_x thin-films for resistive switching memories," Thin Solid Films, vol. 527, pp. 299-302, Jan. 2013.

[48] Y. Bernard, V. T. Renard, P. Gonon, and V. Jousseaume, "Back-end-of-line compatible conductive bridging RAM based on Cu and SiO_2," Microelectron. Eng., vol. 88, no. 5, pp. 814-816, May 2011.

[49] T. Sakamoto, N. Banno, N. Iguchi, H. Kawaura, H. Sunamura, S. Fujieda, K. Terabe, T. Hasegawa, and M. Aono, “A Ta_2O_5 solid-electrolyte switch with improved reliability,” in Tech. Dig. – VLSI Symp., 2007, pp. 38-39.

[50] M. Haemori, T. Nagata, and T. Chikyow, “Impact of Cu electrode on switching behavior in a Cu/HfO_2/Pt structure and resultant Cu ion diffusion,” Appl. Phys. Express, vol. 2, no. 6, p. 061401, Jun. 2009.

[51] H. Lv and T. Tang, “The role of CuAlO interface layer for switching behavior of Al/Cu_xO/Cu memory device,” IEEE Electron Device Lett., vol. 31, no. 12, pp. 1464-1466, Dec. 2010.

[52] Y. Li, S. Long, Q. Liu, Q. Wang, M. Zhang, H. Lv, L. Shao, Y. Wang, S. Zhang, Q. Zuo, S. Liu, and M. Liu, “Nonvolatile multilevel memory effect in Cu/WO_3/Pt device structures,” Phys. Status Solidi Rapid Res. Lett., vol. 4, no. 5-6, pp. 124-126, Jun. 2010.

[53] C. Schindler, S. C. P. Thermadam, R. Waser, and M. N. Kozicki, “Bipolar and unipolar resistive switching in Cu-doped SiO_2,” IEEE Trans. Electron Devices, vol. 54, no. 10, pp. 2762-2768, Oct. 2007.

[54] D. Braeuhaus, C. Schindler, U. Boettger, and R. Waser, “Radiofrequency sputter deposition of germanium-selenide thin films for resistive switching,” Thin Solid Films, vol. 516, no. 6, pp. 1223-1226, Jan. 2008.

[55] H. Li, B. Niu, Q. Mao, J. Xi, W. Ke, and Z. Ji, “Resistive switching characteristics of ZnO based ReRAMs with different annealing temperatures,” Solid-State Electron., vol. 75, pp. 28-32, Sep. 2012.

[56] Q. Liu, S. Long, W. Wang, S. Tanachutiwat, Y. Li, Q. Wang, M. Zhang, Z. Huo, J. Chen, and M. Liu, "Low-power and highly uniform switching in ZrO_2-based ReRAM with a Cu nanocrystal insertion layer," IEEE Electron Device Lett., vol. 31, no. 11, pp. 1299-1301, Nov. 2010.

[57] T. Sakamoto, M. Tada, K. Okamoto, and H. Hada, "Electronic conduction mechanism in atom switch using polymer solid electrolyte," IEEE Trans. Electron Devices, vol. 59, no. 12, pp. 3574-3577, Dec. 2012.

Chapter 2

[1] M. N. Kozicki and W. C. West, "Programmable metallization cell structure and method of making same," US patent 5761115, Jun. 1998.

[2] M. N. Kozicki, C. Gopalan, M. Balakrishnan, M. Park, and M. Mitkova, "Non-volatile memory based on solid electrolyte," in Proc. Non-Volatile Memory Technol. Symp., 2004, pp. 10-17.

[3] C. Schindler, S. C. P. Thermadam, R. Waser, and M. N. Kozicki, "Bipolar and unipolar resistive switching in Cu-doped SiO_2," IEEE Trans. Electron Devices, vol. 54, no. 10, pp. 2762-2768, Oct. 2007.

[4] K. Terabe, T. Hasegawa, T. Nakayama, and M. Aono, "Quantized conductance atomic switch," Nature, vol. 433, no. 7021, pp. 47-50, Jan. 2005.

[5] R. Symanczyk, R. Bruchhaus, R. Dittrich, and M. Kund, "Investigation of the reliability behavior of conductive-bridging memory cells," IEEE Electron Device Lett., vol. 30, no. 8, pp. 876-878, Aug. 2009.

[6] D.-Y. Cho, I. Valov, J. van den Hurk, S. Tappertzhofen, and R. Waser, "Direct observation of charge transfer in solid electrolyte for electrochemical metallization memory," Adv. Mater., vol. 24, no. 33, pp. 4552-4556, Aug. 2012.

[7] R. Waser, "Resistive non-volatile memory devices," Microelectron Eng., vol. 86, no. 7-9, pp. 1925-1928, Jul.-Sep. 2009.

[8] Z. Fang, H. Y. Yu, W. J. Liu, Z. R. Wang, X. A. Tran, B. Gao, and J. F. Kang, "Temperature instability of resistive switching of HfO_x-based RRAM devices," IEEE Electron Device Lett., vol. 31, no. 5, May 2010.

[9] I. G. Baek, D. C. Kim, M. J. Lee, H.-J. Kim, E. K. Yim, M. S. Lee, J. E. Lee, S. E. Ahn, S. Seo, J. H. Lee, J. C. Park, Y. K. Cha, S. O. Park, H. S. Kim, I. K. Yoo, U-I. Chung, J. T. Moon, and B. I. Ryu, "Multi-layer cross-point binary oxide resistive memory (OxRRAM) for post-NAND storage application," in Tech. Dig. – Int. Electron Devices Meet., 2005, pp. 750-753.

[10] K. Szot, W. Speier, G. Bihlmayer, and R. Waser, "Switching the electrical resistance of individual dislocations in single-crystalline $SrTiO_3$," Nature Mater., vol. 5, no. 4, pp. 312-320, Apr. 2006.

[11] T. Sakamoto, N. Banno, N. Iguchi, H. Kawaura, H. Sunamura, S. Fujieda, K. Terabe, T. Hasegawa, and M. Aono, "A Ta_2O_5 solid-electrolyte switch with improved reliability," in Tech. Dig. – VLSI Symp., 2007, pp. 38-39.

[12] N. Banno, T. Sakamoto, N. Iguchi, H. Sunamura, K. Terabe, T. Hasegawa, and M. Aono, "Diffusivity of Cu ions in solid electrolyte and its effect on the

performance of nanometer-scale switch," IEEE Trans. Electron Devices, vol. 55, no. 11, pp. 3283-3287, 2008.

[13] L. Zhang, R. Huang, M. Zhu, S. Qin, Y. Kuang, D. Gao, C. Shi, and Y. Wang, "Unipolar TaO_x-based resistive change memory realized with electrode engineering," IEEE Electron Device Lett., vol. 31, no. 9, pp. 966-968, Sep. 2010.

[14] T. Potnis, Master of Engineering Report, Virginia Tech, Blacksburg, 2013.

[15] S. Yu, Y. Wu, R. Jeyasingh, D. Kuzum, and H.-S. P. Wong, "An electronic synapse device based on metal oxide resistive switching memory for neuromorphic computation," IEEE Trans. Electron Devices, vol. 58, no. 8, pp. 2729-2737, Aug. 2011.

[16] S.-J. Choi, K.-H. Kim, G.-S. Park, H.-J. Bae, W.-Y. Yang, and S. Cho, "Multibit operation of Cu/Cu-GeTe/W resistive memory device controlled by pulse voltage magnitude and width," IEEE Electron Device Lett., vol. 32, no. 3, pp. 375-377, Mar. 2011.

[17] U. Russo, D. Ielmini, C. Cagli, A. L. Lacaita, S. Spiga, C. Wiemer, M. Perego, and M. Fanciulli, "Conductive-filament switching analysis and self-accelerated thermal dissolution model for reset in NiO-based RRAM," Tech. Dig. – Int. Electron Devices Meet., 2007, pp. 775-778.

[18] W. Guan, M. Liu, S. Long, Q. Liu, and W. Wang, "On the resistive switching mechanisms of Cu/ZrO_2:Cu/Pt," Appl. Phys. Lett., vol. 93, no. 22, p. 223506, Dec. 2008.

[19] J. R. Jameson, N. Gilbert, F. Koushan, J. Saenz, J. Wang, S. Hollmer, and M. N. Kozicki, "1-D model of the programming kinetics of conductive bridge memory cells," Appl. Phys. Lett., vol. 99, p. 063506, 2011.

[20] J. J. Yang, F. Miao, M. D. Pickett, D. A. A. Ohlberg, D. R. Stewart, C. N. Lau, and R. S. Williams, "The mechanism of electroforming of metal oxide memristive switches," Nanotechnol., vol. 20, no. 21, p. 215201, May 2009.

[21] Z. Wei, Y. Kanzawa, K. Arita, Y. Katoh, K. Kawai, S. Muraoka, S. Mitani, S. Fujii, K. Katayama, M. Iijima, T. Mikawa, T. Ninomiya, R. Miyanaga, Y. Kawashima, K. Tsuji, T. Okada, R. Azuma, K. Shimakawa, H. Sugaya, T. Takagi, R. Yasuhara, K. Horiba, H. Kumigashira, M. Oshima, "Highly reliable TaO_x ReRAM and evidence of redox reaction mechanism" in Tech. Dig. – Int. Electron Devices Meet., 2008, pp. 293-296.

[22] T.-S. Jung, Y.-J. Choi, K.-D. Suh, B.-H. Suh, J.-K. Kim, Y.-H. Lim, Y.-N. Koh, J.-W. Park, K.-J. Lee, J.-H. Park, K.-T. Park, J.-R. Kim, J.-H. Lee, H.-K. Lim, "A 3.3 V 128 Mb multi-level NAND flash memory for mass storage applications," in Tech. Dig. – Int. Solid-State Circuits Conf., 1996, pp. 32-33.

[23] S. Menzel, B. Klopstra, C. Kuegeler, U. Boettger, G. Staikov, and R. Waser, "A simulation model of resistive switching in electrochemical metallization memory cells (ECM)," Mater. Res. Soc. Symp. Proc., vol. 1160, p. 101, 2009.

[24] Y. Kang, M. Verma, T. Liu, and M. K. Orlowski, "Formation and rupture of multiple conductive filaments in a $Cu/TaO_x/Pt$ device," ECS Solid State Lett., vol. 1, no. 5, pp. Q48-Q50, Sep. 2012.

[25] Q. Liu, C. Dou, Y. Wang, S. Long, W. Wang, M. Liu, M. Zhang, and J. Chen, "Formation of multiple conductive filaments in the Cu/ZrO_2:Cu/Pt device," Appl. Phys. Lett., vol. 95, no. 2, p. 023501, Jul. 2009.

[26] X. Wu, K. Li, N. Raghavan, M. Bosman, Q.-X. Wang, D. Cha, X.-X. Zhang, and K.-L. Pey, "Uncorrelated multiple conductive filament nucleation and rupture in ultra-thin high-k dielectric based resistive random access memory," Appl. Phys. Lett., vol. 99, no. 9, p. 093502, Aug. 2011.

Chapter 3

[1] M. H. Kryder and C. S. Kim, "After hard drives—what comes next?" IEEE Trans. Magn., vol. 45, no. 10, pp. 3406-3413, Oct. 2009.

[2] E. Linn, R. Rosezin, C. Kuegeler, and R. Waser, "Complementary resistive switches for passive nanocrossbar memories," Nature Mater., vol. 9, no. 5, pp. 403-406, May 2010.

[3] X. A. Tran, H. Y. Yu, Y. C. Yeo, L. Wu, W. J. Liu, Z. R. Wang, Z. Fang, K. L. Pey, X. W. Sun, A. Y. Du, B. Y. Nguyen, and M. F. Li, "A high-yield HfO_x-based unipolar resistive RAM employing Ni electrode compatible with Si-diode selector for crossbar integration," IEEE Electron Device Lett., vol. 32, no. 3, pp. 396-398, Mar. 2011.

[4] F. Nardi, D. Ielmini, C. Cagli, S. Spiga, M. Fanciulli, L. Goux, and D. J. Wouters, "Control of filament size and reduction of reset current below 10 μA in NiO resistance switching memories," Solid-State Electron., vol. 58, no. 1, pp. 42-47, Apr. 2011.

[5] M.-J. Lee, Y. Park, D.-S. Suh, E.-H. Lee, S. Seo, D.-C. Kim, R. Jung, B.-S. Kang, S.-E. Ahn, C. B. Lee, D. H. Seo, Y.-K. Cha, I.-K. Yoo, J.-S. Kim, and B. H. Park, "Two series oxide resistors applicable to high speed and high density nonvolatile memory," Adv. Mater., vol. 19, no. 22, pp. 3919-3923, Nov. 2007.

[6] S. H. Chang, S. C. Chae, S. B. Lee, C. Liu, T. W. Noh, J. S. Lee, B. Kahng, J. H. Jang, M. Y. Kim, D.-W. Kim, and C. U. Jung, "Effects of heat dissipation on unipolar resistance switching in Pt/NiO/Pt capacitors," Appl. Phys. Lett., vol. 92, no. 18, p. 183507, 2008.

[7] S. H. Chang, J. S. Lee, S. C. Chae, S. B. Lee, C. Liu, B. Kahng, D.-W. Kim, and T. W. Noh, "Occurrence of both unipolar memory and threshold resistance switching in a NiO film," Phys. Rev. Lett., vol. 102, no. 2, p. 026801, Jan. 2009.

[8] Y. C. Yang, F. Pan, and F. Zeng, "Bipolar resistance switching in high-performance Cu/ZnO:Mn/Pt nonvolatile memories: active region and influence of Joule heating," New J. Phys., vol. 12, no. 2, p. 023008, Feb. 2010.

[9] C.-J. Chen, H.-J. Yen, W.-C. Chen, and G.-S. Liou, "Resistive switching non-volatile and volatile memory behavior of aromatic polyimides with various electron-withdrawing moieties," J. Mater. Chem., vol. 22, no., 28, pp.14085-14093, 2012.

[10] T. Kurosawa, Y.-C. Lai, T. Higashihara, M. Ueda, C.-L. Liu, and W.-C. Chen, "Tuning the electrical memory characteristics from volatile to nonvolatile by

perylene imide composition in random copolyimides," Macromolecules, vol. 45, no. 11, pp. 4556-4563, Jun. 2012.

[11] T. Hasegawa, Y. Itoh, H. Tanaka, T. Hino, T. Tsuruoka, K. Terabe, H. Miyazaki, K. Tsukagoshi, T. Ogawa, S. Yamaguchi, and M. Aono, "Volatile/nonvolatile dual-functional atom transistor," Appl. Phys. Expr., vol. 4, no. 1, p. 015204, Jan. 2011.

[12] J. Steigman, W. Shockley, and F. C. Nix, "The self-diffusion of copper," Phys. Rev., vol. 56, no. 1, pp. 13-21, Jul. 1939.

[13] A. Kuper, H. Letaw, Jr., L. Slifkin, E. Sonder, and C. T. Tomizuka, "Self-diffusion in copper," Phys. Rev., vol. 96, no. 5, pp. 1224-1225, Dec. 1954.

[14] D. B. Butrymowicz, J. R. Manning, and M. E. Read, "Diffusion in copper and copper alloys, part IV. Diffusion in systems involving elements of group VIII," J. Phys. Chem. Ref. Data, vol. 5, no. 1, pp. 103-200, Mar. 1976.

[15] D. B. Butrymowicz, J. R. Manning, and M. E. Read, "Diffusion in copper and copper alloys, part I. volume and surface self-diffusion in copper," J. Phys. Chem. Ref. Data, vol. 2, no. 3, pp. 643-655, Jul. 1973.

[16] K. Terabe, T. Hasegawa, T. Nakayama, and M. Aono, "Quantized conductance atomic switch," Nature, vol. 433, no. 7021, pp. 47-50, Jan. 2005.

[17] U. Russo, D. Kamalanathan, D. Ielmini, A. L. Lacaita, and M. N. Kozicki, "Study of multilevel programming in programmable metallization cell (PMC) memory," IEEE Trans. Electron Devices, vol. 56, no. 5, pp. 1040-1047, May 2009.

[18] J. R. Jameson, N. Gilbert, F. Koushan, J. Saenz, J. Wang, S. Hollmer, and M. N. Kozicki, “One-dimensional model of the programming kinetics of conductive-bridge memory cells,” Appl. Phys. Lett., vol. 99, no. 6, p. 063506, Aug. 2011.

[19] I. Valov, I. Sapezanskaia, A. Nayak, T. Tsuruoka, T. Bredow, T. Hasegawa, G. Staikov, M. Aono, and R. Waser “Atomically controlled electrochemical nucleation at superionic solid electrolyte surfaces,” Nature Mater., vol. 11, no. 6, pp. 530-535, Jun. 2012.

[20] I. Valov and G. Staikov, “Nucleation and growth phenomena in nanosized electrochemical systems for resistive switching memories,” J. Solid State Electrochem., vol. 17, no. 2, pp. 365-371, Feb. 2013.

[21] C. Schindler, G. Staikov, and R. Waser, “Electrode kinetics of Cu-SiO_2-based resistive switching cells: overcoming the voltage-time dilemma of electrochemical metallization memories,” Appl. Phys. Lett., vol. 94, no. 7, p. 072109, Feb. 2009.

[22] Q. Liu, S. Long, W. Wang, S. Tanachutiwat, Y. Li, Q. Wang, M. Zhang, Z. Huo, J. Chen, and M. Liu, “Low-power and highly uniform switching in ZrO_2-based ReRAM with a Cu nanocrystal insertion layer,” IEEE Electron Device Lett., vol. 31, no. 11, pp. 1299-1301, Nov. 2010.

Chapter 4

[1] S. Yu, Y. Wu, R. Jeyasingh, D. Kuzum, and H.-S. P. Wong, “An electronic synapse device based on metal oxide resistive switching memory for

neuromorphic computation," IEEE Trans. Electron Devices, vol. 58, no. 8, pp. 2729-2737, Aug. 2011.

[2] T. Hasegawa, T. Ohno, K. Terabe, T. Tsuruoka, T. Nakayama, J. K. Gimzewski, and M. Aono, "Learning abilities achieved by a single solid-state atomic switch," Adv. Mater., vol. 22, no. 16, pp. 1832-1834, Apr. 2010.

[3] DARPA, Systems of Neuromophic Adaptive Plastic Scalable Electronics Program (SyNAPSE), www.darpa.mil.

[4] K.-H. Kim, S. Gaba, D. Wheeler, J. M. Cruz-Albrecht, T. Hussain, N. Srinivasa, and W. Lu, "A functional hybrid memristor crossbar-array/CMOS system for data storage and neuromorphic applications", Nano Lett., vol. 12, no. 1, pp. 389-395, Jan. 2012.

[5] D. B. Strukov, G. S. Snider, D. R. Stewart, and R. S. Williams, "The missing memristor found," Nature, vol. 453, no. 7191, pp. 80-83, May 2008.

[6] L. Chua, "Resistance switching memories are memristors," Appl. Phys. A, vol. 102, no. 4, pp. 765-783, Mar. 2011.

[7] E. Linn, R. Rosezin, C. Kuegeler, and R. Waser, "Complementary resistive switches for passive nanocrossbar memories," Nature Mater., vol. 9, no. 5, pp. 403-406, May 2010.

[8] Y. Yang, P. Sheridan, and W. Lu, "Complementary resistive switching in tantalum oxide-based resistive memory devices," Appl. Phys. Lett., vol. 100, no. 20, p. 203112, May 2012.

[9] S. Balatti, S. Larentis, D. C. Gilmer, and D. Ielmini, "Multiple memory states in resistive switching devices through controlled sized and orientation of the conductive filament," Adv. Mater., vol. 25, no. 10, pp. 1474-1478, Mar. 2013.

[10] X. Liu, S. M. Sadaf, S. Park, S. Kim, E. Cha, D. Lee, G.-Y. Jung, and H. Hwang, "Complementary resistive switching in niobium oxide-based resistive memory devices," IEEE Electron Device Lett., vol. 34, no. 2, pp. 235-237, Feb. 2013.

[11] Y. Kang, M. Verma, T. Liu, and M. K. Orlowski, "Pulse operation of a floating-electrode memristive device," IEEE Trans. Electron Devices, vol. 60, no. 4, pp. 1476-1479, Apr. 2013.

[12] F. Corinto, A. Ascoli, and M. Gilli, "Symmetric charge-flux nonlinearity with combined inherently-asymmetric memristors," in Proc. 20th European Conf. Circuit Theory and Design, 2011, pp. 632-636.

[13] F. Corinto, A. Ascoli, and M. Gilli, "Memristor models for chaotic neural circuits," in Proc. Int. Joint Conf. Neural Networks, 2012, pp. 1-8.

[14] A. Buscarino, L. Fortuna, M. Frasca, and L. V. Gambuzza, "A chaotic circuit based on Hewlett-Packard memristor," Chaos, vol. 22, no. 2, p. 023136, Jun. 2012.

[15] Y. Kang, M. Verma, T. Liu, and M. Orlowski, "Firing of a pulse and its control using a novel floating electrode bi-resistive device," Mater. Res. Soc. Symp. Proc., vol. 1430, p. 935, 2012.

[16] U. Russo, D. Kamalanathan, D. Ielmini, A. L. Lacaita, and M. N. Kozicki, "Study of multilevel programming in programmable metallization cell (PMC)

memory," IEEE Trans. Electron Devices, vol. 56, no. 5, pp. 1040-1047, May 2009.

[17] S. H. Jo, K.-H. Kim, and W. Lu, "Programmable resistance switching in nanoscale two-terminal devices," Nano Lett., vol. 9, no. 1, pp. 496-500, Jan. 2009.

[18] C. Schindler, G. Staikov, and R. Waser, "Electrode kinetics of Cu-SiO_2-based resistive switching cells: overcoming the voltage-time dilemma of electrochemical metallization memories," Appl. Phys. Lett., vol. 94, no. 7, p. 072109, Feb. 2009.

[19] G. Meszaros, I. Szenes, and B. Lengyel, "Measurements of charge transfer noise," Electrochem. Commun., vol. 6, no. 11, pp. 1185-1191, Nov. 2004.

[20] M. Terai, Y. Sakotsubo, Y. Saito, S. Kotsuji, and H. Hada, "Memory-state dependence of random telegraph noise of Ta_2O_5/TiO_2 stack ReRAM," IEEE Electron Device Lett., vol. 31, no. 11, pp. 1302-1304, Nov. 2010.

[21] I. Valov, R. Waser, J. R. Jameson, and M. N. Kozicki, "Electrochemical metallization memories-fundamentals, applications, prospects," Nanotechnol., vol. 22, no. 25, p. 254003, Jun. 2011.

[22] T. Hasegawa, A. Nayak, T. Ohno, K. Terabe, T. Tsuruoka, J. K. Gimzewski, and M. Aono, "Memristive operations demonstrated by gap-type atomic switches," Appl. Phys. A, vol. 102, no. 4, pp. 811-815, Mar. 2011.

[23] S.-J. Choi, G.-B. Kim, K. Lee, K.-H. Kim, W.-Y. Yang, S. Cho, H.-J. Bae, D.-S. Seo, S.-I. Kim, and K.-J. Lee, "Synaptic behaviors of a single metal-oxide resistive device," Appl. Phys. A, vol. 102, no. 4, pp. 1019-1025, Mar. 2011.

Chapter 5

[1] G. Palma, E. Vianello, C. Cagli, G. Molas, M. Reyboz, P. Blaise, B. De Salvo, F. Longnos, F. Dahmani, "Experimental investigation and emprirical modeling of the set and reset kinetics of Ag-GeS_2 conductive bridging memories," in Proc. 4th IEEE Int. Memory Workshop, 2012, pp. 178-181.

[2] S. Yu and H.-S. P. Wong, "Compact modeling of conducting-bridge random-access memory (CBRAM)," IEEE Trans. Electron Devices, vol. 58, no. 5, pp. 1352-1360, May 2011.

[3] C. Schindler, "Resistive switching in electrochemical metallization memory cells," Ph.D. dissertation, RWTH, Aachen, 2009.

[4] M. Kund, G. Beitel, C.-U. Pinnnow, T. Roehr, J. Schumann, R. Symanczyk, K.-D. Ufert, and G. Mueller, "Conductive bridging RAM (CBRAM): an emerging non-volatile memory technology scalable to sub 20 nm," in Tech. Dig. – Int. Electron Devices Meet., 2005, pp. 754-757.

[5] T. Liu, Y. Kang, M. Verma, M. Orlowski, "Novel highly nonlinear memristive circuit elements for neural networks," in Proc. Int. Joint. Conf. Neural Networks, 2012, pp. 1-8.

[6] S. Tappertzhofen, I. Valov, and R. Waser, "Quantum conductance and switching kinetics of AgI-based microcrossbar cells," Nanotechnol., vol. 23, no. 14, p. 145703, Apr. 2012.

[7] N. F. Mott and R. W. Gurney, Electronic Processes in Ionic Cystals, 2nd ed. Dover Publications, New York, 1964.

[8] J. H. Davies, The Physics of Low-Dimensional Semiconductors: An Introduction, Cambridge University Press, New York, 1998.

[9] U. Russo, D. Kamalanathan, D. Ielmini, A. L. Lacaita, and M. N. Kozicki, "Study of multilevel programming in programmable metallization cell (PMC) memory," IEEE Trans. Electron Devices, vol. 56, no. 5, pp. 1040-1047, May 2009.

[10] S. Menzel, U. Boettger, and R. Waser, "Simulation of multilevel switching in electrochemical metallization memory," J. Appl. Phys., vol. 111, no. 1, p. 014501, Jan. 2012.

[11] T. Tsuruoka, T. Hasegawa, K. Terabe, and M. Aono, "Conductance quantization and synaptic behavior in a Ta_2O_5-based atomic switch," Nanotechnol., vol. 23, no. 42, p. 435705, Nov. 2012.

[12] J. R. Jameson, N. Gilbert, F. Koushan, J. Saenz, J. Wang, S. Hollmer, M. Kozicki, and N. Derhacobian, "Quantized conductance in Ag/GeS_2/W conductive-bridge memory cells," IEEE Electron Device Lett., vol. 33, no. 2, pp. 257-259, Feb. 2012.

[13] J. J. T. Wagenaar, M. Morales-Masis, and J. M. van Ruitenbeek, "Observing 'quantized' conductance steps in silver sulfide: two parallel resistive switching mechanisms," J. Appl. Phys., vol. 111, no. 1, p. 014302, Jan. 2012.

[14] K. Terabe, T. Hasegawa, T. Nakayama, and M. Aono, "Quantized conductance atomic switch," Nature, vol. 433, no. 7201, pp. 47-50, Jan. 2005.

[15] A. Nayak, T. Tsuruoka, K. Terabe, T. Hasegawa, and M. Aono, "Switching kinetics of a Cu_2S-based gap-type atomic switch," Nanotechnol., vol. 22, no. 23, p. 235201, Jun. 2011.

[16] L. Goux, K. Sankaran, G. Kar, N. Jossart, K. Opsomer, R. Degraeve, G. Pourtois, G.-M. Rignanese, C. Detavernier, S. Clima, Y.-Y. Chen, A. Fantini, B. Govoreanu, D. J. Wouters, M. Jurczak, L. Altimime, and J. A. Kittl, "Field-driven ultrafast sub-ns programming in W\Al_2O_3\Ti\CuTe-based 1T1R CBRAM system," in Tech. Dig. – VLSI Symp., 2012, p. 69-70.

[17] A. Nayak, T. Ohno, T. Tsuruoka, K. Terabe, T. Hasegawa, J. K. Gimzewski, and M. Aono, "Controlling the synaptic plasticity of a Cu_2S gap-type atomic switch," Adv. Funct. Mater., vol. 22, no. 17, pp. 3606-3613, May 2012.

[18] G. Palma, E. Vianello, G. Molas, C. Cagli, F. Longnos, J. Guy, M. Reyboz, C. Carabasse, M. Bernard, F. Dahmani, D. Bretegnier, J. Liebault, and B. De Salvo, "Effect of the active layer thickness and temperature on the switching kinetics of GeS_2-based conductive bridge memories," Jpn. J. Appl. Phys., vol. 52, no. 4, p. 04CD02, Apr. 2013.

[19] C. Schindler, G. Staikov, and R. Waser, "Electrode kinetics of Cu-SiO_2-based resistive switching cells: overcoming the voltage-time dilemma of electrochemical metallization memories," Appl. Phys. Lett., vol. 94, no. 7, p. 072109, Feb. 2009.

[20] Y. Bernard, V. T. Renard, P. Gonon, and V. Jousseaume, "Back-end-of-line compatible conductive bridging RAM based on Cu and SiO_2," Microelectron. Eng., vol. 88, no. 5, pp. 814-816, May 2011.

[21] D. Ielmini, F. Nardi, and S. Balatti, "Evidence for voltage-driven set/reset processes in bipolar switching RRAM," IEEE Trans. Electron Devices, vol. 59, no. 8, pp. 2049-2056, Aug. 2012.

[22] S. Larentis, F. Nardi, S. Balatti, D. C. Gilmer, and D. Ielmini, "Resistive switching by voltage-driven ion migration in bipolar RRAM—part II: modeling," IEEE Trans. Electron Devices, vol. 59, no. 9, pp. 2468-2475, Sep. 2012.

[23] S. Choi, S. Balatti, F. Nardi, and D. Ielmini, "Size-dependent drift of resistance due to surface defect relaxation in conductive-bridge memory," IEEE Electron Device Lett., vol. 33, no. 8, pp. 1189-1191, Aug. 2012.

[24] K. M. Kim, M. H. Lee, G. H. Kim, S. J. Song, J. Y. Seok, J. H. Yoon, and C. S. Hwang, "Understanding structure-property relationship of resistive switching oxide thin films using a conical filament model," Appl. Phys. Lett., vol. 97, no. 16, p. 162912, Oct. 2010.

[25] T. Tsuruoka, K. Terabe, T. Hasegawa, and M. Aono, “Forming and switching mechanisms of a cation-migration-based oxide resistive memory,” Nanotechnol., vol. 21, no. 42, p. 425205, Oct. 2010.

[26] D. Kamalanathan, S. Baliga, S. C. P. Puthen Thermadam, and M. Kozicki, “ON state stability of programmable metallization cell,” in Proc. Non-Volatile Memory Technol. Symp., 2007, pp. 91-95.

[27] S. Yu and H.-S. P. Wong., “Modeling the switching dynamics of programmable-metallization-cell (PMC) memory and its application as synapse device for a neuromorphic computation system,” in Tech. Dig. – Int. Electron Devices Meet., 2010, pp. 520-523.

[28] G. Bersuker, D. C. Gilmer, D. Veksler, J. Yum, H. Park, S. Lian, L. Vandelli, A. Padovani, L. Larcher, K. McKenna, A. Shluger, V. Iglesias, M. Porti, M. Nafria, W. Taylor, P. D. Kirsch, and R. Jammy, “Metal oxide RRAM switching mechanism based on conductive filament microscopic properties,” in Tech. Dig. – Int. Electron Devices Meet., 2010, pp. 456-459.

[29] S. Z. Rahaman, S. Maikap, W. S. Chen, H. Y. Lee, F. T. Chen, T. C. Tien, and M. J. Tsai, “Impact of TaO_x nanolayer at the $GeSe_x$/W interface on resistive switching memory performance and investigation of Cu nanofilament,” J. Appl. Phys., vol. 111, no. 6, p. 063710, Mar. 2012.

[30] R. Waser and M. Aono, “Nanoionics-based resistive switching memories,” Nature Mater., vol. 6, no. 11, pp. 833-840, Nov. 2007.

[31] S. Kaeriyama, T. Sakamoto, H. Sunamura, M. Mizuno, H. Kawaura, T. Hasegawa, K. Terabe, T. Nakayama, and M. Aono, "A nonvolatile programmable solid-electrolyte nanometer switch," IEEE J. Solid-State Circuits, vol. 40, no. 1, pp. 168-176, Jan. 2005.

[32] M. N. Kozicki, M. Park, and M. Mitkova, "Nanoscale memory elements based on solid-state electrolytes," IEEE Trans. Nanotechnol., vol. 4, no. 3, pp. 331-338, May 2005.

[33] R. Waser, R. Dittmann, G. Staikov, and K. Szot, "Redox-based resistive switching memories – nanoionic mechanisms, prospects, and challenges," Adv. Mater., vol. 21, no. 25-26, pp. 2632-2663, Jul. 2009.

[34] M. Paunovic and M. Schlesinger, Fundamentals of Electrochemical Deposition, 2nd ed., John Wiley & Sons, Hoboken, 2006.

[35] Q. Liu, S. Long, H. Lv, W. Wang, J. Niu, Z. Huo, J. Chen, and M. Liu, "Controllable growth of nanoscale conductive filaments in solid-electrolyte-based ReRAM by using a metal nanocrystal covered bottom electrode," ACS Nano, vol. 4, no. 10, pp. 6162-6168, Oct. 2010.

[36] Y. C. Yang, F. Pan, Q. Liu, M. Liu, and F. Zeng, "Fully room-temperature-fabricated nonvolatile resistive memory for ultrafast and high-density memory application," Nano Lett., vol. 9, no. 4, pp. 1636-1643, Apr. 2009.

[37] U. Russo, D. Ielmini, C. Cagli, A. L. Lacaita, S. Spiga, C. Wiemer, M. Perego, and M. Fanciulli, "Conductive-filament switching analysis and self-accelerated

thermal dissolution model for reset in NiO-based RRAM," in Tech. Dig. – Int. Electron Devices Meet., 2007, pp. 775-778.

[38] U. Russo, D. Ielmini, C. Cagli, and A. L. Lacaita, "Filament conduction and reset mechanism in NiO-based resistive-switching memory (RRAM) devices," IEEE Trans. Electron Devices, vol. 56, no. 2, pp. 186-192, Feb. 2009.

[39] D. Ielmini, "Modeling the universal set/reset characteristics of bipolar RRAM by field- and temperature-driven filament growth," IEEE Trans. Electron Devices, vol. 58, no. 12, pp. 4309-4317, Dec. 2011.

[40] M. M. Fejer, S. Rowan, G. Cagnoli, D. R. M. Crooks, A. Gretarsson, G. M. Harry, J. Hough, S. D. Penn, P. H. Sneddon, and S. P. Vyatchanin, "Thermoelastic dissipation in inhomogenenous media: loss measurements and displacement noise in coated test masses for interferometric gravitational wave detectors," Phys. Rev. D, vol. 70, no. 8, p. 082003, Oct. 2004.

Chapter 6

[1] C. Schindler, G. Staikov, and R. Waser, "Electrode kinetics of Cu-SiO_2-based resistive switching cells: overcoming the voltage-time dilemma of electrochemical metallization memories," Appl. Phys. Lett., vol. 94, no. 7, p. 072109, Feb. 2009.

[2] M. Wang, H. Lv, Q. Liu, Y. Li, Z. Xu, S. Long, H. Xie, K. Zhang, X. Liu, H. Sun, X. Yang, and M. Liu, "Investigation of one-dimensional thickness scaling on Cu/HfO_x/Pt resistive switching device performance," IEEE Electron Device Lett., vol. 33, no. 11, pp. 1556-1558, Nov. 2012.

[3] V. V. Zhirnov, R. Meade, R. K. Cavin, and G. Sandhu, "Scaling limits of resistive memories," Nanotechnol., vol. 22, no. 25, p. 254027, Jun. 2011.

[4] R. Waser, R. Dittmann, G. Staikov, and K. Szot, "Redox-based resistive switching memories – nanoionic mechanisms, prospects, and challenges," Adv. Mater., vol. 21, no. 25-26, pp. 2632-2663, Jul. 2009.

[5] N. F. Mott and R. W. Gurney, Electronic Processes in Ionic Cystals, 2nd ed. Oxford University Press, London, 1964.

[6] J.-Y. Kwon, K.-S. Kim, Y.-C. Joo, and K.-B. Kim, "Simulation of the copper diffusion profile in SiO_2 during bias temperature stress (BTS) test," Jpn. J. Appl. Phys., vol. 41, no. 2A, pp. L99-L101, Feb. 2002.

[7] T. Tsuruoka, K, Terabe, T. Hasegawa, and M. Aono, "Forming and switching mechanisms of a cation-migraton-based oxide resistive memory," Nanotechnol., vol. 21, no. 42, p. 425205, Oct. 2010.

[8] S. Yu and H.-S. P. Wong., "Modeling the switching dynamics of programmable-metallization-cell (PMC) memory and its application as synapse device for a neuromorphic computation system," in Tech. Dig. – Int. Electron Devices Meet., 2010, pp. 520-523.

[9] J. D. McBrayer, "Diffusion of metals in silicon dioxide (interstitial, solid solubility, VLSI)," Ph. D. dissertation, Stanford University, 1984.

[10] J. D. McBrayer, R. M. Swanson, and T. W. Sigmon, "Diffusion of metals in silicon dioxide," J. Electrochem. Soc., vol. 133, no. 6, pp. 1242-1246, Jun. 1986.

[11] COMSOL Multiphysics User's Guide Version 4.0, 2010.

[12] N. Banno, T. Sakamoto, N. Iguchi, H. Sunamura, K. Terabe, T. Hasegawa, and M. Aono, "Diffusivity of Cu ions in solid electrolyte and its effect on the performance of nanometer-scale switch," IEEE Trans. Electron Devices, vol. 55, no. 11, pp. 3283-3237, Nov. 2008.

[13] T. Tsuruoka, K. Terabe, T. Hasegawa, and M. Aono, "Temperature effects on the switching kinetics of a Cu-Ta_2O_5-based atomic switch," Nanotechnol., vol. 22, no. 25, p. 254013, Jun. 2011.

[14] T. Sakamoto, K. Lister, N. Banno, T. Hasegawa, K. Terabe, and M. Aono, "Electronic transport in Ta_2O_5 resistive switch," Appl. Phys. Lett., vol. 91, no. 9, p. 092110, Aug. 2007.

[15] T. Potnis, Master of Engineering Report, Virginia Tech, Blacksburg, 2013.

[16] D. C. Kim, S. Seo, S. E. Ahn, D.-S. Suh, M. J. Lee, B.-H. Park, I. K. Yoo, I. G. Baek, H.-J. Kim, E. K. Yim, J. E. Lee, S. O. Park, H. S. Kim, U-I. Chung, J. T. Moon, and B. I. Ryu, "Electrical observations of filamentary conductions for the resistive memory switching in NiO films," Appl. Phys. Lett., vol. 88, no. 20, p. 202102, May 2006.

[17] S. Larentis, C. Cagli, F. Nardi, and D. Ielmini, "Filament diffusion model for simulating reset and retention processes in RRAM," Microelectron. Eng., vol. 88, no. 7, pp. 1119-1123, Jul. 2011.

[18] J. J. Lander, “Measurement of Thomson coefficient for metals at high temperatures and of Peltier coefficients for solid-liquid interfaces of metals,” Phys. Rev., vol. 74, no. 4, pp. 479-488, Aug. 1948.

[19] M. Bocquet, D. Deleruyelle, C. Muller, and J.-M. Portal, “Self-consistent physical modeling of set/reset operations in unipolar resistive-switching memories,” Appl. Phys. Lett., vol. 98, no. 26, p. 263507, Jun. 2011.

[20] Q. Huang, C. M. Lilley, M. Bode, and R. Divan, “Surface and size effects on the electrical properties of Cu nanowires,” J. Appl. Phys., vol. 104, no. 2, p. 023709, Jul. 2008.

[21] W. Steinhoegl, G. Schindler, G. Steinlesberger, M. Traving, and M. Engelhardt, “Comprehensive study of the resistivity of copper wires with lateral dimensions of 100 nm and smaller,” J. Appl. Phys., vol. 97, no. 2, p. 023706, Jan. 2005.

[22] Y. Zhang, J. X. Cao, Y. Xiao, and X. H. Yan, “Phonon spectrum and specific heat of silicon nanowires,” J. Appl. Phys., vol. 102, no. 10, p. 104303, Nov. 2007.

[23] N. R. Pradhan, H. Duan, J. Liang, and G. S. Iannacchione, “Specific heat and thermal conductivity measurement for anisotropic and random macroscopic composites of cobalt nanowires,” Nanotechnol., vol. 19, no. 48, p. 485712, Dec. 2008.

[24] L. Philippe, B. Cousin, Z. Wang, D. F. Zhang, and J. Michler, “Mass density of individual cobalt nanowires,” Appl. Phys. Lett., vol. 96, no. 5, p. 051903, Feb. 2010.

[25] U. Russo, D. Ielmini, C. Cagli, and A. L. Lacaita, “Filament conduction and reset mechanism in NiO-based resistive-switching memory (RRAM) devices,” IEEE Trans. Electron Devices, vol. 56, no. 2, pp. 186-192, Feb. 2009.

[26] X. Zhang, H. Xie, M. Fujii, H. Ago, K. Takahashi, T. Ikuta, H. Abe, and T. Shimizu, “Thermal and electrical conductivity of a suspended platinum nanofilm,” Appl. Phys. Lett., vol. 86, no. 17, p. 171912, Apr. 2005.

[27] M. M. Fejer, S. Rowan, G. Cagnoli, D. R. M. Crooks, A. Gretarsson, G. M. Harry, J. Hough, S. D. Penn, P. H. Sneddon, and S. P. Vyatchanin, “Thermoelastic dissipation in inhomogeneous media: loss measurements and displacement noise in coated test masses for interfereometric gravitational wave detectors,” Phys. Rev. D, vol. 70, no. 8, p. 082003, Oct. 2004.

Chapter 7

[1] E. Linn, R. Rosezin, C. Kuegeler, and R. Waser, “Complementary resistive switches for passive nanocrossbar memories,” Nature Mater., vol. 9, no. 5, pp. 403-406, May 2010.

[2] J. Borghetti, G. S. Snider, P. J. Kuekes, J. J. Yang, D. R. Stewart, and R. S. Williams, “‘Memristive’ switches enable ‘stateful’ logic operations via material implication,” Nature, vol. 464, no. 7290, pp. 873-876, Apr. 2010.

[3] S. Shin, K. Kim, and S.-M. Kang, “Memristive XOR for resistive multiplier,” Electronics Lett., vol. 40, no. 2, pp. 78-79, Jan. 2012.

[4] S. Shin, K. Kim, and S.-M. Kang, “Memristor applications for programmable analog ICs,” IEEE Trans. Nanotechnol., vol. 10, no. 2, pp. 266-274, Mar. 2011.